

# **The Structure and Function of the Water-Oxidizing Complex of Photosystem II and Related Model Complexes Investigated by Pulse EPR Spectroscopy**

Inaugural dissertation

for the attainment of the title of doctor  
in the Faculty of Mathematics and Natural Sciences  
at the Heinrich Heine University Düsseldorf

presented by

**Montserrat Perez-Navarro**

from Teruel, Spain

Düsseldorf, December 2017

From the Max Planck Institut für Chemische Energiekonversion

Published by permission of the  
Faculty of Mathematics and Natural Sciences at  
Heinrich Heine University Düsseldorf

Supervisor: Prof. Dr. Lubitz  
Co-supervisor: Prof. Dr. Schierbaum

Date of the oral examination: 16/02/2018

# **TABLE OF CONTENTS**

TABLE OF CONTENTS .....	3
ABBREVIATIONS AND SYMBOLS .....	5
DECLARATION.....	8
ZUSAMMENFASSUNG .....	9
ABSTRACT .....	11
1. INTRODUCTION .....	12
1.1. Photosynthesis: energy storage.....	15
1.2. Structure of the Photosystem II .....	19
1.2.1. Electron Transfer Reactions in PS II .....	20
1.2.2. Geometric and Electronic Structure of the Oxygen Evolving Complex .....	22
1.2.3. Mechanistic studies of Photosystem II .....	24
1.3. Manganese model systems – the manganese catalase.....	26
2. MATERIALS AND METHODS .....	28
2.1. The Spin Hamiltonian Formalism.....	28
2.1.1. Electron and nuclear Zeeman interaction .....	29
2.1.2. The Zero-Field Splitting .....	31
2.1.3. The Hyperfine Interaction.....	32
2.1.4. Nuclear Quadrupole Interaction .....	33
2.1.5. The Electron Exchange Interaction .....	34
2.2. The Spin Hamiltonian of the Mn Cluster of the OEC.....	35
2.3. The Spin Hamiltonian of the <sup>17</sup> O-Mn Cluster of the OEC.....	37
2.4. EPR spectroscopy techniques and spectral analysis .....	38
2.4.1. Continuous-Wave (cw) EPR.....	38
2.4.2. Pulse EPR techniques .....	39

3.	SUMMARY AND PUBLISHED PAPERS .....	48
3.1.	Ammonia binding to the oxygen-evolving complex of Photosystem II identifies the solvent-exchangeable oxygen bridge ( $\mu$ -oxo) of the manganese tetramer.....	49
3.2.	Characterization of the Oxygen Bridged Manganese Model Complexes Using Multifrequency $^{17}\text{O}$ -Hyperfine EPR Spectroscopies and Density Functional Theory.	67
3.3.	Recent developments in biological water oxidation .....	87
4.	CONCLUSIONS .....	95
	ACKNOWLEDGEMENTS .....	98
	REFERENCES.....	100

## ***ABBREVIATIONS AND SYMBOLS***

<i>A</i>	hyperfine coupling
ATP	adenosine-5'-triphosphate
$\mu_e$	Bohr magneton
BIPY	$\text{Mn}^{\text{III}}\text{Mn}^{\text{IV}}(\mu\text{-O})_2\text{bipy}_4]\text{ClO}_4$ complex
Chl	chlorophyll
Chl <i>a</i>	chlorophyll <i>a</i>
Chl <sub>D1</sub>	chlorophyll <i>a</i> bound to the D1 polypeptide
Chl <sub>D2</sub>	chlorophyll <i>a</i> bound to the D2 polypeptide
Chl <sub>Z</sub>	peripheral chlorophyll's associated with the PS II RC
CP43	protein of inner antenna complex
CP47	protein of inner antenna complex
cw	continuous wave
cyt <sub>b559</sub>	cytochrome b <sub>559</sub> of PS II
DFT	Density Functional Theory
DTNE	$\text{Mn}^{\text{III}}\text{Mn}^{\text{IV}}(\mu\text{-O})_2(\mu\text{-O}_2\text{CCH}_3)\text{DTNE}]\text{BPh}_4$ complex
EDNMR	ELDOR-Detected Nuclear Magnetic Resonance
ELDOR	Electron electron Double Resonance
ENDOR	Electron Nuclear Double Resonance
EPR	Electron Paramagnetic Resonance
ESE	electron spin echo
ESSEM	Electron Spin Echo Envelope Modulation

EXAFS	extended X-ray absorption fine-structure
FID	free induction decay
$g_e$	Lande factor
HYSCORE	Hyperfine Sublevel Correlation
$J$	Heisenberg exchange coupling constant
$k$	Boltzmann constant
LHI	light harvesting complex I
LHII	light harvesting complex II
ML	multiline
mw	microwave
NADPH	nicotinamide adenine dinucleotide phosphate
NMR	nuclear magnetic resonance
OEC	Oxygen Evolving Complex
P680	primary electron donor chlorophyll molecule in PS II
P <sub>D1</sub> /P <sub>D2</sub>	'special pair' chlorophyll a's bound to the D1/ D2 polypeptides
Pheo	pheophytin
Pheo a	pheophytin <i>a</i>
Pheo <sub>D1</sub>	Pheophytin A bound to the D1 polypeptide
Pheo <sub>D2</sub>	pheophytin a bound to the D2 polypeptide
PivOH	Mn <sup>II</sup> Mn <sup>III</sup> (μ-OH)-(μ-piv) <sub>2</sub> (Me <sub>3</sub> taen) <sub>2</sub> ](ClO <sub>4</sub> ) <sub>2</sub> complex
PQ	plastoquinone
PQH <sub>2</sub>	plastoquinol
PS I	photosystem I

PS II	photosystem II
$Q$	electrical quadrupole moment of a nucleus
$Q_A$	primary plasto-quinone acceptor of PS II
$Q_B$	secondary plasto-quinone acceptor of PS II
RC	reaction center
rf	radio frequency
<i>T.elongatus</i>	<i>Thermosynechococcus elongatus</i>
$T_1$	longitudinal (spin-lattice) relaxation time
$T_2$	spin-spin relaxation time
$W_f$	fastly exchanging substrate
WOC	Water Oxidizing Complex
$W_s$	slowly exchanging substrate
$Y_D$	tyrosine D or residue 160 of the D2 polypeptide of PS II
$Y_Z$	tyrosine Z or residue 161 of the D1 polypeptide of PS II
ZFS	Zero Field Splitting

## ***DECLARATION***

The experimental work in this thesis is assembled chapter three into four self-contained sub-chapters. Each of the sub-chapters represents one of my published or soon to be published journal articles. The investigations detailed in this thesis were carried out jointly with other collaborators.

Their contributions to this thesis include:

- Sample preparation: isolation of the PS II enzyme was done by A. Boussac and M. Nowaczyk (chapters 3.1 and 3.2).
- Time-resolved mass spectrometry measurements in chapter 3.1, collected by H. Nilsson.
- DFT calculations in chapters 3.1 and 3.2, completed by D. Pantazis.
- Simulations of part of the PS II experiments were done by N. Cox, T. Lohmiller and L. Rapatskiy (chapters 3.2).

All other work in this thesis is my own.

Montserrat Perez-Navarro

## **ZUSAMMENFASSUNG**

Ein wichtiger Baustein für die künftige Energieversorgung der Gesellschaft wird die katalytische Erzeugung von Wasserstoff aus Wasser sein. Um dies zu erreichen, ist es notwendig, effiziente und nachhaltige Katalysatoren für die Wasseroxidation bestehend aus reichlich vorhandenen Materialien zu entwickeln. Zyanobakterien, Algen and Pflanzen sind natürliche Systeme, die als Blaupause für eine effiziente Oxidation von Wasser dienen können. In diesen biologischen Systemen hat die Natur einen einzigartigen photochemisch aktiven Protein-Superkomplex entwickelt, das Photosystem II (PSII). Dieses Enzym nutzt Lichtenergie, um die Spaltung von zwei Wassermolekülen in O<sub>2</sub> und Protonen anzutreiben. Dieser elementare biologische Prozess bildet die Grundlage für Photosynthese und Kohlenstoff-Fixierung.

Der katalytische Zentrum für die Oxidation von Wasser im PS II ist ein  $\mu$ -oxo-verbrücktes tetra-Mangan-Kalzium-Cluster, Mn<sub>4</sub>O<sub>5</sub>Ca, das in vier aufeinanderfolgenden lichtinduzierten Ladungstrennungsreaktionen fünf Redoxzustände durchläuft, die S<sub>i</sub>-Zustände (*i* = 0-4). Die vorliegende Studie konzentriert sich auf den S<sub>2</sub>-Zustand mit einem effektiven Elektronenspin  $S_{\text{eff}} = 1/2$ , der sich aus der Austauschwechselwirkung zwischen den vier Mn-Ionen in den Oxidationszuständen Mn<sup>III</sup>Mn<sup>IV</sup>Mn<sup>IV</sup>Mn<sup>IV</sup> ergibt. Dieser Zustand ist paramagnetisch und ermöglicht dadurch, seine chemischen Eigenschaften durch paramagnetische Elektronenresonanz (EPR) und verwandte Techniken zu studieren. In meiner Doktorarbeit werde ich zeigen, wie Hochfeld-ESR-Spektroskopie in Kombination mit Substrat-Wasser-Markierung leistungsfähige Werkzeuge zur Untersuchung der Wechselwirkungen zwischen Substrat und Mn-Cluster bietet, wodurch die Bindestellen der beiden Substrate am Cluster identifiziert werden. Dies grenzt den Mechanismus der biologischen Oxidation von Wasser ein und liefert neue Informationen über einen oxo/oxy-Mechanismus unter Beteiligung einer der austauschbaren  $\mu$ -oxo-Brücken. Diese Ergebnisse haben

wichtige Konsequenzen für die Entwicklung von Übergangsmetall-Katalysatoren mit verbesserter Effizienz.

## ***ABSTRACT***

An important component for the future energy needs of society will be the catalytic production of hydrogen from water. To achieve this it is necessary to develop efficient, sustainable water oxidation catalysts from abundant materials. Cyanobacteria, algae and higher plants are natural systems that can serve as a blueprint for efficient water oxidation. Housed inside these large biological systems, nature has developed a unique photochemical supercomplex called Photosystem II (PSII). This enzyme uses light energy to drive the splitting of two water molecules into O<sub>2</sub> and protons. This primary biological process forms the basis of photosynthesis and carbon fixation.

The catalytic site for water oxidation in PS II is a  $\mu$ -oxo-bridged tetra manganese-calcium cluster, Mn<sub>4</sub>O<sub>5</sub>Ca, that undergoes four consecutive light-induced charge separation reactions, involving five redox intermediates, the S<sub>*i*</sub> states (*i* = 0-4). The present study is focused on S<sub>2</sub> with effective electron spin of  $S_{\text{eff}} = 1/2$ , due to the exchange interaction between the four Mn ions with oxidation states Mn<sup>III</sup>Mn<sup>IV</sup>Mn<sup>IV</sup>Mn<sup>IV</sup>. This state is paramagnetic and thus allows its chemical properties to be studied by electron paramagnetic resonance (EPR) and related techniques. In my thesis, I will describe how high-field EPR spectroscopy combined with substrate water labeling provides powerful tools to measure the interaction of the substrate with the Mn cluster, identifying the sites where the two substrates bind to the cluster, thus constraining the mechanism of biological water oxidation and providing new information where an oxo/oxyl mechanism takes place, involving one of the exchangeable  $\mu$ -oxo bridges. These results have important consequences for the development of 1<sup>st</sup> row transition metal catalysts of enhanced efficiency.

# 1. INTRODUCTION

The Earth, which is approximately 4.55 billion years old <sup>1</sup>, has fundamentally been altered by the emergence of photosynthetic organisms.<sup>2</sup> Their emergence led to the O<sub>2</sub> rich atmosphere, the formation of the protective ozone layer and all high life on Earth, including mankind. The first evidence of photosynthetic life on Earth is found in stromatolites and microfossils 3.5 billion years old on the Australian coastline.<sup>3-8</sup> These layered biochemical structures were formed in shallow water by trapping and cementation of sedimentary grains of microorganisms, especially cyanobacteria.<sup>9-11</sup>

Photosynthesis is the process by which light energy is captured and converted by a series of chemical reactions into stored chemical energy and powers practically all life.<sup>12</sup> Although society currently uses fossil fuels for much of its energy needs, these resources should also be considered photosynthetic in origin, the remnants of ancient photosynthetic organisms.

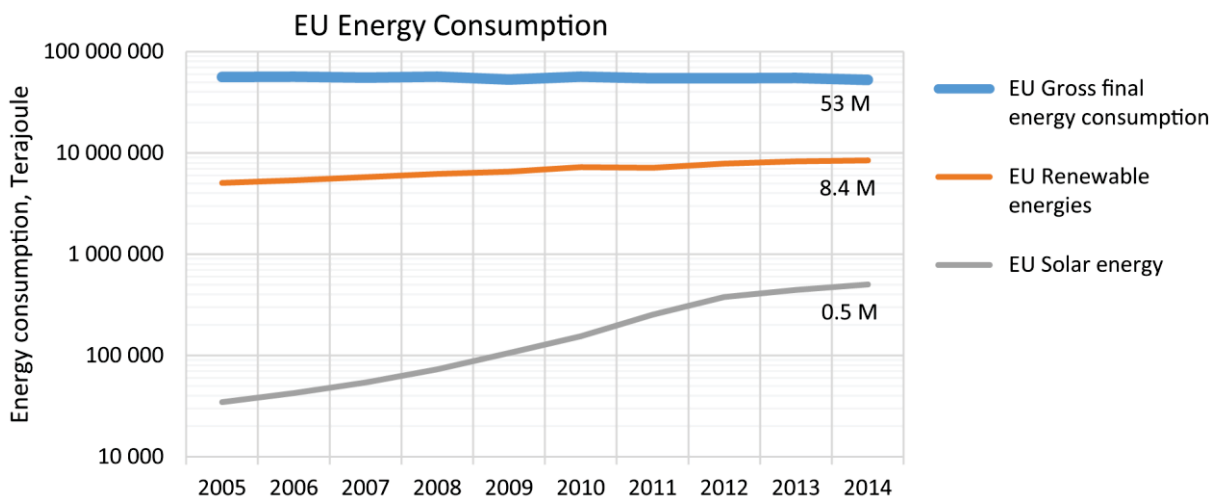


Figure 1. Increasing share of solar energy in gross final energy consumption in EU (28 countries). Source data from the Eurostat database.

As these resources are limited and their consumption implicated in anthropomorphic global warming, there is significant interest in developing alternative, renewable energy resources. According to the data from Eurostat for 28 EU countries (database [nrg\_ind\_335a]), the share of renewable energy in gross annual consumption is constantly increasing and had reached 16% in 2014, which equals  $8.42 \cdot 10^{18}$  J. Despite rapid growth in the industry of solar energy in recent years, the overall contribution to the gross annual consumption is still relatively small, only around 1% (or  $0.5 \cdot 10^{18}$  J). The evolution of the European energy consumption profile is shown in Figure 1. Currently, the solar energy industry has, for the most part, reached its limits in the efficiency of energy conversion from sunlight to thermal or electric energy, with the efficiency rates of about 92% for thermal storage, and subsequent conversion to electricity (total efficiency 17.5%) [<http://www.sciencedirect.com/science/article/pii/S1364032109001786>], and 44% for direct conversion in photovoltaics [<http://onlinelibrary.wiley.com/doi/10.1002/pip.2475/full>]. In order to expand the share of renewable energy in total energy consumption, it is necessary to invent other approaches of light energy conversion, finding effective ways of producing solar fuels, storing the solar energy in a chemical form. One of the ways to solve this problem is artificial photosynthesis.

Understanding the structure and mechanism of the energy storage processes of photosynthesis may allow us to develop efficient artificial systems that mimic its function: water splitting and hydrogen fuel generation; providing a new renewable chemical fuel for the 21<sup>st</sup> century, see Figure 2. Similarly, photosynthesis provides important design information on the efficient light collection, with applications for antenna systems, both biological and synthetic.

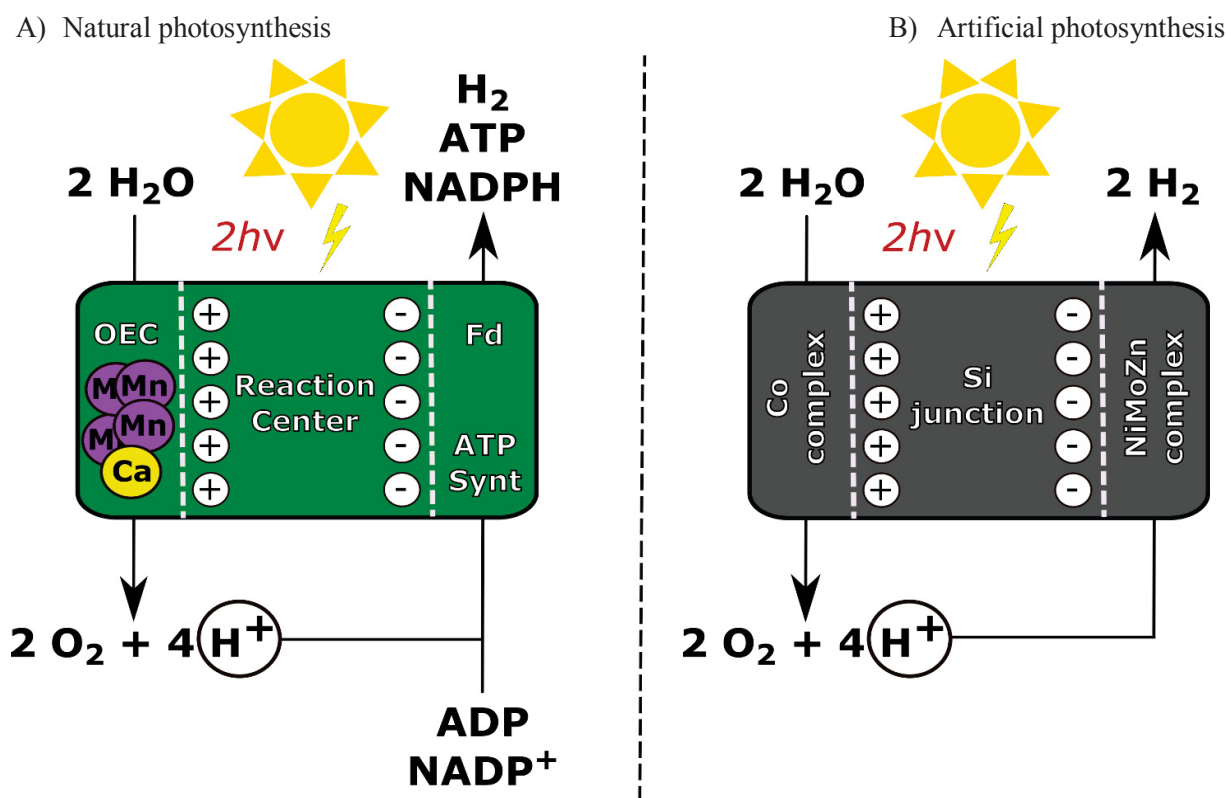


Figure 2. Figure-scheme of photosynthesis and an ‘artificial leaf’ mimic. A) The OEC and the reaction center in natural photosynthesis are part of the same structural unit (PSII) where water oxidation takes place, while Fd and ATP synthase are separate proteins that carry out the synthesis of NADPH and ATP, respectively. B) One example of an artificial leaf is the Co complex and NiMoZn complexes are separated by a Si junction, where  $H_2O$  is oxidized in the anode and  $H^+$  is reduced in the cathode.

The aim of the work presented in this thesis is to investigate the structure of the Oxygen Evolving Complex (OEC) and the mechanism of O-O bond formation to provide new important design criteria for artificial systems and devices that are able to produce  $H_2$  and  $O_2$  from water oxidation.

## ***1.1. Photosynthesis: energy storage***

Traditionally, photosynthesis has been divided into two phases: light and dark reactions.<sup>13</sup> Here, we further divide photosynthesis into four fundamental processes: during the first phase, photons are absorbed so that requires light, while the rest of the phases do not require it.<sup>14</sup> In the first phase, the light energy needed for photosynthesis is absorbed by the pigments associated with the photosynthetic apparatus, i.e. chlorophylls, carotenoids, etc.<sup>15, 16</sup> The antennas collect the light and funnel this energy to the reaction center (RC), which is a complex that contains several proteins, pigments and co-factors that carry out the primary energy conversion reactions of photosynthesis. Subsequent photon absorption by the RC creates an excited state that leads to a charge separation across the photosynthetic membrane. Ideally, no chemical reactions take place in the antenna, they just facilitate the efficient collection and migration of light energy to the RC.

In the second phase, the collected light energy is transformed into an electrochemical gradient. This takes place exclusively in the RC. RCs are found embedded in the photosynthetic membrane.<sup>17</sup> RCs are multisubunit pigment-protein complexes that contain chlorophyll and carotenoid pigments, quinones, and other redox cofactors bound to very hydrophobic polypeptides. An electron transfer cascade is initiated by the primary charge separation event between the primary electron donor (P) and the primary acceptor (A). The precise nature of P and A varies with different RCs. This first radical ion-pair state is then stabilized by secondary reactions that increase the spatial separation between the positive donor and the negative acceptor charges, minimizing charge recombination and increasing light conversion efficiency.

In the third phase, the stabilized charge separated state, chemical reactions occur on both sides of the photosynthetic membrane. On the acceptor side, mobile electron carriers are formed that allow RCs to be coupled to other redox enzymes. On the donor side, mobile electron carriers are instead consumed, which need to be replenished. In the case of oxygenic photosynthetic organisms two photochemical reaction-center complexes are coupled together linearly, Photosystem I (PS I) and

Photosystem II (PS II). The donor side of PS II oxidizes (removes electrons from) water yielding molecular oxygen as a waste product. The electrons first go on to generate reduced plastoquinone (plastoquinol) which is a mobile electron acceptor (PQ-H<sub>2</sub>). Reduced PQ-H<sub>2</sub> is used to generate a second mobile electron carrier, plastocyanin (in the cytochrome complex b<sub>6</sub>f, cytb<sub>6</sub>f, see Figure 3. The Z-scheme), which is consumed on the donor side of PS I. On the acceptor side of PS I “biological hydrogen” i.e. nicotinamide adenine dinucleotide phosphate hydrogen (NADPH) is formed.<sup>18</sup> In this way, the energy of two light photons (absorbed by PS II and PS I) is used to drive the production of NADPH using electrons from water. Concomitantly, an excess of protons is generated on the donor side of the photosynthetic membrane due to cytb<sub>6</sub>f that engages in a Q-cycle mechanism. This second electrochemical gradient is used to generate adenosine triphosphate (ATP), nature’s mobile energy currency.

A simpler cyclic transport chain exists in anoxygenic photosynthetic organisms such as *Chloroflexus aurantiacus*, which instead employs an electron transport process similar to that of purple bacteria. These organisms do not have soluble cytochromes in their apparatus. They use instead a small blue copper protein (BCP), called Auracyanin, similar to the plastocyanin in oxygenic photosynthesis, which reduces a tetraheme cytochrome that reduces the primary acceptor, P870, in the electron transport pathway. The P870 forms an excited state after light energy absorption (P870\*) and decays in several steps as an ion-pair until the cycle is complete. Auracyanins also do not include a cytochrome bc<sub>1</sub> complex in their structure, but they contain an Alternative Complex III. For a better understanding of photosynthetic organisms, Auracyanins were part of my research during my PhD, but the results are not included in this thesis.

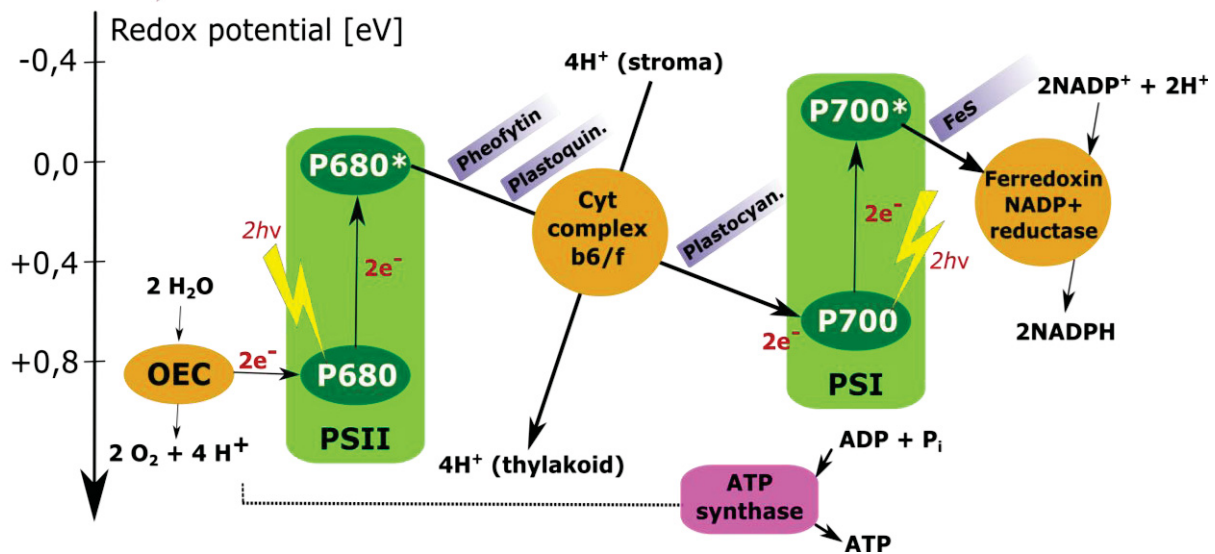


Figure 3. The Z-scheme describing the four phases of photosynthesis.

Finally, the high-energy compounds ATP and NADPH are used for long-term storage of energy. In the final fourth phase, these reduced compounds are used to fix carbon dioxide to sugars. The Calvin-Benson cycle is the carbon fixation pathway and occurs in the dark, taking place in the chloroplast stroma. The electron/energy flow throughout the four phase of photosynthesis is shown by the Z-scheme (Figure 3). Absorption of light drives the energetically uphill reactions (charge separation) of the reaction centers (PSII and PSI) allowing subsequent chemistry to occur on both the acceptor and donor sides. The redox potential of all photosynthetic components is shown on the same scale, from water (electron source) to NADPH (electron sink). Two photons of visible light are needed to generate reduced NADPH/water i.e. a potential range of +1.1 to -0.7 electron volts (eV).

The entire visible range of light (400 – 700 nm, known as the photosynthetically active radiation) and some near-infrared wavelengths (700 – 1000 nm) are highly active in driving photosynthesis.<sup>18</sup> So far, there is no organism that can utilize light of a wavelength longer than 1000 nm for photosynthesis. In the case of higher plants, algae, and cyanobacteria, most or all of their energy needs are met by sunlight and, therefore, these organisms are described as photosynthetic. While there are also other bacteria and archaea known as phototrophic, which can perform

photosynthesis as well, most of their energy needs are met by other sources, as is the case in e.g. *Chloroflexus aurantiacus*. Similarly, plants, algae, and cyanobacteria are called oxygenic because they produce oxygen during the photosynthetic process, while those that do not evolve oxygen are called anoxygenic.

## 1.2. Structure of the Photosystem II

Photosystem II is a large multisubunit protein complex embedded in the thylakoid membrane of photosynthetic organisms such as higher plants and cyanobacteria. High-resolution X-ray crystal structures of PS II purified from the cyanobacterium *Thermosynechococcus vulcanus* are now available, collected using both the standard synchrotron and new free-electron laser sources, see Figure 4.<sup>19, 20</sup> These structures represent the PS II homodimer. Each monomer contains 19 protein subunits that accommodate 77 cofactors. The core consists of two proteins, D1 (32 kDa) and D2 (34 kDa), and the inner antenna CP43 and CP47 complexes.

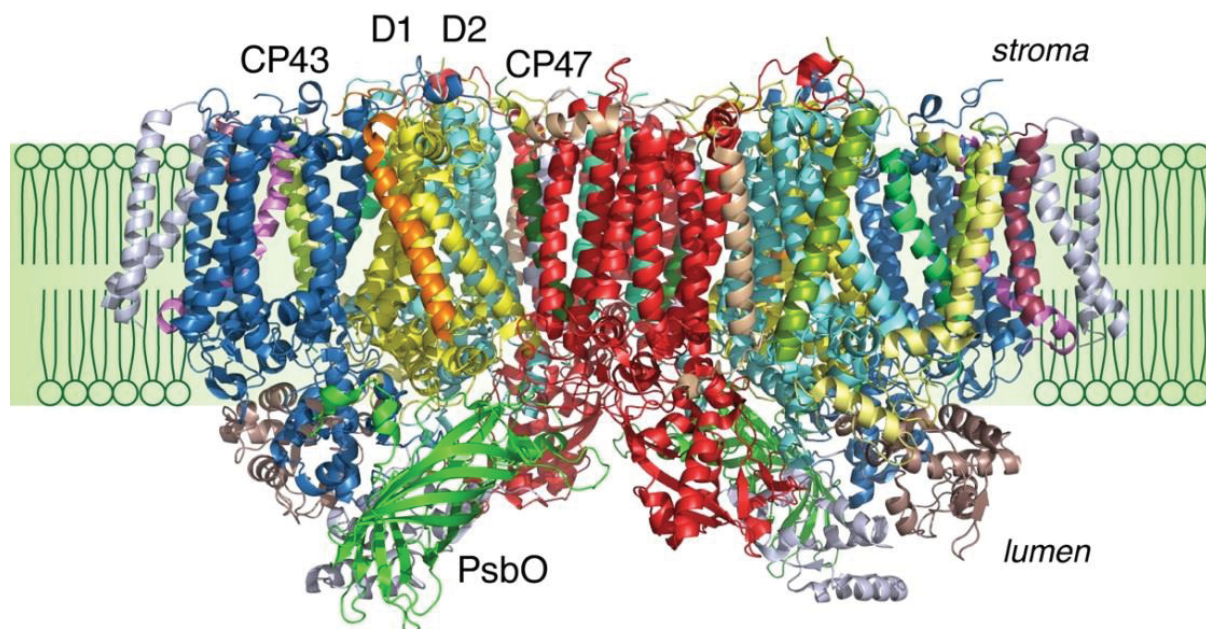


Figure 4. The structure of the PS II dimer analyzed at 1,9 Å resolution.<sup>21</sup> The dimer is presented from a perpendicular direction to the membrane normal and its structure contains 19 subunits per monomer, of which 16 are transmembrane subunits and 3 are membrane-peripheral subunits required for oxygen evolution. The reaction center core complex of PS II, where most of the electron-transfer cofactors are bound is formed by D1 and D2.

Each PS II monomer contains 35 chlorophylls (Chl *a*); 11  $\beta$ -carotenes; 2 plastoquinones (PQ) called  $Q_A$  on D2 and  $Q_B$  on D1; 2 pheophytins (Pheo *a*); 2 redox active tyrosines:  $Y_Z$  (D1-Tyr161) and  $Y_D$  (D2-Tyr160); 1  $Mn_4O_5Ca$  complex; 2 heme Fe centers; 1 non-heme Fe center between  $Q_A$  and  $Q_B$ ; and 1 hydrogen carbonate ( $HCO_3^-$ ,  $CO_3$ ) connected to the Fe; and three extrinsic soluble subunits, which are different in higher plants and cyanobacteria, and which protect and stabilize the donor side, see Figure 5.

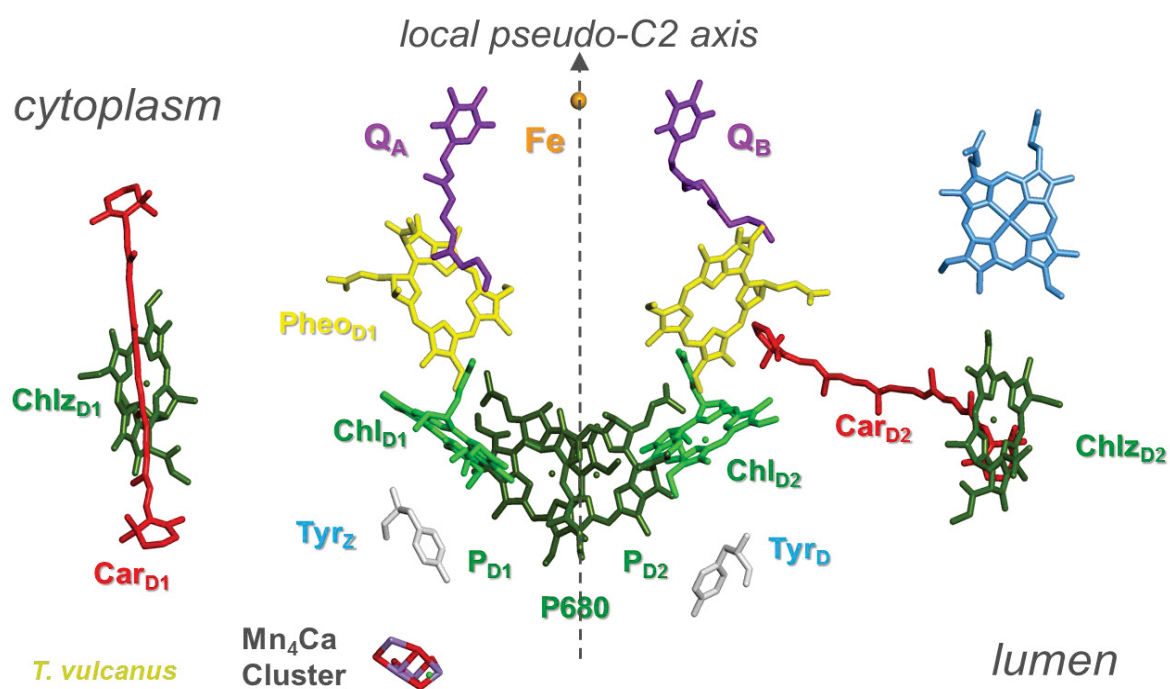
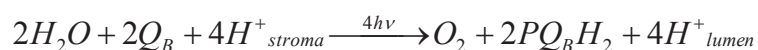


Figure 5. Arrangement of cofactors in the PS II structure of a monomer.<sup>21</sup> The vertical line located in the middle represents the local pseudo-C2 axis.

### 1.2.1. Electron Transfer Reactions in PS II

The electrons generated during the water oxidation are used to reduce plastoquinone  $Q_B$ , which is located near to the chloroplast stroma.<sup>22, 23</sup> The net reaction catalysed by PS II is that of a light-driven water-plastoquinone oxidoreductase:



Light energy collected by the antenna complexes, excites the primary electron donor P680 of PS II to the photo-excited state, P680\*. This high energy state reduces the nearby primary acceptor (Pheo<sub>D1</sub>) generating the 1<sup>st</sup> charge separated radical-pair state. The reduced Pheo<sub>D1</sub> then transfers an electron to Q<sub>A</sub>, which transfers an electron to Q<sub>B</sub>. Simultaneously, Q<sub>B</sub> takes up a cytosolic H<sup>+</sup>. These processes should be extremely fast to minimize recombination reactions. The whole process is repeated to produce plastoquinol, Q<sub>B</sub>H<sub>2</sub>, which acts as a mobile electron carrier, taking electrons from PS II and delivering them to cytochrome b<sub>6</sub>f.

On the donor side of PS II, redox-active tyrosines (Y<sub>Z</sub> and Y<sub>D</sub>) play an important role.<sup>24, 25</sup> Y<sub>Z</sub>, which lies close to P680<sup>+</sup>, donates an electron and a proton to generate a neutral radical Y<sub>Z</sub>.<sup>26, 27</sup> Subsequently, Y<sub>Z</sub> is reduced by the manganese cluster, which after four oxidation events will extract 4 electrons from two H<sub>2</sub>O molecules and releases 4 protons in the thylakoid lumen. Thus stabilization of the charge separated state occurs on both the acceptor and donor sides of PS II via linear electron flow where the electrons/electron holes formed are filled by electrons/electron holes from secondary acceptors/donors. We note that there is a second tyrosine, Y<sub>D</sub> which has a lower potential than Y<sub>Z</sub> but does not take part in the electron transfer pathway. Its role appears to be important in stabilizing the manganese cluster, bringing it to its lowest oxidation state, S<sub>0</sub>. Both tyrosines can be characterized by EPR.<sup>28</sup>

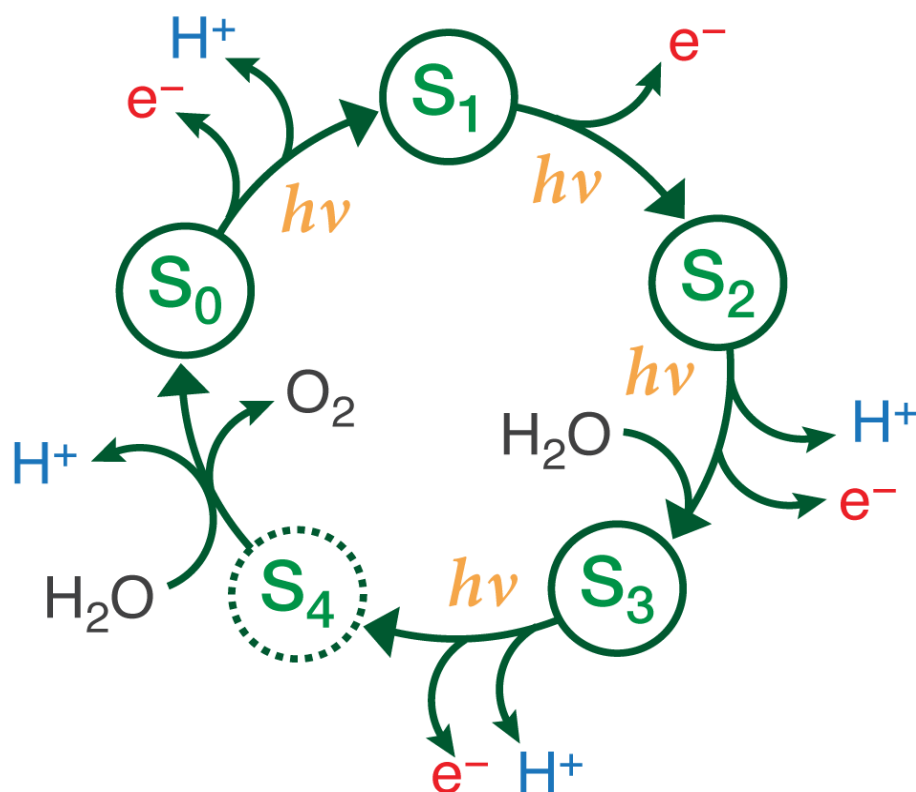


Figure 6. The catalytic Kok cycle. The five intermediate states are known as the S states: S<sub>0</sub>, S<sub>1</sub>(dark stable), S<sub>2</sub>, S<sub>3</sub>, and S<sub>4</sub> (not yet isolated.)

The manganese cluster undergoes a five step catalytic cycle known as the Kok cycle,<sup>29</sup> see Figure 6. The states are named S<sub>0-4</sub> referring to the number of oxidizing equivalents stored in the manganese cluster after each transition state. S<sub>1</sub> is known as the dark-adapted state while the S<sub>4</sub> state spontaneously decays to the S<sub>0</sub> state with the release of molecular oxygen.

### 1.2.2. Geometric and Electronic Structure of the Oxygen Evolving Complex

The crystal structure of the OEC at a resolution of 1.9 Å by Umena *et al.*<sup>19</sup> and the subsequent study of Suga *et al.*<sup>20</sup> represent the most refined and detailed picture of the water oxidation complex, see Figure 7. These structures do not only reveal the arrangement of the proteins and cofactors in PS II at the atomic level, they also resolve the position and connections of each of the ions that make up the Oxygen Evolving Complex (OEC). The OEC consists of an inorganic tetra-manganese penta-

oxygen calcium ( $Mn_4O_5Ca$ ) cluster and a redox-active tyrosine residue ( $Y_Z$  (D1-Tyr161)) that couples the manganese cluster to the P680.

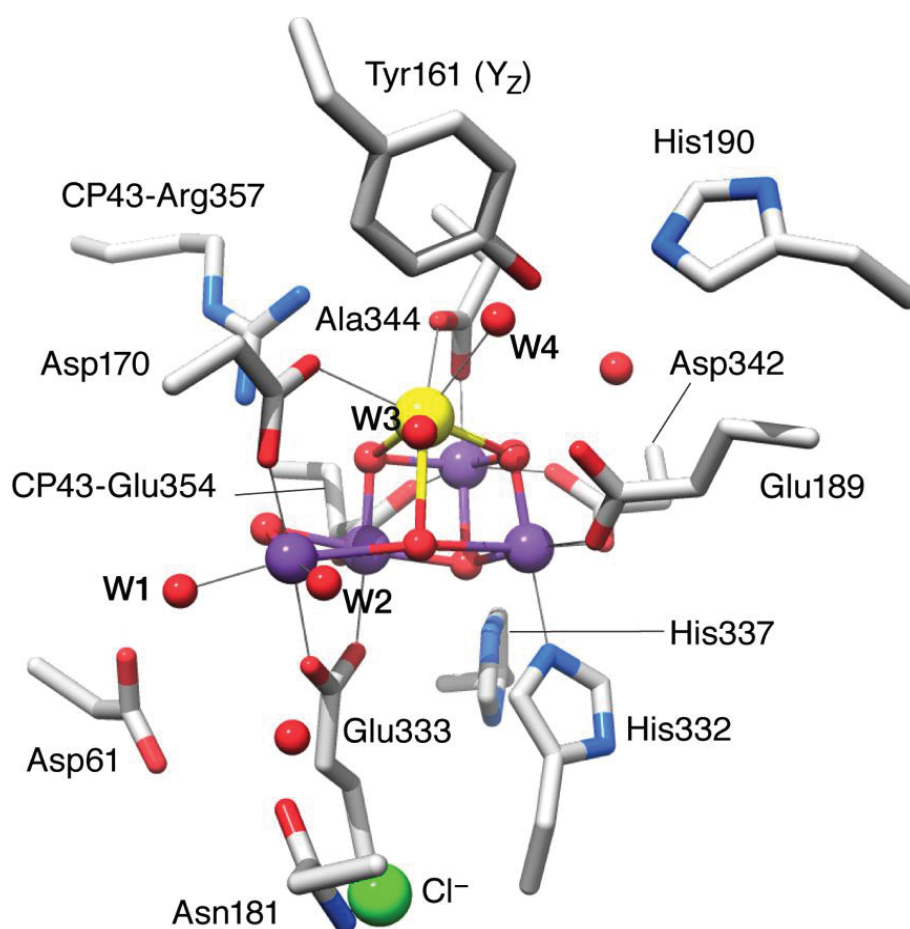


*Figure 7. The  $Mn_4O_5Ca$  cluster and its protein surrounding.*

The  $Mn_4O_5Ca$  cluster has a structure similar to a “distorted chair” (see Figure 8): three manganese ions and the calcium form the vertices of the base of the chair in a  $\mu$ -oxo-bridged cuboidal unit ( $Mn_3O_4Ca$ ). This is then linked to the outer manganese ion ( $Mn_{A4}$ ) through a  $\mu$ -oxo-bridge (O4) located in one of the corners ( $Mn_{B3}$ ) and the O5, which can also be described as one of the oxygen bridges of the cuboidal unit. In addition, the X-ray structure identified four carboxylate ligands that hold the manganese cluster in place and one directly coordinating nitrogen D1-His332. This nitrogen is well characterized by EPR techniques and it is a spin-probe of the Mn to which it is bound, MnD1. The four carboxylates, located in the first coordination sphere and directly binding to the four manganese ions of the cluster are provided by Asp342, Asp170, Glu333, and CP47-Glu354.

Finally, theoretical calculations have suggested that the structure of the OEC may be dynamic, namely that the O5 oxygen bridge allows certain flexibility. The cofactor is thus often described in terms of two discrete structural forms i) a “closed” structure where O5 forms an oxygen-bridge between Mn3 and Mn4; and ii) an “open” form where O5 remains in a hydroxo form and the Mn4 remains as a vertex of the cubane structure,<sup>30</sup> with facile interconversion between the two forms.

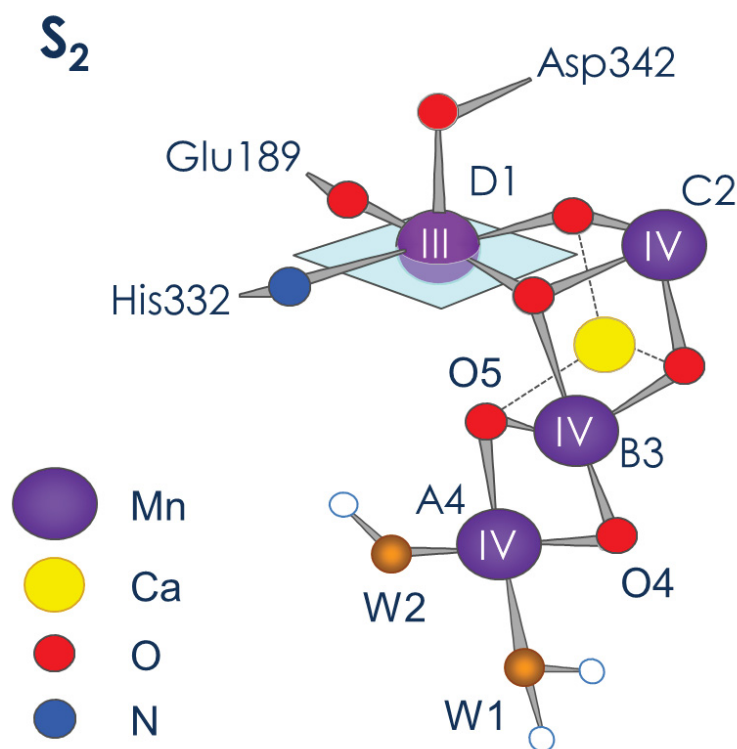


Figure 8. The  $Mn_4O_5Ca$  cluster poised at the  $S_2$  state.

### 1.2.3. Mechanistic studies of Photosystem II

The  $Mn_4O_5Ca$  cluster of PS II performs electron transfer and multistep redox reactions all of which can be studied by EPR spectroscopy.<sup>31</sup> EPR provides information about the structure and functional role of the manganese cluster by the characterization of the metal site and oxidation state of the metal cluster.<sup>32</sup> The  $S_2$  state is the most studied intermediate of the cycle. In this state the four Mn ions couple together to form a ground electronic state with one unpaired electron,  $S_{\text{eff}} = 1/2$ , giving rise to the well-known “multiline” EPR signal as a result of their coupling to the  $I=1/2$  nuclei of Mn. Using double resonance methods the interaction of the unpaired electron spin with other

magnetic nuclei present in the first and second coordination sphere can be measured, such as  $^{55}\text{Mn}$ ,  $^{17}\text{O}$ ,  $^{14}\text{N}/^{15}\text{N}$ , or  $^1\text{H}/^2\text{H}$ . These advanced EPR techniques include Electron Spin Echo Envelope Modulation (ESEEM), Electron Nuclear Double Resonance (ENDOR), ELDOR-Detected Nuclear Magnetic Resonance (EDNMR), etc., described in Chapter 2. These methods allow the fine details of the electronic structure of the cofactor to be obtained and have been crucial in resolving how substrate water interacts with the cofactor.

### ***1.3. Manganese model systems – the manganese catalase***

The complexity of the manganese cluster of PS II lead us to the necessity of studying simpler model systems that provide information that help us to understand the OEC. An important model system for the OEC of PSII is the manganese catalase. This enzyme catalyzes a similar reaction in nature, the two electron conversion (dismutation) of hydrogen peroxide to O<sub>2</sub> and water.<sup>33</sup> It comprises only two Mn ions (instead of four) and its magnetic properties, as studied by EPR, are easier to understand. The catalytic cycle of the manganese catalase (MnCat) comprises two net oxidation states: the reduced form Mn<sup>II</sup>Mn<sup>II</sup> and the oxidized form Mn<sup>III</sup>Mn<sup>III</sup> where the two oxygen bridges are assigned as a  $\mu$ -oxo/ $\mu$ -hydroxo, (see Figure 9). Mixed valence complexes such as Mn<sup>II</sup>Mn<sup>III</sup> and Mn<sup>III</sup>Mn<sup>IV</sup> can be generated from MnCat and used as models for spectroscopic studies of other Mn metallocofactors. These complexes typically exhibit antiferromagnetic coupling, which leads to the ground state configuration of total electron spin  $S_T = 1/2$ . The super oxidized state of MnCat, Mn<sup>III</sup>Mn<sup>IV</sup>, can be chemically generated. This state is EPR active ( $S_T = 1/2$ ), displaying a multiline EPR spectrum centered at  $g = 2$ , similar to the signal observed for the OEC in the S<sub>2</sub> state.<sup>34-38</sup> The electronic g-tensor, the exchange-coupling constants, the Mn-N hyperfine coupling and the nuclear quadrupole-splitting have been well described. The calculated Mn-Mn distances and the <sup>55</sup>Mn hyperfine coupling suggest the di-manganese cluster contains  $\mu$ -oxo bridges in the superoxidized state.

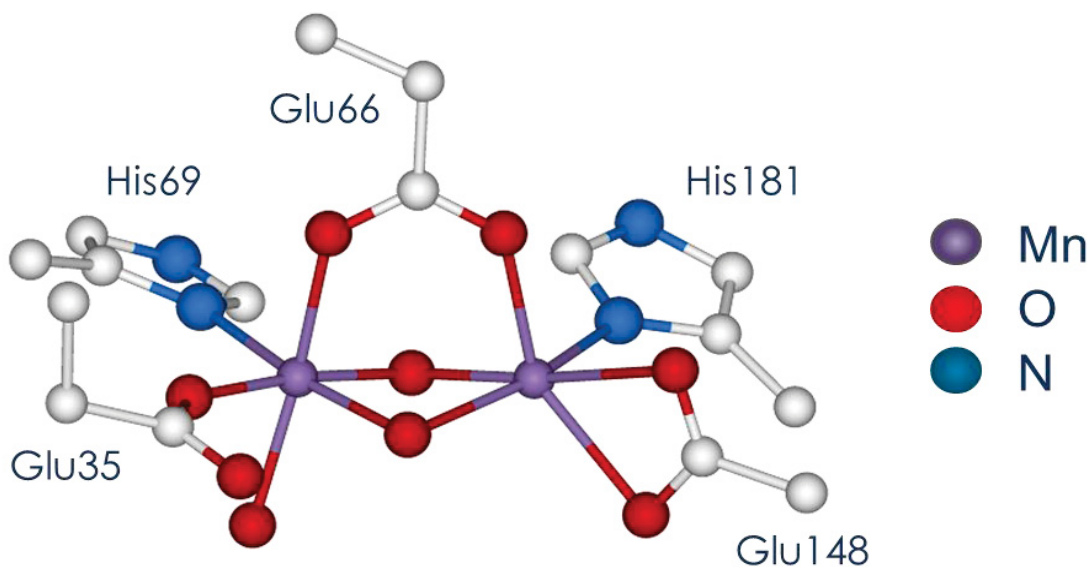


Figure 9. The manganese catalase cluster ( $Mn^{III}Mn^{IV}$ ).

The MnCat enzyme has been isolated from two organisms, *Lactobacillus plantarum* and *Thermus thermophilus*, being the last species used in the work presented in Chapter 3. The structure presents two manganese ions bridged by the  $\mu$ -carboxylate group of a glutamate and two oxygen bridges (one of which is derived from the substrate  $H_2O_2$ ). Each manganese ion has one terminal histidine and one glutamate ligand.<sup>38</sup>

Multifrequency pulsed EPR characterization, principally by the electron-electron double resonance detected NMR (EDNMR) technique described in Chapter 2, of the oxygen bridged ( $\mu$ -oxo/ $\mu$ -hydroxo) from MnCat, where the oxygen is labelled with the magnetically active isotope  $^{17}O$  ( $I = 5/2$ ), is presented in Chapter 3. The aim is to obtain an explanation about the oxygen bridges and their role: as both a structural element and as a substrate derivative of the catalysed reaction.

## 2. MATERIALS AND METHODS

EPR spectroscopy is particularly useful when it is applied to study intermediate states of redox-active metalloproteins. EPR provides information about the total spin of the system and its oxidation state, as well as a better understanding of its structure and function. Furthermore, double resonance techniques provide information about the first coordination sphere of the metal centre.

Metallocofactors, such as the  $Mn_4O_5Ca$  cluster of PS II, which perform electron transfer and multistep redox reactions, are particularly well suited to study by EPR spectroscopy.<sup>39</sup> The aim of this chapter is to introduce the basic theoretical and methodological aspects of EPR.<sup>40-44</sup> This overview will provide the background information necessary to understand the application of EPR to exchange-coupled transition-metal complexes through the effective spin Hamiltonian and the spin projection formalism.<sup>45</sup>

### 2.1. The Spin Hamiltonian Formalism

The spin Hamiltonian formalism, first described in the work of Abragam and Pryce,<sup>46</sup> is used to interpret all EPR measurements described in this thesis. The complete static spin Hamiltonian which describes an arbitrary spin system i.e. one containing  $i$  unpaired electron spins and  $k$  nuclear spins, includes the following terms parameterizing the interaction of the unpaired electron spin with other unpaired spins, nuclear spins, and the interaction of the electron spins and nuclear spins with the external magnetic field:

$$H = H_{EZ} + H_{ZFS} + H_{HF} + H_{NZ} + H_{NQ} + H_{EX} \quad (\text{Eq. 2.1})$$

$$= \sum_i \beta_e \vec{B}_0 \cdot \hat{g}_i \cdot \vec{S}_i + \sum_i \vec{S}_i \cdot \hat{D}_i \cdot \vec{S}_i + \sum_i \sum_k \vec{S}_i \cdot \hat{A}_{ik} \cdot \vec{I}_k - \sum_k g_n \beta_n \vec{B}_0 \cdot \vec{I}_k + \sum_k \vec{I}_k \cdot \hat{P}_k \cdot \vec{I}_k - 2 \sum_{i < j} \vec{S}_i \cdot \hat{J}_{ij} \cdot \vec{S}_j,$$

where  $H_{EZ}$  is the electron Zeeman interaction;  $H_{ZFS}$  is the zero field splitting term;  $H_{HF}$  is the hyperfine interaction between bound electron spins and nuclear spins;  $H_{NZ}$  is the nuclear Zeeman

interaction;  $H_{NQ}$  is the nuclear quadrupole interactions for spins with nuclear quantum numbers  $I > 1/2$ ; and  $H_{EX}$  is the spin-spin exchange interaction.

The basis set of the spin system with  $i$  electron spins of unpaired electrons and  $k$  nuclear spins, is formed as a product of the eigenstates of the interacting spins using the initial uncoupled wave functions and taking the following form:

$$|S_i \dots S_n M_i \dots M_n I_i \dots I_k m_i \dots m_k\rangle, \quad (\text{Eq. 2.2})$$

where  $S_i$  is the; electron spin of unpaired electron(s);  $M_i$  is its magnetic sub-level (projection on the magnetic field axis);  $I_j$  is the nuclear spin of a particular nucleus  $j$ ;  $m_j$  is its magnetic sub-level.

The interactions described in Eq. 2.1 are described below.

### **2.1.1. Electron and nuclear Zeeman interaction**

The electron Zeeman interaction describes the interaction between the magnetic moment  $\vec{\mu}$  of the unpaired electron spin with the external static magnetic field  $\vec{B}_0$ :

$$H_{EZ} = \beta_e \vec{B}_0 \cdot \hat{g} \cdot \vec{S} = \beta_e \vec{B}_0 (\vec{L} + g_e \vec{S}), \quad (\text{Eq. 2.3})$$

where  $\beta_e$  is the Bohr magneton;  $g_e = 2.0023193043737$  is the Lande g-factor of the free electron.

The  $\hat{g}$  tensor represents the interaction matrix which describes the magnetic moment associated with a given spin, which need not be the same in all directions, in this instance relative to the laboratory frame, defined by the external magnetic field ( $\vec{B}_0$ ). It is a symmetric matrix with the dimension 3x3 in the laboratory coordinate system and can be transformed to a diagonal form in the principal axis frame via rotation. The matrix is defined by the diagonal elements of the  $\hat{g}$  tensor, which are called principal values ( $g_x, g_y, g_z$ ) and the three Euler angles  $\alpha, \beta$  and  $\gamma$  of the rotation. These three angles describe the orientation of a protein crystal's principal axes in the laboratory frame. Typically, the

principal axis frame can be difficult as the molecular frame of a particular paramagnetic cofactor, and all interaction tensors are referred to within this frame.

The orientation dependence (anisotropy) can be understood primarily as a manifestation of spin-orbit coupling. The ground spin state of molecules in many cases is non-degenerate and the orbital angular momentum  $\vec{L}$  is quenched ( $L = 0$ ) leading to an isotropic g-tensor (the same in all directions). However, the coupling of the ground spin state with excited states can lead to a deviation from this simple picture. The spin-orbit coupling operator can be written in the form:

$$H_{SO} = \lambda \vec{L} \vec{S}, \quad (\text{Eq. 2.4})$$

the orbital angular momentum mixes with the spin, introducing a second-order contribution to the  $g$  values. Here,  $\lambda$  is the effective spin-orbit coupling constant. Since these second-order contributions are inversely proportional to the energy difference between the ground state and excited states, the deviation from  $g_e$  can be significant if the energy levels are close to each other.

The spin Hamiltonian term for the nuclear Zeeman interaction, which describes the coupling between the nuclear spin  $\vec{I}$  and the external magnetic field  $\vec{B}_0$  is as follows:

$$H_{NZ} = -\beta_n \vec{B}_0 \cdot \hat{g}_n \cdot \vec{I} = -g_n \beta_n \vec{B}_0 \cdot \vec{I}. \quad (\text{Eq. 2.5})$$

For a particular nucleus, the nuclear  $g_n$  factor and the nuclear spin quantum number are its intrinsic properties. The nuclear Zeeman interaction can be considered isotropic in most of the EPR experiments, and this approximation will be used throughout this work.

### 2.1.2. The Zero-Field Splitting

In a system with multiple unpaired electrons the strong interaction between the individual electron spins needs to be considered. The degeneracy of the total spin states and their magnetic sublevels  $M_S$  in the energy ladder is lifted by this interaction and this splitting, which is independent of the external magnetic field. When dealing with an effective spin  $S > 1/2$ , the zero field splitting term of the general spin Hamiltonian can be expressed by the following effective Hamiltonian:

$$\hat{H}_{ZFS} = \vec{S} \cdot \hat{d} \cdot \vec{S}, \quad (\text{Eq. 2.6})$$

where  $\hat{d}$  is a symmetric tensor which can be diagonalized in its principal axes. Due to the absence of the isotropic component in the fine structure interaction, the diagonalized tensor is traceless. In this way, the energy splitting of the  $M_S$  sublevels of the spin manifold  $S$  at zero-field is defined by the principal components  $d_x$ ,  $d_y$ , and  $d_z$  of the traceless tensor  $\hat{d}$ . These three components are not all independent and are expressed in terms of two parameters the axial ( $D$ ) and rhombic ( $E$ ) terms:

$$d_x = -\frac{1}{3}D + E, \quad d_y = -\frac{1}{3}D - E, \quad d_z = \frac{2}{3}D. \quad (\text{Eq. 2.7})$$

The ZFS term then can be rewritten as:

$$H_{ZFS} = d_x S_x^2 + d_y S_y^2 + d_z S_z^2 = D \left[ S_z^2 - \frac{1}{3} S(S+1) \right] + E(S_x^2 - S_y^2), \quad (\text{Eq. 2.8})$$

where  $D = \frac{3}{2}d_z$  and  $E = \frac{1}{2}(d_x - d_y)$  – axial and rhombic ZFS parameters.

### 2.1.3. The Hyperfine Interaction

The interaction between an electron and a nuclear spin is called the hyperfine interaction. The hyperfine interaction term of the spin Hamiltonian takes the form:

$$H_{HF} = \vec{S} \cdot \hat{A} \cdot \vec{I}, \quad (\text{Eq. 2.9})$$

where  $\hat{A}$  is defined as the hyperfine tensor. This Hamiltonian consists of an isotropic and anisotropic term ( $\hat{A} = A_{iso} + \hat{A}_{aniso}$ ).

The isotropic part comes from the interaction (overlap) of the electron spin density and the nucleus and is thus a property of s-orbitals. It is described by the Fermi contact interaction and defined by the following Hamiltonian:

$$H_{FC} = A_{iso} \vec{S} \cdot \vec{I} = \frac{8\pi}{3} g_e \beta_e g_n \beta_n \delta(r) \cdot \vec{S} \cdot \vec{I}, \quad (\text{Eq. 2.10})$$

with the isotropic hyperfine interaction constant  $A_{iso}$ , which is proportional to the electron spin density at the nucleus and the nuclear  $g_n$ . Thus, it differs depending on isotope or type of nucleus. When the spin arises from an unpaired electron in a p, d or f orbital, a non-zero spin density at the nucleus emerges due to spin polarization. This results in the presence of an anisotropic hyperfine component. The anisotropic part represents classical electron-nuclear dipole-dipole coupling, and it is described by the following Hamiltonian:

$$H_{DD} = \vec{S} \cdot \hat{A}_{aniso} \cdot \vec{I} = g_e \beta_e g_n \beta_n \left[ \frac{3(\vec{S} \cdot \vec{r})(\vec{r} \cdot \vec{I})}{r^5} - \frac{\vec{S} \cdot \vec{I}}{r^3} \right], \quad (\text{Eq. 2.11})$$

with a dipolar coupling tensor  $\hat{A}_{aniso}$ , which is typically traceless and symmetric in its principal axis system. If the spin density is located in s-orbitals, the average dipole-dipole interaction is cancelled out.

### 2.1.4. Nuclear Quadrupole Interaction

Nuclei with nuclear spin quantum number  $I \geq 1$  exhibit a non-spherical charge distribution due to a nuclear electrical quadrupole moment  $Q$ . The nuclear quadrupole interaction is the interaction of this charge distribution with an electric field gradient caused by the surrounding electrons and nuclei. The corresponding spin Hamiltonian is

$$H_{NQ} = \vec{I} \cdot \hat{P} \cdot \vec{I}, \quad (\text{Eq. 2.12})$$

where  $\hat{P}$  is the nuclear quadrupole tensor, parameterized in its principal axis system where the nuclear quadrupole interaction matrix is traceless. Subsequently, the Hamiltonian can be expanded as

$$H_{NQ} = P_x I_x^2 + P_y I_y^2 + P_z I_z^2 = \frac{3}{2} P_z \left[ \left( I_z^2 - \frac{1}{3} I(I+1) \right) + \frac{1}{3} \eta (I_x^2 - I_y^2) \right], \quad (\text{Eq. 2.13})$$

with the convention  $|P_z| \geq |P_y| \geq |P_x|$  and the asymmetry parameter  $\eta$  defined as

$$\eta = \left| \frac{P_x - P_y}{P_z} \right|, \quad (\text{Eq. 2.14})$$

where  $0 \leq \eta \leq 1$ . The largest absolute principal value of the quadrupole tensor is given by

$$P_z = \frac{e^2 q Q}{h \cdot 2I(2I-1)}, \quad (\text{Eq. 2.15})$$

where  $eq$  is the electric field gradient. The quadrupole tensor is normally expressed in terms of the two parameters  $e^2 q Q/h$  and  $\eta$  which are related to the diagonal matrix by:

$$P = P_z \begin{pmatrix} -(1-\eta) & 0 & 0 \\ 0 & -(1+\eta) & 0 \\ 0 & 0 & 2 \end{pmatrix} = \frac{e^2 q Q}{h \cdot 4I(2I-1)} \begin{pmatrix} -(1-\eta) & 0 & 0 \\ 0 & -(1+\eta) & 0 \\ 0 & 0 & 2 \end{pmatrix} \quad (\text{Eq. 2.16})$$

### ***2.1.5. The Electron Exchange Interaction***

For overlapping electronic orbitals, the electronic wave function has to be anti-symmetric with respect to the exchange of electrons. This results in a difference in the Coulomb interaction for states with parallel and antiparallel spins and therefore in their respective energies. This interaction can be described by the Heisenberg-Van Fleck exchange Hamiltonian as follows:

$$\hat{H}_{EX} = -2J\vec{S}_1 \cdot \vec{S}_2 \quad (\text{Eq. 2.17})$$

Here,  $J < 0$  corresponds to an antiferromagnetic exchange interaction (a weak bonding situation) and  $J > 0$  to a ferromagnetic interaction (a weak anti-bonding situation).

## 2.2. The Spin Hamiltonian of the Mn Cluster of the OEC.

The Mn-cluster of the OEC represents an exchange coupled spin system. In the  $S_2$  state, the oxidation states of the four manganese ions are  $Mn^{III}Mn^{IV}Mn^{IV}Mn^{IV}$ .<sup>47</sup> Describing such a complicated spin system requires building a basis set from the product of the eigenstates of the four interacting spins:

$$|S_1 S_2 S_3 S_4 M_1 M_2 M_3 M_4 I_1 I_2 I_3 I_4 m_1 m_2 m_3 m_4\rangle, \quad (\text{Eq. 2.18})$$

where  $S_i$  is the electronic spin state of  $Mn_i$ ,  $M_i$  is the electronic magnetic sub-level of  $Mn_i$ ,  $I_i$  is the nuclear spin state of  $Mn_i$ , and  $m_i$  is the nuclear magnetic sub-level of  $Mn_i$ .  $S_i$  takes the value 2 for  $Mn^{III}$  and 3/2 for  $Mn^{IV}$ ;  $M_i = -S_i, -S_i + 1, \dots, S_i$ ;  $I_i$  takes the value 5/2 for  $^{55}Mn$  (100% natural abundance);  $m_i = -I_i, -I_i + 1, \dots, I_i$ .

The Spin Hamiltonian that describes the spin manifold of the Mn tetramer is the following:

$$H = \sum_i \beta_e \vec{B}_0 \cdot \hat{g}_i \cdot \vec{S}_i - \sum_i g_n \beta_n \vec{B}_0 \cdot \vec{I}_i + \sum_i \vec{S}_i \cdot \hat{a}_i \cdot \vec{I}_i + \sum_i \vec{I}_i \cdot \hat{p}_i \cdot \vec{I}_i + \sum_i \vec{S}_i \cdot \hat{d}_i \cdot \vec{S}_i - 2 \sum_{i < j} \vec{S}_i \cdot \hat{J}_{ij} \cdot \vec{S}_j \quad (\text{Eq. 2.19})$$

Including: i) an electronic Zeeman term for each Mn ( $g_i$ ) ion; ii) a nuclear Zeeman term for each  $^{55}Mn$  ( $g_n$ ); iii) an electron-nuclear hyperfine term for each  $^{55}Mn$  ( $a_i$ ); iv) a nuclear quadrupole term for each  $^{55}Mn$  ( $p_i$ ); v) a fine structure term for each Mn ( $d_i$ ) ion; vi) pair-wise exchange terms for each Mn-Mn ( $J_{ij}$ ) interaction. It is however possible to simplify this spin Hamiltonian. As the exchange interaction term is significantly greater than any other term in the spin Hamiltonian, it is possible to describe the system with an effective electronic spin state, using a single electron spin quantum number instead of four, the total spin  $S_T$ . This simplified spin Hamiltonian is sufficient to rationalize the EPR signal seen for the OEC, the so called multiline signal, which can be described as arising from the ground state of a ladder of effective spin states of total spin  $S_T = 1/2$ .<sup>47, 48</sup> The basis

set in that case is simplified, including only the effective electronic spin  $S_T = 1/2$  and the nuclear spin of each  $^{55}\text{Mn}$  nucleus. The wave functions of this basis set are given by:

$$\left| \frac{1}{2} \ M \ m_1 \ m_2 \ m_3 \ m_4 \right\rangle, \quad (\text{Eq. 2.20})$$

where  $M = \pm \frac{1}{2}$  and  $m_i = -\frac{5}{2}, -\frac{3}{2}, \dots, \frac{5}{2}$ .

The effective spin Hamiltonian that describes the ground state of the spin manifold ( $S_T = 1/2$ ) is:

$$H = \beta_e \vec{B}_0 \cdot \hat{G} \cdot \vec{S} + \sum_i \left( g_n \beta_n \vec{B}_0 \cdot \vec{I}_i + \vec{S} \cdot \hat{A}_i \cdot \vec{I}_i \right). \quad (\text{Eq. 2.21})$$

It consists of: i) the Zeeman term for the total electronic spin; ii) Zeeman terms for each  $^{55}\text{Mn}$  nucleus; iii) hyperfine terms for each  $^{55}\text{Mn}$  nucleus. Quadrupole terms are neglected for the  $^{55}\text{Mn}$  nuclei since they are considered to only have a small contribution to the energy levels (eigenstates) of the system.

### 2.3. The Spin Hamiltonian of the $^{17}\text{O}$ -Mn Cluster of the OEC.

We can extend the above effective spin Hamiltonian description to also include the coupling of ligand nuclei to the electronic spin e.g. the interaction of the OEC with labelled oxygen ligands ( $^{17}\text{O}$   $I = 5/2$ , natural abundance 0.038%).<sup>49</sup> The basis set describing this system is given by:

$$\left| \frac{1}{2} \ M \ m_1 \ m_2 \ m_3 \ m_4 \ L \ k \right\rangle, \quad (\text{Eq. 2.22})$$

where  $M = \pm \frac{1}{2}$ ;  $m_i = -\frac{5}{2}, -\frac{3}{2}, \dots, \frac{5}{2}$ ;  $L = 5/2$  for  $^{17}\text{O}$  and  $k = -\frac{5}{2}, -\frac{3}{2}, \dots, \frac{5}{2}$ .

The effective spin Hamiltonian that describes the ground state of the spin manifold ( $S_T = 1/2$ ) is:

$$H = \beta_e \vec{B}_0 \cdot \hat{G} \cdot \vec{S} + \sum_i \left( g_n \beta_n \vec{B}_0 \cdot \vec{I}_i + \vec{S} \cdot \hat{A}_i \cdot \vec{I}_i \right) + g_o \beta_o \vec{B}_0 \cdot \vec{L} + \vec{S} \cdot \hat{C} \cdot \vec{L} + \vec{L} \cdot \hat{F} \cdot \vec{L} \quad (\text{Eq. 2.23})$$

It contains: i) the Zeeman term for the total electronic spin; ii) Zeeman terms for each  $^{55}\text{Mn}$  nucleus and the  $^{17}\text{O}$  nucleus; iii) hyperfine terms for each  $^{55}\text{Mn}$  nucleus and the  $^{17}\text{O}$  nucleus and iv) a quadrupole term for the  $^{17}\text{O}$  nucleus. Here the quadrupole terms for the  $^{55}\text{Mn}$  nuclei are also neglected since they are considered to only have a small contribution to the energy levels of the system.

## 2.4. EPR spectroscopy techniques and spectral analysis

The basic EPR experiment uses microwave (mw) radiation at a constant frequency and a varying external magnetic field. When the mw radiation energy ( $h\nu$ ) matches the field-dependent energy difference between spin states ( $\Delta E$ ), the absorption of the mw radiation is detected. This is described by the resonance condition:

$$h\nu = \Delta E = g_{eff} \beta_e B_0, \quad (\text{Eq. 2.24})$$

where  $g_{eff}$  is the effective g-value, which corresponds to the field position where the transition appears in the spectrum. The resulting EPR line is broadened due to homogenous effects related to relaxation processes as well as inhomogeneous mechanisms of broadening, like the broadening due to unresolved hyperfine interactions. The selection rule for allowed transitions in an EPR experiment is ( $\Delta M_S = 1$  and  $\Delta M_I = 0$ ), although in some circumstances spin forbidden transitions can gain intensity. EPR experiments can be performed at different mw frequency bands. Higher frequencies lead to a better resolution of the g tensor improving the orientation selectivity but often at the expense of the EPR linewidth. The mw frequency bands used in this work are X- (9 GHz), Q- (35 GHz) and W-band (94 GHz). The various EPR techniques used in this work will be described below.

### 2.4.1. Continuous-Wave (cw) EPR

The cw EPR experiment uses continuous microwave radiation at a fixed frequency. The external magnetic field is then scanned changing the separation of energy levels of the spin system. When it matches the resonance condition the spin system is able to absorb the mw radiation. A net microwave absorption is observed due to the thermodynamic difference in populations of separated energy levels, which is described by the Maxwell-Boltzmann distribution, written as follows for a two-level system as a ratio of populations:

$$\frac{n_{+\frac{1}{2}}}{n_{-\frac{1}{2}}} = \exp\left(-\frac{\Delta E}{k_B T}\right), \quad (\text{Eq. 2.25})$$

where  $k_B$  is the Boltzmann constant and  $T$  is the temperature in Kelvin. The population difference between the two levels, however, is very small. For example, under standard conditions at X-band the difference in populations is only about 0.2%. It is noted that the comparatively small population difference between the energy levels allows the exponential function in Eq. 2.26 to be approximated as a linear function:

$$\Delta N = n_{+\frac{1}{2}} - n_{-\frac{1}{2}} = \frac{\Delta E}{2k_B T} \quad (\text{Eq. 2.26})$$

It is easily observed that the population difference (and thus the magnitude of the EPR signal) is enhanced by decreasing the temperature and by performing the EPR experiment at higher microwave frequencies (with corresponding higher magnetic fields).

The sensitivity of the EPR technique is defined as the minimum number of detectable spins, which is dependent on microwave power  $P$ , resonance frequency  $\nu$ , sample volume  $V$  and the unloaded quality factor of the resonator  $Q$  in the following way:

$$N_{\min} \propto VQ^{-1}\nu^{-2}P^{-\frac{1}{2}}. \quad (\text{Eq. 2.27})$$

In order to increase sensitivity, higher mw powers are used to enhance the EPR signal. Higher powers are only beneficial if the spin system can relax back to thermal equilibrium (longitudinal relaxation ( $T_1$ ) is fast enough). If this is not the case, saturation of the EPR signal takes place and the signal intensity will decrease with increasing power. Thus the optimum way to conduct a cw EPR experiment is working in the unsaturated regime. High temperatures can prevent saturation problems, since relaxation processes slow down at low temperatures. Therefore, the best experiment performance is achieved when both effects, power and temperature, are taken in account.

### **2.4.2. Pulse EPR techniques**

Contrary to the cw EPR technique, where continuous mw radiation is applied, in pulse EPR employs short mw pulses to induce EPR transitions. The typical mw pulses have a length in the

range of few ns and high power (1 kW) at a certain frequency to drive the spin transitions of the system. The vector model that describes the evolution of the net magnetization vector  $\vec{M}$  in time explains the spin dynamics induced by the pulses. In this model, each spin centre that belongs to the system is aligned parallel or perpendicular to the applied field  $\vec{B}_0$  with the consequence being that only a fraction of the sample is EPR active (as above see 2.4.1). The excess spin population will be mainly in the lower energy state at thermal equilibrium and can be considered a macroscopic quantity i.e. a net magnetization vector  $\vec{M}$  aligned with the external field  $\vec{B}_0$ ; which is generally labelled the z-axis. When a second magnetic field  $\vec{B}_1$  perpendicular to  $\vec{B}_0$  is introduced by a mw pulse, the magnetization is transiently flipped into the xy plane.  $\vec{M}$  precesses about the applied magnetic field axis (z-axis) at a frequency of rotation characteristic of each non-equivalent spin, termed the Larmor frequency. The transverse magnetization in the xy-plane is detected as the EPR signal. Finally, due to the spin lattice relaxation ( $T_1$ ) processes the system will recover to the original state, meaning that the precession of  $\vec{M}$  is damped. The simplest pulse EPR experiment is termed the Free Induction Decay (FID), where after applying a  $\pi/2$  pulse the decay of the  $\vec{M}$  in the xy-plane can be monitored (see Figure 10).

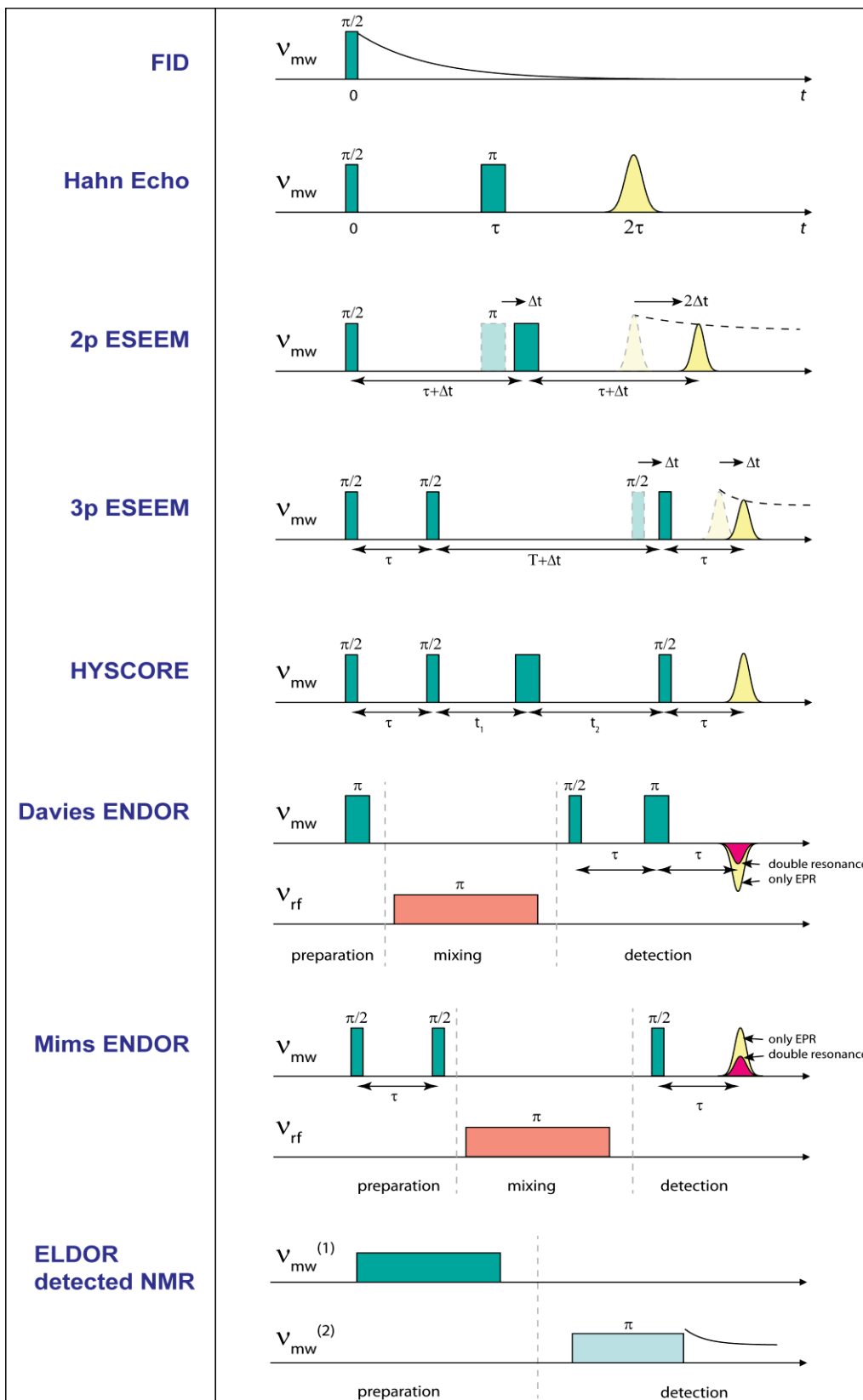


Figure 10. EPR techniques used in this work , described in the text below.

Moreover, due to inhomogeneity of the spin ensemble, different spins precess with slightly different frequencies, causing the defocusing of  $\vec{M}$  and corresponding signal decay with characteristic transverse (spin-spin) relaxation time ( $T_2$ ). The defocusing process can be reversed by extending the FID experiment with the second  $\pi$  pulse after a short delay  $\tau$ , then at the moment  $t = 2\tau$  the net magnetization is refocused, giving the EPR signal. This sequence is called electron spin echo (ESE) or the Hahn echo experiment.<sup>50</sup>

The advantage of Pulse EPR over CW-EPR is that it can reveal transitions that are not resolved in the EPR spectrum e.g. the splitting of the EPR signal due to ligand hyperfine interactions. This is achieved by microwave pulse sequences in which *selected* transitions of the spin manifold are viewed in isolation. Such measurements are termed double resonance techniques and include: Electron Nuclear DOuble Resonance (ENDOR), Electron Spin Echo Envelope Modulation (ESEEM), HYperfine Sublevel CORrElation (HYSCORE), and ELeCtron electron DOuble Resonance detected NMR (ELDOR-detected NMR or ED-NMR). A brief description of these methods is listed below:

#### ***2.4.2.a. Two and Three-Pulses Electron Spin Echo (ESE) Envelope Modulation (ESEEM)***

Electron Spin Echo Envelope Modulation (ESEEM) spectroscopy is based on the modulation of the relaxation-induced decay of an ESE signal which is encoded with the transition frequencies of coupled nuclear spins. Thus, ESEEM indirectly probes nuclear transitions. The resulting modulations in the decay curve of ESE in the time-domain spectrum can be converted into a frequency domain spectrum by subtraction of the decay background of the spin echo and a subsequent Fourier transformation. Information about the nature of the nuclei that are coupled to the electron spin, hyperfine coupling of the nuclei and nuclear quadrupole interaction (for  $I \geq 1$ ) can be obtained from the observed resonance frequencies in the frequency domain spectrum.

The simplest ESEEM experiment uses the two-pulse Hahn echo sequence<sup>50</sup>. The echo signal decay, which is modulated with the nuclear transition frequencies, is monitored while sweeping the time delay ( $\tau$ ) between the  $\pi/2$  and  $\pi$  mw pulses<sup>51</sup>. In the two-pulse ESEEM method, nuclear transition frequencies are observed along with the combinational frequencies (i.e. their sums and differences). In two-pulse ESEEM experiments the lines are typically broadened, since the linewidth is determined by the electron phase memory time, which is normally significantly shorter than that of nuclear spins<sup>41</sup>. The resolution of ESEEM spectra can be increased by the use of a three-pulse ESEEM technique, where the pulse sequence is based on detection of a stimulated echo<sup>52</sup>. In this case, the experiment follows the decay of a stimulated echo using a sequence of three  $\pi/2$  pulses instead of the Hahn echo. The echo modulation is recorded as the time delay  $T$  between the second and third pulses is increased. The spectral resolution is improved as compared to two-pulse ESEEM, since the linewidths are determined now by the electronic  $T_1$  time, which is much longer than the  $T_2$  time and approaches the phase memory time of the nuclear spins. Unlike two-pulse ESEEM, the three-pulse method does not produce lines at the nuclear combination frequencies, which simplifies the spectra. However, the three-pulse ESEEM experiment suffers from blind spots due to suppression of modulations at frequencies that are integer multiples of  $1/\tau$ . The problem can be solved by performing the measurements for several  $\tau$  values, which shifts the positions of the artefacts in the spectra. The positive effect of blind spots is that they can be used to suppress interfering transitions from background signals or strong matrix transitions by selecting an appropriate  $\tau$  value.

For both ESEEM techniques, the modulation effect arises from hyperfine anisotropy and disappears for an isotropic hyperfine interaction. A significant nuclear quadrupole interaction, however, can produce the effect even in the case of an isotropic hyperfine coupling. The nuclear transitions accessible in ESEEM spectroscopy are limited to low frequencies due to a bandwidth

limitation of the resonator (<50 MHz). Therefore, ESEEM spectroscopy must often be used in conjunction with other spectroscopic techniques, such as ENDOR or EDNMR.

#### **2.4.2.b. HYSORE**

The Hyperfine Sublevel Correlation is a 2D technique, based on the 3-pulse ESEEM sequence, with an additional  $\pi$ -pulse placed in between 2<sup>nd</sup> and 3<sup>rd</sup> pulses. Varying the spacing  $t_1$  and  $t_2$ , the time steps between the 2<sup>nd</sup> and 3<sup>rd</sup> pulse and the additional  $\pi$ -pulse, a 2D time domain spectrum can be obtained where the signal is modulated with the frequencies of connected nuclei. The additional pulse swaps the coherencies between  $m = +1/2$  and  $m = -1/2$  state. That allows hyperfine interactions that belong to the same electron spin manifold to be correlated, resolving overlapping signals in the 1D (ESEEM) experiment. As in ESEEM experiments, the time domain spectra are transformed to the frequency domain hyperfine spectra using Fourier transformation, with preliminary background subtraction.

#### **2.4.2.c. ENDOR**

Electron nuclear double resonance (ENDOR) spectroscopy is a powerful method for determining nuclear transition frequencies. In ENDOR, measurements nuclear transitions are directly induced by a second, radio-frequency (rf) field, which is applied in addition to the mw radiation. Pumping the nuclear transitions changes the populations of the spin manifold, which, in turn, affects the intensity of the observed EPR signal. The ENDOR signal is recorded as a change of the EPR signal intensity as a function of the swept rf field frequency.

The frequency-domain spectrum provides a selective probing of nuclear transitions. For a spin of  $S = 1/2$ , the resonance frequencies of transitions  $\nu_{\alpha/\beta}$  are: i) centred at half of the absolute hyperfine coupling and split by twice the Larmor frequency of the particular nucleus ( $\nu_n$ ) in the low field limit ( $2\nu_n < |a|$ ); ii) and centred at ( $\nu_n$ ) and split by  $|a|$  in the high field limit ( $2\nu_n > |a|$ )

according to the following equation:  $\nu_{\alpha/\beta} = \nu_n \pm |a|/2$  (see Figure 11). The presence of the nuclear quadrupole interaction (in nuclei with  $I > 1/2$ ) leads to further line structure.

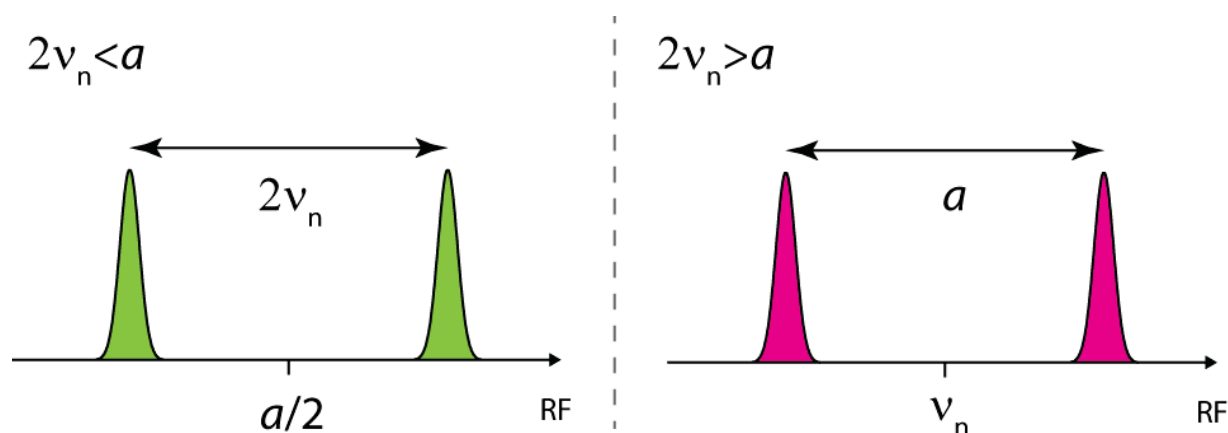


Figure 11. ENDOR signals for  $S=1/2$ ,  $I=1/2$  spin system: weak (left) and strong (right) field limits.

Pulse ENDOR techniques have a number of advantages over the classical cw ENDOR.<sup>41</sup> In pulse experiments the signal intensity does not critically depend on a balance between electron and nuclear relaxation times. Another advantage is a lower susceptibility to instrumental artifacts, since the mw and rf pulses are separated from the detection time.

#### 2.4.2.d. Davies ENDOR

The two most commonly used pulse ENDOR techniques were introduced by Mims<sup>53</sup> and Davies<sup>54</sup>. The Davies ENDOR experiment is based on the inversion recovery pulse sequence.<sup>54</sup> The preparation mw  $\pi$ -pulse is first applied and inverts the spin population of a single EPR transition (allowed EPR transition of the spin manifold), burning a hole in the EPR spectrum. The length of the preparation pulse defines the width of the burnt hole and thus the selectivity of the measurement. In the following step, a mixing period occurs where a selective rf pulse is applied. When the swept rf is in resonance with an NMR transition, magnetization of nuclear spin states is transferred to the other spin manifold, otherwise no mixing occurs to fill in the hole created by the inversion pulse.

Subsequently, the changed electron polarization is converted to observable electron coherence using a Hahn echo detection sequence.

The Davies ENDOR experiment is preferentially used to measure nuclei in the strong-coupling limit i.e. to nuclei with large hyperfine coupling values, particularly metal-centred hyperfine couplings. For weakly coupled nuclei the part of the ENDOR spectrum centred at the Larmor frequency is suppressed, due to lack of hyperfine contrast, a manifestation of the finite selectivity of the first microwave pulse. It is also noted that the ENDOR effect is less intense than the EPR signal (measured using a 2 pulse Hahn echo sequence) due to i) not entire nuclear spin ensemble is excited by the rf pulse; and ii) its stronger dependence on the slow  $T_1$  as the whole pulse sequence is much longer.

#### ***2.4.2.e. Mims ENDOR***

The Mims ENDOR pulse sequence is based on a stimulated echo sequence, the same used in 3 pulse ESSEM, with three microwave pulses separated by two time delays as follows:  $\pi/2$ - $\tau$ -  $\pi/2$ - $T$ - $\pi/2$ .<sup>53</sup> The first two microwave pulses prepare the system with the third microwave pulse used to read out the EPR signal. The rf  $\pi$  pulse used to induce nuclear transitions is applied between the second and third mw pulse during the time delay  $T$ . The first time delay,  $\tau$ , is limited by  $T_2$  and typically lasts several hundreds of ns, while the second delay,  $T$ , which is limited by  $T_1$ , lasts tens of  $\mu$ s. In contrast to the Davies ENDOR experiment, Mims ENDOR is superior for the detection of smaller hyperfine couplings but suffers from blind spots as seen in ESEEM. This problem can be overcome by recording spectra for different  $\tau$  values.

#### ***2.4.2.f. ELDOR-detected NMR***

The ELection-electron DOuble Resonance (ELDOR) detected NMR (EDNMR) technique, as with ENDOR, directly probes nuclear interactions of the spin manifold by the transfer of spin polarization between sublevels split by Zeeman and hyperfine interactions.<sup>53</sup> A second mw pulse that

pumps spin forbidden electronic transitions is used. The measured transition frequencies represent the nuclear transition +/- EPR transition. As the EPR frequency is known (and is observed in the EDNMR spectrum by a broad central line) nuclear frequencies can easily be deduced. EDNMR is more sensitive than ENDOR, in part because it is less restrained by  $T_1$  relaxation, as the pulse sequence length is much shorter.

A soft and highly selective pulse is swept around the resonance frequency ( $\nu_{mw1}$ ) to pump allowed and forbidden EPR transitions of the spin manifold ( $\Delta M_S = 1$  and  $\Delta M_I = 1$ ). When the pump pulse coincides with the forbidden electron transitions of the spin manifold at certain microwave frequency, the observed echo signal decreases, leading to apparent side-holes from the excited nuclear forbidden transitions of the spin manifold ( $\Delta M_I = 1$ ). In addition, allowed transitions of the spin manifold are excited by the pump pulse. This results in a frequency spectrum with a central hole of a Lorentzian lineshape around  $\nu_{mw1}$ . Typically transitions are located symmetrically around  $\nu_{mw1}$  separated from the center hole by  $\Delta\nu = \nu_{mw2} - \nu_{mw1}$ , which corresponds to the nuclear transition frequency. Performing EDNMR experiments at high field, such as W-band, allows signals from nuclei of a low nuclear  $g_n$  factor to be resolved, where the coupling of the nuclei to the electron spin is weak.<sup>21, 53</sup> At lower frequencies these would be hidden under the central hole. Furthermore, overlapping of signals of nuclei with similar nuclear  $g_n$  factor are better separated.

### **3. SUMMARY AND PUBLISHED PAPERS**

This chapter has an overview of the academic work produced during my PhD project. This work includes five journal articles, four of which are already published, and the remaining is still in preparation. My contribution to each study is described below:

#### **3.1. Ammonia binding to the oxygen-evolving complex of Photosystem II identifies the solvent-exchangeable oxygen bridge (u-oxo) of the manganese tetramer.**

- I collected most of the EPR experimental data.
- I performed part of the data simulations and modeling.
- I was involved in the production of the manuscript.

A. Boussac and M. Nowaczyk provided all biological samples. W. Ames and D. Pantazis performed all the DFT calculations.

A follow up article was published in Physical Chemistry Chemical Physics.

#### **3.2 Characterization of the Oxygen Bridged Manganese Model Complexes Using Multifrequency $^{17}\text{O}$ -Hyperfine EPR Spectroscopies and Density Functional Theory.**

- I was involved in the collection of the EPR experimental data, specifically the Mn-catalase sections;
- I performed part of the data simulations and modeling
- I was involved in the production of the manuscript

A. Boussac, J.J. Griese/M. Högbom + Mn catalase people + synthetic people provided all biological samples. W. Ames and D. Pantazis performed all the DFT calculations.

#### **3.3. Recent developments in biological water oxidation (review)**

- I was involved in the preparation of the manuscript.

### ***3.1. Ammonia binding to the oxygen-evolving complex of Photosystem II identifies the solvent-exchangeable oxygen bridge ( $\mu$ -oxo) of the manganese tetramer.***

*Montserrat Pérez Navarro, William M. Ames, Håkan Nilsson, Thomas Lohmiller, Dimitrios A. Pantazis, Leonid Rapatskiy, Marc M. Nowaczyk, Frank Neese, Alain Boussac, Johannes Messinger, Wolfgang Lubitz, and Nicholas Cox.*

*Published in the Proceedings of the National Academy of Sciences, 2013 Vol. 110 (39), pp 15561–15566.*

Ammonia, a water analogue, has been reported to bind to the OEC of PS II while not inhibiting oxygen evolution activity. In this study we show that the binding of ammonia to the OEC leads to a large change in  $^{17}\text{O}$  signals associated with the exchangeable oxygen ligands of the cofactor, including the fast exchanging  $\mu$ -oxo bridge of the cofactor, a candidate for one of the substrates. We further show that ammonia binding does not alter substrate exchange kinetics conclusively demonstrating that ammonia does not competitively displace a substrate water. We go on to show which non-catalytic water molecule ammonia does displace, namely a water ligand of the outer manganese  $\text{Mn}_{\text{A}4}$ , W1. Furthermore we show that W1 displacement is expected to strongly perturb the oxygen bridge *trans* to its position i.e. O5. This result requires that O5 is an exchangeable  $\mu$ -oxo bridge. This study ultimately provided new information that will be relevant to elucidate the mechanism of biological water splitting pointing to an oxo/oxyl mechanism involving O5.

A follow up article to this work was published in in Physical Chemistry Chemical Physics, 2014 Vol. 16 (24), pp 11877–11892.

# Ammonia binding to the oxygen-evolving complex of photosystem II identifies the solvent-exchangeable oxygen bridge ( $\mu$ -oxo) of the manganese tetramer

Montserrat Pérez Navarro<sup>a</sup>, William M. Ames<sup>a</sup>, Håkan Nilsson<sup>b</sup>, Thomas Lohmiller<sup>a</sup>, Dimitrios A. Pantazis<sup>a</sup>, Leonid Rapatskiy<sup>a</sup>, Marc M. Nowaczyk<sup>c</sup>, Frank Neese<sup>a</sup>, Alain Boussac<sup>d</sup>, Johannes Messinger<sup>b</sup>, Wolfgang Lubitz<sup>a,1</sup>, and Nicholas Cox<sup>a,1</sup>

<sup>a</sup>Max-Planck-Institut für Chemische Energiekonversion, D-45470 Mülheim an der Ruhr, Germany; <sup>b</sup>Department of Chemistry, Chemical Biological Centre, Umeå University, S-90187 Umeå, Sweden; <sup>c</sup>Plant Biochemistry, Ruhr-Universität Bochum, D-44780 Bochum, Germany; and <sup>d</sup>iBiTec-S, Centre National de la Recherche Scientifique Unité Mixte de Recherche 8221, Commissariat à l'Énergie Atomique Saclay, 91191 Gif-sur-Yvette, France

Edited by Brian M. Hoffman, Northwestern University, Evanston, IL, and approved August 13, 2013 (received for review March 6, 2013)

The assignment of the two substrate water sites of the tetramanganese penta-oxygen calcium ( $Mn_4O_5Ca$ ) cluster of photosystem II is essential for the elucidation of the mechanism of biological O-O bond formation and the subsequent design of bio-inspired water-splitting catalysts. We recently demonstrated using pulsed EPR spectroscopy that one of the five oxygen bridges ( $\mu$ -oxo) exchanges unusually rapidly with bulk water and is thus a likely candidate for one of the substrates. Ammonia, a water analog, was previously shown to bind to the  $Mn_4O_5Ca$  cluster, potentially displacing a water/substrate ligand [Britt RD, et al. (1989) *J Am Chem Soc* 111(10):3522–3532]. Here we show by a combination of EPR and time-resolved membrane inlet mass spectrometry that the binding of ammonia perturbs the exchangeable  $\mu$ -oxo bridge without drastically altering the binding/exchange kinetics of the two substrates. In combination with broken-symmetry density functional theory, our results show that (i) the exchangeable  $\mu$ -oxo bridge is O5 (using the labeling of the current crystal structure [Umena Y, et al. (2011) *Nature* 473(7345):55–60]); (ii) ammonia displaces a water ligand to the outer manganese ( $Mn_{A4}$ -W1); and (iii) as W1 is *trans* to O5, ammonia binding elongates the  $Mn_{A4}$ -O5 bond, leading to the perturbation of the  $\mu$ -oxo bridge resonance and to a small change in the water exchange rates. These experimental results support O-O bond formation between O5 and possibly an oxyl radical as proposed by Siegbahn and exclude W1 as the second substrate water.

PSII | OEC | water oxidizing complex | water-oxidation | Mn cluster

In oxygenic photosynthesis, light-driven water splitting is catalyzed by the oxygen-evolving complex (OEC) of the membrane bound, pigment-protein complex photosystem II (PSII). The OEC consists of an inorganic tetra-manganese penta-oxygen calcium ( $Mn_4O_5Ca$ ) cluster (1–3) and the nearby redox-active tyrosine residue  $Y_Z$  (D1-Tyr161) that couples electron transfer from the  $Mn_4O_5Ca$  cluster to P680, the photo-oxidant of PSII. The cluster resembles a “distorted chair”, where the base is formed by an oxygen-bridged ( $\mu$ -oxo) cuboidal  $Mn_3O_4Ca$  unit (1) (Fig. 1A). The fourth Mn ( $Mn_{A4}$ ) is located outside of the cuboidal unit and is linked via a  $\mu$ -oxo-bridged ligation (O4) to one of its corners ( $Mn_{B3}$ ). A second linkage between the outer Mn and the cube is provided by a fifth oxygen O5. The  $Mn_4O_5Ca$  cluster is also held together by six carboxylate ligands and has only one directly coordinating nitrogen ligand, D1-His332 (Fig. 1B).

The OEC cycles through a series of five intermediate states that are known as S states (4) (Fig. 1A):  $S_0$ ,  $S_1$  (dark stable),  $S_2$ ,  $S_3$ , and  $S_4$  (not yet isolated), where the subscript refers to the number of oxidizing equivalents stored in the OEC through successive electron withdrawals by  $Y_Z^+$ . In the 1.9-Å resolution structure, the S state of the cluster was assigned to be  $S_1$  (1). However, this is unlikely as all Mn-Mn, Mn-Ca, and Mn-O/N distances of the crystal structure are  $\sim 0.1$  Å longer compared with those determined by extended X-ray absorption fine structure

(EXAFS) spectroscopy (5–7). Moreover, the central O5 has unusually long bonds to three Mn ions and to the Ca ion, outside the range seen for model complexes. All these structural details suggest that the Mn ions of the cluster were photoreduced during X-ray data collection, and as such, the X-ray structure represents a nonphysiological, overreduced S state (8, 9). This structural ambiguity can be eliminated by combining the X-ray data with spectroscopic constraints and the introduction of computational modeling. In these unified models, O5 is generally considered to be a  $\mu$ -oxo bridge between  $Mn_{A4}$  and  $Mn_{B3}$  in the  $S_1$  and  $S_2$  states, rendering this unit bis- $\mu$ -oxo bridged, and  $Mn_{D1}$  as five coordinate (10–13) (Fig. 1B).

The  $S_2$  state is readily observed using EPR spectroscopy and related techniques. In this state, the four Mn ions of the OEC are coupled together, resulting in a ground electronic state with one unpaired electron, i.e., effective spin  $S_{eff} = 1/2$  (14). A distinctive “multiline” EPR spectrum is observed at liquid helium temperature, where the line splittings reflect the coupling of the four  $^{55}Mn$  magnetic nuclei to the unpaired electron spin (hyperfine interaction) (Fig. 1C). The unpaired electron of the  $Mn_4CaO_5$  cluster also couples to other magnetic nuclei in the vicinity of the OEC (e.g.,  $^{17}O$ ,  $^{14}N/^{15}N$ ,  $^1H/^2H$ ), such as those that coordinate the Mn ions, e.g.,  $^{17}O$ ,  $^{14}N/^{15}N$ ,  $^1H/^2H$ . These hyperfine couplings are sufficiently small so that the interactions are not directly observed by continuous wave (CW)-EPR spectroscopy. Such interactions can instead be detected using pulse magnetic resonance techniques that probe NMR transitions (15). Such techniques include electron spin echo envelope modulation (ESEEM), electron nuclear double resonance (ENDOR), and electron–electron double-resonance–detected NMR (EDNMR). Each technique is suited to probe specific electron–nuclear interactions of the OEC. For example, exchangeable oxygen sites of the OEC, which are potential substrate sites (16), have been recently studied with W-band EDNMR using  $^{17}O$  isotopic labeling (17). This methodology is particularly useful as it allows all water-exchangeable sites, including fully deprotonated Mn- $\mu$ -oxo bridges, to be observed. It is known from time-resolved membrane inlet mass spectrometry (TR-MIMS) that at least one substrate is bound in all S states and exchanges with bulk water on a seconds timescale (16, 18–20). In the equivalent EDNMR experiment performed in the  $S_1$  state, rapid mixing of PSII with  $^{17}O$ -labeled water led to the uptake of the  $^{17}O$  label at three

Author contributions: W.L. and N.C. designed research; M.P.N., W.M.A., H.N., T.L., D.A.P., L.R., A.B., and N.C. performed research; M.M.N. and A.B. contributed new reagents/analytic tools; M.P.N., W.M.A., H.N., T.L., D.A.P., L.R., F.N., A.B., J.M., and N.C. analyzed data; and M.P.N., D.A.P., A.B., J.M., and N.C. wrote the paper.

The authors declare no conflict of interest.

This article is a PNAS Direct Submission.

<sup>1</sup>To whom correspondence may be addressed. E-mail: wolfgang.lubitz@cec.mpg.de or nicholas.cox@cec.mpg.de.

This article contains supporting information online at [www.pnas.org/lookup/suppl/doi:10.1073/pnas.1304334110/-DCSupplemental](http://www.pnas.org/lookup/suppl/doi:10.1073/pnas.1304334110/-DCSupplemental).

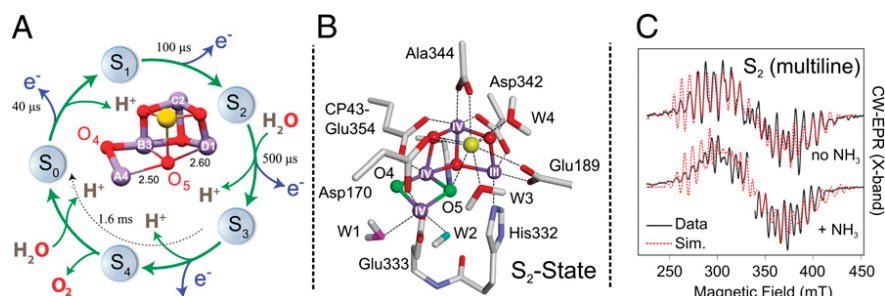


**Fig. 1.** (A) The S-state cycle of the OEC. The crystal structure of the manganese tetramer is also shown, indicating the unusual ligation of O5, equidistant between  $Mn_{A4}$  and  $Mn_{D1}$  (1). (B) A representative, unified DFT model of the OEC in the  $S_2$  state (10). The oxygen ligands W1 (pink), W2 (cyan), and O4/O5 (green) were assigned as sites exchangeable with solvent water in the  $S_1$  state (17). (C) The effect of ammonia on the CW-EPR (multiline) signal of the  $S_2$  state [11,29] (Fig. S1 and Table S1).

different Mn-ligand sites: (i) as one  $\mu$ -oxo bridge, most likely O4 or O5; (ii) as a terminal hydroxide ligand, most likely W2, a ligand of  $Mn_{A4}$ ; and (iii) as a terminal water ligand, most likely W1, also a ligand of  $Mn_{A4}$  (17). This latter species dominates the weakly coupled “matrix” envelope, which also has contributions from the Ca-bound waters (W3/W4) and second coordination shell  $H_2O$  ligands. These assignments are based on comparison with model compounds and the recent 1.9-Å resolution PSII crystal structure in conjunction with density functional theory (DFT) models (10).

Enzymological studies have indicated that there are at least two independent ammonia-binding sites, SYI and SYII (21, 22) in PSII. Ammonia binding at the SYI site is chloride-concentration dependent, is S-state independent, and results in the inhibition of oxygen-evolving activity (21–23), indicating that SYI likely represents one of the chloride sites identified in the crystal structure (1). In contrast, ammonia binding to SYII is independent of the chloride concentration (21, 22, 24, 25) and does not reduce  $O_2$  evolution. It binds only upon formation of the  $S_2$  state, to be subsequently released at some later point during the S state cycle (after  $S_3$ ), such that it is not bound upon return to the  $S_1$  state (26). SYII exhibits steric selectivity for small Lewis bases and appears to be only accessible to ammonia.

The ESEEM study by Britt et al. (25) demonstrated that SYII represents a Mn coordination site. Interestingly, the bound  $^{14}NH_3$  species displayed a large, rhombic quadrupole coupling ( $e^2Qq/h$ ) of 1.61 MHz, with  $\eta = 0.59$ . From comparison with model compounds, it was suggested that the ammonia is taken up as an amido bridge between either two Mn ions or one Mn ion and the Ca ion, i.e., replacing or modifying one  $\mu$ -oxo bridge of the complex. Low-frequency FTIR spectroscopy supports this basic hypothesis, identifying a putative Mn- $\mu$ O-Mn or Mn- $\mu$ O-Ca vibrational mode (27) lost upon ammonia addition (28).

Here we investigate the binding of ammonia to the OEC, using multiple-pulse EPR techniques and TR-MIMS. It is shown that, although ammonia significantly perturbs all exchangeable Mn-O ligand signals, it only moderately affects the exchange rates of both substrate waters. Instead of it displacing a  $\mu$ -oxo bridge, our data support a mechanism in which ammonia modifies the  $\mu$ -oxo bridge by displacing a water ligand *trans* to the bridge position, specifically the water ligand W1 *trans* to the  $\mu$ -oxo bridge O5. Broken symmetry (BS)-DFT calculations, which model this displacement, quantitatively reproduce all spectroscopic observables. Together, our data show that W1 is not a substrate binding site, but instead favor O5 as one of the two substrate waters.

## Results and Discussion

**Ammonia Binds to the OEC Without Significantly Changing Its Electronic Structure.** PSII isolated from the thermophilic cyanobacteria *Thermosynechococcus elongatus* was used throughout this study. Ammonia was added to PSII samples in the  $S_1$  state, which was advanced before the EPR measurements to the  $S_2$  state by low-temperature (180 K) illumination with visible light. In agreement with the literature, this resulted in an unperturbed  $S_2$ -state multiline EPR signal similar to the “no  $NH_3$ ” spectrum shown in Fig. 1C (26). Subsequent annealing of the sample to 260 K for 30 s led to the induction of the ammonia-modified multiline form ( $NH_3$  spectrum, Fig. 1C) (26). No change was observed in the background

cytochrome c550/b559 signals upon annealing the sample at 260 K. The ammonia-modified  $S_2$ -state multiline signal is also centered about  $g \approx 2.0$ , spread over the 250- to 430-mT field range and characteristically contains more hyperfine peaks than the control sample (at least 24 vs. 20; see Fig. 1C) (24, 29). Simulations of the EPR and  $^{55}Mn$ -ENDOR spectra using the spin Hamiltonian formalism are given in Fig. S1 and Table S1.

Nitrogen ligands of the OEC can be readily detected using ESEEM. In this type of pulse EPR experiment, the EPR signal intensity (spin echo) is recorded as a function of the time intervals between the successive microwave pulses. Signal intensity modulations arise from the weak coupling of the electron spin with nearby magnetic nuclei such as  $^{14}N$  [ $I(^{14}N) = 1$ ]. Both native  $^{14}N$ -PSII and universally labeled  $^{15}N$ -PSII [ $I(^{15}N) = 1/2$ ] were measured. X-band three-pulse ESEEM experiments of  $^{14}NH_3$ -containing PSII illuminated at 180 K and subsequently annealed at 260 K (see above) are shown in Fig. 2A and B. A new modulation, consistent with  $^{14}NH_3$  binding to the  $Mn_4O_5Ca$  cluster, is observed in the light-minus-dark difference spectra only after the 260-K annealing step (25). The bound  $^{14}NH_3$  species displays three sharp nuclear-quadrupole lines (N.Q.L.) at 0.5, 1.0, and 1.5 MHz in the Fourier-transformed spectrum (Fig. 2B). Spin Hamiltonian simulations of the lineshape are shown in Fig. 2A and B as dashed red lines and the fitted parameters (Table 1, Fig. S2, and Table S2) for *T. elongatus* are similar to those reported in the earlier higher-plant study (25). The relatively small magnitude of the hyperfine coupling supports the assignment of  $^{14}NH_3$  as a ligand to one of the  $Mn^{IV}$  ions as opposed to the  $Mn^{III}$  ion of the  $S_2$  state. This is because the  $Mn^{IV}$  ions carry a lower spin density (spin projection) than the  $Mn^{III}$  ion and thus their ligands are expected to display smaller effective hyperfine couplings (30).

In contrast to the X-band measurements, at Q-band, no difference is seen between the control and the  $^{14}NH_3$ -treated sample (Figs. 2C and 2D). Instead, the observed ESEEM modulation is dominated by a  $^{14}N$  hyperfine coupling assigned to the D1-His332 ligand of  $Mn_{D1}$  (31). At Q-band the histidine  $^{14}N$  signal is at or near the cancellation condition and as such displays a maximal ESEEM response (30, 31). As a consequence of the D1-His332  $^{14}N$  coupling matching the cancellation condition, the signal of the bound ammonia in comparison is suppressed at Q-band and no direct information on its binding site can be obtained in this way. However, the  $^{14}N$  histidine ESEEM signal, which resolves multiple spectral lines at 0.6, 2.0, and 7.3 MHz, and 14.8 MHz representing single-quantum (SQ) and double-quantum (DQ) transitions, respectively, can be used as spin probe reporting on the electronic structure and the oxidation state of  $Mn_{D1}$ . Spin Hamiltonian simulations of the lineshape of this signal are shown in Fig. 2C and D (dashed red lines). The parameters used (Table 1, Fig. S2, and Table S2) are similar to those reported earlier by Stich et al. (31) for PSII purified from *Synechocystis* sp. 6803. The relatively large magnitude of the D1-His332  $^{14}N$  coupling suggests that it is ligated to the only  $Mn^{III}$  ion in the  $S_2$  state, i.e., to the Mn ion that carries the largest spin density/spin projection (11, 30, 31). As the D1-His332 signal does not change upon the addition of ammonia, the oxidation state and ligand field of the  $Mn_{D1}$  ion cannot change. Thus, the binding site of ammonia at the manganese tetramer is unlikely to be proximal to the  $Mn_{D1}$  but instead is

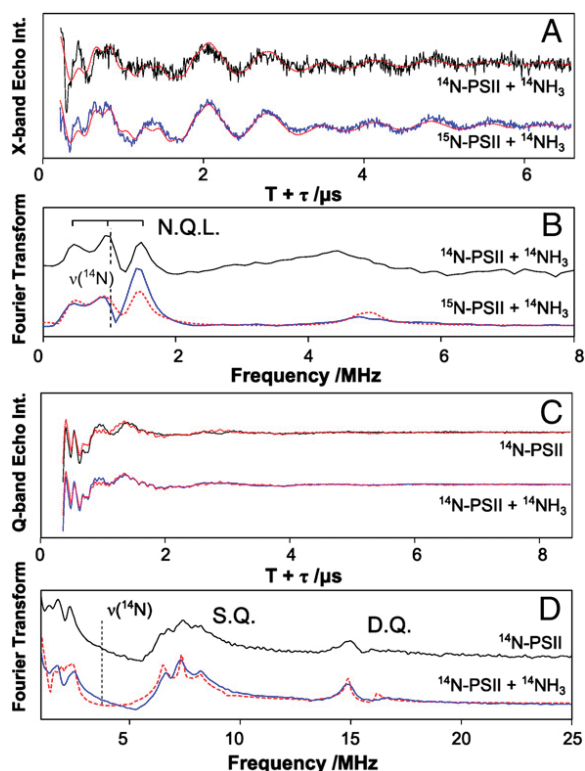


**Fig. 2.** (A) X-band three-pulse ESEEM traces measured at the center of the  $S_2$ -state multiline signal (Fig. 1,  $B_0 = 333$  mT, microwave frequency = 9.4 GHz). The data represent annealed-minus-dark difference traces collected on ammonia ( $^{14}\text{NH}_3$ )-treated  $^{14}\text{N}$ -PSII (black) and ( $^{14}\text{NH}_3$ )-treated  $^{15}\text{N}$ -PSII (blue). The traces shown in A were measured with an interpulse spacing  $\tau$  of 136 ns. Additional data traces using the  $\tau$ -values 152 ns, 168 ns, and 184 ns are shown in Fig. S2. (B) Fourier transform (FT) of the X-band time domain data. N.Q.L. identifies the nuclear-quadrupole lines caused by the coupling of the OEC with the added  $^{14}\text{N}$  ( $I = 1$ ). The spectrum shown represents the sum of the FT of the four ESEEM traces measured using different  $\tau$ -values (136–184 ns) to minimize spectral artifacts. (C) Q-band three-pulse ESEEM traces measured at the center of the  $S_2$ -state multiline signal ( $B_0 = 1.22$  T, microwave frequency = 34.0 GHz). The data represent light-minus-dark and annealed-minus-dark difference spectra of native  $^{14}\text{N}$ -PSII (black) and ammonia ( $^{14}\text{NH}_3$ )-treated  $^{14}\text{N}$ -PSII (blue) respectively. The time domain data were measured using an interpulse spacing  $\tau$  of 260 ns. Additional data traces using  $\tau$ -values of 240 ns and 300 ns are shown in Fig. S2. (D) Corresponding FT of the data traces presented in C. S.Q. and D.Q. identify single-quantum and double-quantum transition lines from the coupling with  $^{14}\text{N}$ -His332. The red dashed lines superimposing the data represent a simulation using the spin Hamiltonian formalism (*SI EPR Theory/Simulations*, Fig. S2, and Table S2). The label N.Q.L. identifies the quadrupole lines observed in the X-band  $^{14}\text{N}$ -ESEEM spectrum.

distal to it, consistent with  $\text{NH}_3$  binding to a  $\text{Mn}^{\text{IV}}$  ion. It is also noted that protons in the vicinity of the OEC can be readily detected using Q-band  $^1\text{H}$ -ENDOR (*SI EPR Theory/Simulations* and Fig. S3A). The addition of  $\text{NH}_3$  does not change the width of the signal envelope, which has been assigned to the protonated oxygen ligands on  $\text{Mn}_{\text{A4}}$  (32). The absence of a large proton coupling suggests ammonia does not replace one of the  $\mu$ -oxo bridges of the OEC, excluding this previous suggestion for its binding site (25).

**Ammonia Perturbs All Exchangeable Oxygen Ligands of the Manganese Tetramer.** EDNMR (32), a pump-probe technique, which employs two independent microwave pulses, has recently been shown to be the magnetic resonance method of choice for the detection of ( $^{17}\text{O}$ ) ligands of metallocofactors, such as the  $\text{Mn}_4\text{O}_5\text{Ca}$  cluster of the OEC. In this experiment, the EPR signal is monitored at a fixed microwave frequency matched to the resonator (probe

**Table 1.** Experimentally determined ESEEM and EDNMR spin Hamiltonian parameters: Comparison with calculated magnetic resonance parameters from DFT

Experiment/ Theory	Hyperfine couplings $ A_{\text{iso}} /\text{MHz}$			
	Exchangeable ligands, $^{14}\text{N}/^{17}\text{O}$			
	His332*, $^{14}\text{N}^*$	W1 $^{17}\text{O}/\text{NH}_3$ $^{14}\text{N}^*$	W2 $^{17}\text{O}^*$	O5 $^{17}\text{O}^*$
DFT				
Native	4.8	1.7	5.2	17.4
+ $\text{NH}_3^\ddagger$	5.2	1.5	4.3	12.2
$\Delta^{\S}$	0.4	—	−0.9	−5.2
$\Delta/\%^{\S}$	8.3	—	−17	−30
Experiment				
Native	7.2	1.4	4.5	9.7
+ $\text{NH}_3^*$	7.2	2.4	3.1	6.5
$\Delta^{\S}$	0.0	—	1.4	3.2
$\Delta/\%^{\S}$	0.0	—	−31	−28

\*Calculated (projected) BS-DFT hyperfine values directly comparable to experiment (MHz).

$^\ddagger$ Calculated (raw) BS-DFT hyperfine values are not directly comparable to experiment; the percentage change ( $\Delta$ ) due to ammonia binding can, however, be compared.

$^*$  $\text{NH}_3$  replacing W1.

$^{\S}$  $\Delta$  = difference between native and + $\text{NH}_3$  samples.

pulse). Before the detection sequence, a microwave pulse of varying frequency, termed the high turning-angle (HTA) pulse, is applied (pump pulse). The pumping (HTA) pulse drives spin-forbidden transitions where both the electron spin and the nuclear spin state change ( $|\Delta m_s| = 1$ ,  $|\Delta m_I| = 1$ ). Magnetic nuclei appear as doublets centered about their characteristic (Larmor) frequencies; i.e.,  $\nu_{\text{N}}(^{14}\text{N}) = 10.46$  MHz and  $\nu_{\text{N}}(^{17}\text{O}) = 19.6$  MHz at 3.4 T. As described in Rapatskiy et al. (17), in  $S_2$ -state PSII samples resuspended in  $\text{H}_2^{17}\text{O}$ -containing buffer, two structured signal envelopes are observed centered at the Larmor frequency and at twice the Larmor frequency of  $^{17}\text{O}$ . These two signal envelopes correspond to SQ and DQ transitions of exchangeable oxygen ligands of the manganese tetramer (Fig. 3A). Three components were identified (17): (i) a large coupling, assigned to a  $\mu$ -oxo bridge from comparison with model complexes, most likely O4 or O5; (ii) an intermediate coupling, assigned to the terminal oxygen ligand of  $\text{Mn}_{\text{A4}}$  (W2); and (iii) a weak coupling (unsplit matrix line), representing the second terminal oxygen ligand of  $\text{Mn}_{\text{A4}}$  (W1) but also including contributions from W3 and W4. The couplings of W1 and W2 are proposed to differ due to their protonation state. In DFT models, W2 is preferentially a hydroxo ligand in the  $S_2$  state, whereas W1 represents a water ligand (10, 13). In comparison with the hydroxo ligand (W2), the water ligand (W1) is expected to have a much smaller coupling, owing to its additional covalent bond to hydrogen, which weakens its bond to the  $\text{Mn}^{\text{IV}}$  ion.

Ammonia binding to the OEC modifies the  $^{17}\text{O}$  signal profile (17) (Fig. 3A and Fig. S4). The widths of the  $^{17}\text{O}$  single- and double-quantum envelopes narrow by  $\sim 30\%$ , and the splitting of the two outer single-quantum satellite peaks, which corresponds to the large coupling ( $\mu$ -oxo bridge), becomes unresolved. Additionally, the sharp central matrix line (W1) appears to be of lower intensity.

The intermediate coupling is best resolved in the double-quantum region, owing to spectral congestion in the single-quantum region. Ammonia binding modifies the intermediate-coupling feature, narrowing it by  $\sim 1$ –2 MHz. Furthermore, the whole double-quantum region becomes more symmetric compared with the spectra of the control sample (Fig. 3A, Fig. S4, and Table S3); this asymmetry was previously thought to be due to the matrix signal (17). The reduced asymmetry in the double-quantum region is taken as additional evidence that the matrix component is

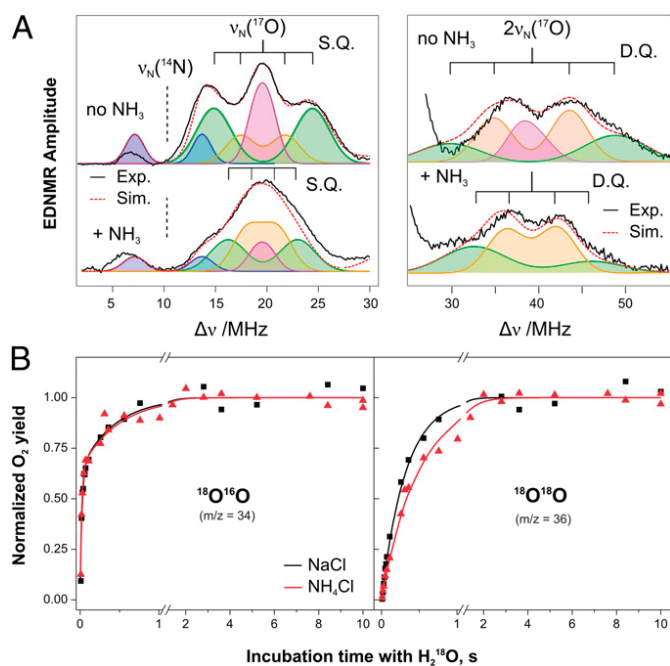


**Fig. 3.** (A) W-band  $^{17}\text{O}$ -EDNMR spectra of native and  $^{14}\text{NH}_3$ -treated  $^{14}\text{N}$ -PSII samples (17). The black line represents the data; the red dashed line represents the total simulation. Fitted isotropic hyperfine values are listed in Table 1. A complete list of parameters is given in Table S3. The colored traces represent the four components of the fit: the  $^{14}\text{N}$  of D1-His332, blue; the strongly coupled  $^{17}\text{O}$  species, green; the intermediately coupled  $^{17}\text{O}$  species, orange; and the weakly coupled  $^{17}\text{O}$  species, pink. (B) TR-MIMS traces monitoring substrate exchange in the  $S_2$  state at pH 7.6 in the presence of either 100 mM  $\text{NH}_4\text{Cl}$  (red triangles) or 100 mM NaCl (black squares). The lines represent biexponential ( $^{34}\text{O}_2$ , Left) and monoexponential ( $^{36}\text{O}_2$ , Right) fits.  $\text{NH}_4\text{Cl}$ :  $k_f = 52 \text{ s}^{-1}$ ,  $k_s = 2 \text{ s}^{-1}$ . NaCl:  $k_f = 38 \text{ s}^{-1}$ ,  $k_s = 3 \text{ s}^{-1}$ .

reduced by ammonia binding to the OEC, which is further supported by considering the power dependence of the EDNMR signal (for further details see *SI EPR Theory/Simulations* and Fig. S4). Thus, ammonia likely displaces W1, perturbing W2 and the  $\mu$ -oxo bridge signal. It is also noted that the water ligands of the  $\text{Ca}^{2+}$  ion (W3, W4) were measured independently using  $^{17}\text{O}$ -Mims ENDOR, and no change was observed; ergo, W3 and W4 are not displaced by ammonia (Fig. S3B).

**The Site of Ammonia Binding: A Mechanism for the Perturbation of the  $\mu$ -oxo Bridge.** The binding of ammonia as a terminal ligand to  $\text{Mn}_{\text{A}4}$  instead of W1 could potentially modify the hyperfine coupling of the  $\mu$ -oxo bridge O5 via the *trans* effect. To test whether this rationale can quantitatively explain the observed spectral changes, DFT calculations were performed using previously reported  $S_2$ -state OEC models consistent with geometric, thermodynamic, and spectroscopic parameters (10, 17). Calculated EPR parameters (33, 34) of both the W1- and the  $\text{NH}_3$ -containing structure are shown in Table 1 and Tables S2–S4. This single-ligand substitution quantitatively reproduces all experimental observables, including the  $^{14}\text{N}$  hyperfine and quadrupole couplings of the bound ammonia, the  $\sim 1$ -MHz decrease in the  $^{17}\text{O}$  hyperfine coupling of the terminal hydroxide (W2), and the  $^{14}\text{N}$ -His332 hyperfine coupling and its insensitivity to ammonia addition. Although it is currently not possible to reliably calculate projected hyperfine coupling constants for bridging ligands, as this is yet to be calibrated in model systems, it is possible to compare the raw BS-DFT values to ascertain the effect of the ammonia ligand. The calculations show that ammonia binding at the W1 site selectively perturbs the O5  $\mu$ -oxo bridge. The observed change in coupling is again quantitatively reproduced, with a decrease in the hyperfine coupling of O5 by 30%, the same

as seen for the  $\mu$ -oxo bridge species using EDNMR. All other  $\mu$ -oxo bridge couplings are calculated as being very similar for the  $\text{H}_2\text{O}$ - and the  $\text{NH}_3$ -containing structure, including the O4, which actually increases upon  $\text{NH}_3$  binding, excluding it as the exchangeable bridge. The only exception is O1, where the calculated raw BS-DFT hyperfine has a large percentage change; however, the absolute magnitude of the O1 hyperfine coupling is small and the absolute change is only 0.55 MHz (Table S4).

From this, we can confidently assign the site of  $\text{NH}_3$  binding to the W1 coordination site of  $\text{Mn}_{\text{A}4}$ . A comparison of the different geometries of the two BS-DFT structures (with and without  $\text{NH}_3$ ) shows a small elongation of the  $\text{Mn}_{\text{A}4}$ -O5 bond of 0.02 Å upon  $\text{NH}_3$  substitution, as expected. This bond lengthening reduces the  $\text{Mn}_{\text{A}4}$  to O5 spin polarization and consequently the overall spin density on O5, resulting in the 30% decrease in the observed  $^{17}\text{O}$  hyperfine value. This change should also modify the vibrational mode of the O5 bridge, consistent with low-frequency IR spectroscopic results reported in ref. 28. Indeed, vibrational frequencies computed for the optimized structures of the two models indicate that a  $\text{Mn}_{\text{A}4}$ -O5 stretching mode along the  $\text{Mn}_{\text{A}1}$ - $\text{Mn}_{\text{D}1}$  vector at  $644 \text{ cm}^{-1}$  shifts upon  $\text{NH}_3$  binding to  $617 \text{ cm}^{-1}$  with concomitant  $\sim 50\%$  loss in intensity, consistent with experimental observations.

**W1 Is Not a Substrate Water.** TR-MIMS, a mass spectrometric pump-probe technique, employing  $\text{H}_2^{18}\text{O}$  labeling, provides important information regarding the binding of the substrate to the catalyst during the S-state cycle (16). This experiment involves poisoning the OEC in the desired S state with light flashes and the subsequent rapid injection ( $t_{1/2} = 3 \text{ ms}$ ) of isotopically labeled water ( $\text{H}_2^{18}\text{O}$ ), followed by successive light flashes to release the product  $\text{O}_2$ . By varying the incubation time of the sample in labeled water, the extent to which  $^{18}\text{O}$  is incorporated into the product  $\text{O}_2$  is varied, allowing the determination of substrate water exchange rates with the bulk solvent. These experiments have established that the two substrate waters exchange with different rates that also vary independently with the S states. Thus, the two substrates bind at chemically distinct sites. The slowly exchanging substrate ( $W_s$ ) is bound throughout the S-state cycle, whereas the fast-exchanging substrate ( $W_f$ ) is bound latest in the  $S_2$  state (16, 18, 20, 35, 36).

TR-MIMS data monitoring the fast and slow substrate exchange in the  $S_2$  state at pH 7.6 in the presence of 100 mM  $\text{NH}_4\text{Cl}$  (red) or 100 mM NaCl (black) are shown in Fig. 3B. If ammonia displaces a substrate, a major slowing or even abolishment of one exchange rate is expected. This is not observed experimentally: The exchange rates of  $W_s$  and  $W_f$  with bulk water lie within factors of 1.5 in the presence and absence of  $\text{NH}_4\text{Cl}$ . This demonstrates that ammonia does not displace a substrate water, but instead slightly modifies exchange rates by binding in their vicinity. Thus, the combined EPR and TR-MIMS data exclude W1 as a substrate site. Importantly, these results exclude O-O bond mechanisms that involve both terminal Mn oxygen ligands on  $\text{Mn}_{\text{A}4}$ , i.e., the Kusunoki-type mechanism (37).

This model also provides a simple rationale for ammonia binding/release during the S-state cycle (24, 26). In the lower S states ( $S_0$ ,  $S_1$ ),  $\text{Mn}_{\text{A}4}$  is usually considered to be in the  $\text{Mn}^{\text{III}}$  oxidation state and is thus potentially five-coordinate, with W1 being only a weakly associated ligand. It is noted that DFT calculations support assigning the Jahn-Teller axis of  $\text{Mn}_{\text{A}4}^{\text{III}}$  along the W1/O5 axis (13, 38, 39). As such, ammonia does not bind in these S states as its nominal binding site is preferentially unoccupied. Upon formation of the  $S_2$  state, the  $\text{Mn}_{\text{A}4}$  is oxidized to +IV and is required to be six-coordinate, thus allowing ammonia to bind to the OEC. As  $\text{NH}_3$  is a better (more tightly bound) ligand to  $\text{Mn}^{\text{IV}}$  than water in the  $S_3$  and presumably the  $S_4$  states, ammonia is unlikely to be released until after the O-O bond formation step, at which point  $\text{Mn}_{\text{A}4}$  returns to its +III oxidation state and is again five-coordinate.

**O5 Represents a Substrate Site.** The slow rate of exchange of  $W_s$  and the observation that the rate is S-state (i.e., Mn oxidation state)

dependent suggest that  $W_s$  represents a Mn–oxygen ligand (16, 18, 20, 35). In Rapatskiy et al. (17), three exchangeable Mn–O ligands were identified, and thus, all three potentially represent  $W_s$ : W1, W2, and a  $\mu$ -oxo bridge, either O4 or O5. As described above, the ammonia effect excludes W1 and demonstrates that O5 (and not O4) represents the exchangeable bridge. Thus, we can now reduce the number of possible candidates for  $W_s$  to only two: W2 and O5.

A series of studies are converging with regard to the role of O5 instead of W2 as the  $W_s$  substrate site. Critical to this assignment has been the recent demonstration that one of the  $\mu$ -oxo bridges (shown here to be O5) exchanges rapidly with bulk water (17), with an exchange rate consistent with mass spectrometry measurements (16, 18–20) and over 1,000 times faster than that seen in synthetic model systems (40). A rationale for this enhanced exchange rate was recently provided by the theoretical study of Pantazis et al. (13), where it was shown that O5 has a flexible coordination, acting as either a  $\mu$ -oxo linkage to the outer Mn ( $Mn_{A4}$ ) or a vertex of the cuboidal unit proper. Similarly, the OEC appears to contain several pathways for internal oxygen exchange between terminal water ligands to Ca or Mn, which may allow a calcium-ligated bridge such as O5 to exchange rapidly (41).

Site-selective perturbations such as protein mutagenesis provide further support for the assignment of O5 over W2 as  $W_s$ . The replacement of Ca with Sr strongly enhances the exchange rate of  $W_s$  (36). As O5 (not W2 or O4) is a ligand to Ca/Sr (1), this result is readily understood (36, 41). Similarly, the mutation of the D1-Glu189 (bridge between  $Mn_{D1}$  and Ca), the D1-Asp170 (bridge between  $Mn_{A4}$  and Ca), and the CP43-Glu354 (bridge between  $Mn_{B3}$  and  $Mn_{C2}$ ) all enhance the rate of  $W_s$  exchange (20, 42, 43). As O5 is a ligand to  $Mn_{A4}$ ,  $Mn_{B3}$ , and  $Mn_{D1}$  (owing to its two isoenergetic forms in the  $S_2$  state and potentially the  $S_3$  state) (1, 13), the observed perturbation in the exchange rate seen in these mutants is again readily explained.

**An O–O Bond Formation Mechanism Involving O5.** The O–O bond reaction can proceed via either (i) a nucleophilic attack of O5 by a nearby substrate, i.e., between the  $\mu$ -oxo bridge (O5) and a terminal hydroxide/Ca<sup>2+</sup>-bound water (W3), or (ii) an oxo/oxyl radical coupling of O5 and an as yet unidentified water (possibly previously bound to Ca/ $Mn_{A4}$ ) that is located proximal to O5 in the  $S_3/S_4$  states, as proposed by Siegbahn (12) (see also refs. 41, 44).

Of the two pathways to O–O bond formation, only the nucleophilic attack mechanism has been previously observed in Mn model systems, albeit with a much slower rate than seen for the OEC (45, 46). In contrast, the radical coupling mechanism has no precedence in Mn model chemistry, but has been demonstrated as an efficient O–O bond formation pathway in second-row transition metal catalysts; see, for example, the ruthenium (Ru–Hbpp) dimer complex (47). This latter mechanistic route has been demonstrated in silico by Siegbahn as the most efficient O–O bond formation pathway (12).

A unique feature of the oxo/oxyl mechanism proposed by Siegbahn is that the second, fast-exchanging water substrate ( $W_f$ ) binds to the OEC late in the S-state cycle, a conclusion supported by FTIR difference spectroscopy (48). This additional substrate from the bulk binds to the open coordination site of  $Mn_{D1}$  as a water/hydroxide ion in the  $S_3$  state, forming an oxyl radical in the  $S_4$  state (Fig. 4) (12). Superficially, this appears to be in disagreement with TR-MIMS measurements, which suggest that  $W_f$  has a similar affinity in the  $S_2$  state to that in the  $S_3$  state, requiring it to be in a chemically similar environment in both states. The inherent structural flexibility of the OEC provides a rationale for this problem, suggesting a second binding sequence for  $W_f$ , reconciling the oxo/oxyl mechanism with the observation that  $W_f$  is already bound in the  $S_2$  state. Instead, of binding directly to  $Mn_{D1}$ , the second substrate could bind to the solvent-accessible outer  $Mn_{A4}$  ion, as the open coordination site of the complex can exist at either  $Mn_{A4}$  or  $Mn_{D1}$  via the facile movement of the O5/ $W_s$  bridge. In this instance, the terminal hydroxide ligands of  $Mn_{A4}$  in the  $S_3$  state (W2 and  $W_f$ ) would be indistinguishable, owing to rapid interchange, and could be considered

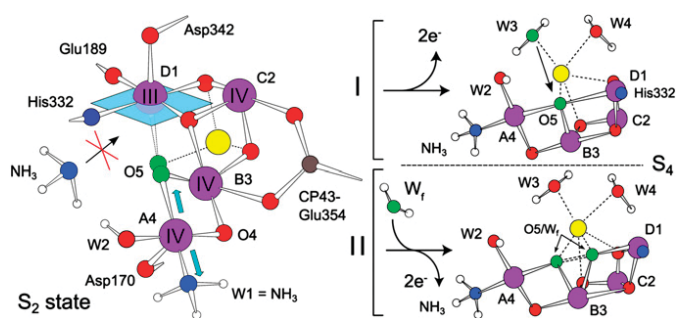


**Fig. 4.** (Left) Site for  $NH_3$  binding to the OEC poised in the  $S_2$  state.  $NH_3$  displaces W1, a water ligand of the outer  $Mn_{A4}$  (a  $Mn^{IV}$  ion in the  $S_2$  state), which slightly affects the binding strength of the oxo-bridge O5, which is *trans* to this position. (Right) O–O bond formation mechanisms consistent with this study (see main text): (I) a nucleophilic attack of O5 by a nearby substrate; (II) an oxo/oxyl radical coupling of O5 and an as yet unidentified additional water marked  $W_f$  (possibly W2). Mn, purple; Ca, yellow; N, blue; O, red; and substrate O, green.

to represent the same species. O5/ $W_s$ , which upon proton movement from  $W_f$  returns to the putative  $S_3$  state proposed by Siegbahn, represents in this tautomeric structure a terminal hydroxide ion bound to a  $Mn^{IV}$  ion. This ligand motif is considered to exchange with bulk solvent on a seconds timescale in Mn model complexes. The  $Mn_{D1}$ -bound oxygen is, however, within a more hydrophobic pocket compared with the  $Mn_{A4}$ -bound oxygen, which explains why two exchange rates are still observed for the two putative  $Mn^{IV}$ -O(H) substrate ligands in the  $S_3$  state. The hydrophobic region about  $Mn_{D1}$  potentially acts to stabilize the subsequent ligand oxidation of the  $Mn_{D1}$ -bound oxygen to an oxyl radical upon advancement to the  $S_4$  state.

Thus, a concerted tetramer mechanism involving O5, which uses the unique geometry of the  $Mn_4O_5Ca$  cluster to bind and position the two substrates, provides a rationale for the substrate exchange phenomenology described in the literature. The sequential uptake of the two substrates ensures that simultaneous binding of both substrates does not occur in the resting states ( $S_0$ ,  $S_1$ ) of the catalyst, which is likely critical for efficient (high turnover frequency) and highly selective  $O_2$  product formation.

## Materials and Methods

<sup>14</sup>N- and <sup>15</sup>N-PSII core complex preparations from *T. elongatus* were isolated as described earlier (49, 50) with modifications described in *SI Materials and Methods*. The  $S_2$  state was generated by short, white-light illumination (5 s) with a tungsten lamp at 185–200 K.

EPR measurements were performed at X-band using Bruker ELEXSYS 500 and 580 spectrometers, at Q-band using a Bruker ELEXSYS E580 spectrometer, and at W-band using a Bruker ELEXSYS E680 spectrometer. X-band CW and pulse EPR measurements were performed at 8.6 K and 4.2 K, respectively. Q- and W-band pulsed EPR measurements were performed at 4.8–5.2 K. Experimental settings were as reported in refs. 11 and 17 and in *Figs. S1–S3*.

TR-MIMS experiments were performed at 20 °C using a modified membrane-inlet cell connected to a magnetic sector field isotope ratio mass spectrometer. Further details regarding experimental procedures and data analysis are described in *SI Materials and Methods* and refs. 16, 19, and 35.

Density functional theory calculations of geometries, exchange coupling constants, vibrational frequencies, and EPR parameters were performed similarly to those described in refs. 10 and 17. Computational details and Cartesian coordinates of the optimized structures are given in *SI Materials and Methods* and *Table S5*, respectively.

**ACKNOWLEDGMENTS.** We thank A. Savitsky (Max-Planck-Institut für Chemische Energiekonversion) and J. Martínez (Consejo Superior de Investigaciones Científicas, Universidad de Zaragoza) for their assistance. This work was supported by The Max-Planck-Gesellschaft, the “Bioénergie” program from the Commissariat à l’Énergie Atomique et aux Énergies Alternatives, the European Union SOLAR-H2 project (FP7 Contract 212508), Vetenskapsrådet, Strong Research Environment Solar Fuels (Umeå University), The Artificial Leaf Project (K&A Wallenberg Foundation), the Swedish Energy Agency, and the Kempe Foundation.

- Umena Y, Kawakami K, Shen J-R, Kamiya N (2011) Crystal structure of oxygen-evolving photosystem II at a resolution of 1.9 Å. *Nature* 473(7345):55–60.
- Ferreira KN, Iverson TM, Maghlaoui K, Barber J, Iwata S (2004) Architecture of the photosynthetic oxygen-evolving center. *Science* 303(5665):1831–1838.
- Loll B, Kern J, Saenger W, Zouni A, Biesiadka J (2005) Towards complete cofactor arrangement in the 3.0 Å resolution structure of photosystem II. *Nature* 438(7070):1040–1044.
- Kok B, Forbush B, McGloin M (1970) Cooperation of charges in photosynthetic O<sub>2</sub> evolution-I. A linear four step mechanism. *Photochem Photobiol* 11(6):457–475.
- Yano J, et al. (2006) Where water is oxidized to dioxygen: Structure of the photosynthetic Mn<sub>4</sub>Ca cluster. *Science* 314(5800):821–825.
- Pushkar YL, Yano J, Sauer K, Boussac A, Yachandra VK (2008) Structural changes in the Mn<sub>4</sub>Ca cluster and the mechanism of photosynthetic water splitting. *Proc Natl Acad Sci USA* 105(6):1879–1884.
- Dau H, Grundmeier A, Loja P, Haumann M (2008) On the structure of the manganese complex of photosystem II: Extended-range EXAFS data and specific atomic-resolution models for four S-states. *Philos Trans R Soc Lond B Biol Sci* 363(1494):1237–1243, discussion 1243–1244.
- Yano J, et al. (2005) X-ray damage to the Mn<sub>4</sub>Ca complex in single crystals of photosystem II: A case study for metalloprotein crystallography. *Proc Natl Acad Sci USA* 102(34):12047–12052.
- Grabolle M, Haumann M, Müller C, Liebisch P, Dau H (2006) Rapid loss of structural motifs in the manganese complex of oxygenic photosynthesis by X-ray irradiation at 10–300 K. *J Biol Chem* 281(8):4580–4588.
- Ames W, et al. (2011) Theoretical evaluation of structural models of the S<sub>2</sub> state in the oxygen evolving complex of Photosystem II: Protonation states and magnetic interactions. *J Am Chem Soc* 133(49):19743–19757.
- Cox N, et al. (2011) Effect of Ca<sup>2+</sup>/Sr<sup>2+</sup> substitution on the electronic structure of the oxygen-evolving complex of photosystem II: A combined multifrequency EPR, <sup>55</sup>Mn-ENDOR, and DFT study of the S<sub>2</sub> state. *J Am Chem Soc* 133(10):3635–3648.
- Siegbahn PEM (2009) Structures and energetics for O<sub>2</sub> formation in photosystem II. *Acc Chem Res* 42(12):1871–1880.
- Pantazis DA, Ames W, Cox N, Lubitz W, Neese F (2012) Two interconvertible structures that explain the spectroscopic properties of the oxygen-evolving complex of photosystem II in the S<sub>2</sub> state. *Angew Chem Int Ed Engl* 51(39):9935–9940.
- Dismukes GC, Siderer Y (1981) Intermediates of a polynuclear manganese center involved in photosynthetic oxidation of water. *Proc Natl Acad Sci USA* 78(1):274–278.
- Schweiger A, Jeschke G (2001) *Principles of Pulse Electron Paramagnetic Resonance* (Oxford Univ Press, Oxford).
- Messinger J, Badger M, Wydrzynski T (1995) Detection of one slowly exchanging substrate water molecule in the S<sub>3</sub> state of photosystem II. *Proc Natl Acad Sci USA* 92(8):3209–3213.
- Rapatskiy L, et al. (2012) Detection of the water binding sites of the oxygen-evolving complex of photosystem II using W-band <sup>17</sup>O ELDOR-detected NMR spectroscopy. *J Am Chem Soc* 134(40):16619–16634.
- Hillier W, Wydrzynski T (2000) The affinities for the two substrate water binding sites in the O<sub>2</sub> evolving complex of photosystem II vary independently during S-state turnover. *Biochemistry* 39(15):4399–4405.
- Hillier W, Wydrzynski T (2004) Substrate water interactions within the Photosystem II oxygen evolving complex. *Phys Chem Chem Phys* 6(20):4882–4889.
- Cox N, Messinger J (2013) Reflections on substrate water and dioxygen formation. *Biochim Biophys Acta* 1827(8–9):1020–1030.
- Sandusky PO, Yocum CF (1984) The chloride requirement for photosynthetic oxygen evolution. Analysis of the effects of chloride and other anions on amine inhibition of the oxygen-evolving complex. *Biochim Biophys Acta* 766(3):603–611.
- Sandusky PO, Yocum CF (1986) The chloride requirement for photosynthetic oxygen evolution: Factors affecting nucleophilic displacement of chloride from the oxygen-evolving complex. *Biochim Biophys Acta* 849(1):85–93.
- Beck WF, Brudvig GW (1986) Binding of amines to the O<sub>2</sub>-evolving center of photosystem II. *Biochemistry* 25(21):6479–6486.
- Beck WF, de Paula JC, Brudvig GW (1986) Ammonia binds to the manganese site of the oxygen-evolving complex of photosystem II in the S<sub>2</sub> state. *J Am Chem Soc* 108(14):4018–4022.
- Britt RD, Zimmermann JL, Sauer K, Klein MP (1989) Ammonia binds to the catalytic manganese of the oxygen-evolving complex of photosystem II. Evidence by electron spin-echo envelope modulation spectroscopy. *J Am Chem Soc* 111(10):3522–3532.
- Boussac A, Rutherford AW, Styring S (1990) Interaction of ammonia with the water splitting enzyme of photosystem II. *Biochemistry* 29(1):24–32.
- Chu H-A, Sackett H, Babcock GT (2000) Identification of a Mn-O-Mn cluster vibrational mode of the oxygen-evolving complex in photosystem II by low-frequency FTIR spectroscopy. *Biochemistry* 39(47):14371–14376.
- Hou L-H, Wu C-M, Huang H-H, Chu H-A (2011) Effects of ammonia on the structure of the oxygen-evolving complex in photosystem II as revealed by light-induced FTIR difference spectroscopy. *Biochemistry* 50(43):9248–9254.
- Boussac A, Sugiura M, Inoue Y, Rutherford AW (2000) EPR study of the oxygen evolving complex in His-tagged photosystem II from the cyanobacterium *Synechococcus elongatus*. *Biochemistry* 39(45):13788–13799.
- Stich TA, Whittaker JW, Britt RD (2010) Multifrequency EPR studies of manganese catalases provide a complete description of proteinaceous nitrogen coordination. *J Phys Chem B* 114(45):14178–14188.
- Stich TA, Yeagle GJ, Service RJ, Debus RJ, Britt RD (2011) Ligation of D1-His332 and D1-Asp170 to the manganese cluster of photosystem II from *Synechocystis* assessed by multifrequency pulse EPR spectroscopy. *Biochemistry* 50(34):7390–7404.
- Schosseler P, Wacker T, Schweiger A (1994) Pulsed ELDOR detected NMR. *Chem Phys Lett* 224(3–4):319–324.
- Sinnecker S, Neese F, Noodleman L, Lubitz W (2004) Calculating the electron paramagnetic resonance parameters of exchange coupled transition metal complexes using broken symmetry density functional theory: Application to a Mn<sup>III</sup>/Mn<sup>IV</sup> model compound. *J Am Chem Soc* 126(8):2613–2622.
- Pantazis DA, et al. (2009) Structure of the oxygen-evolving complex of photosystem II: Information on the S<sub>2</sub> state through quantum chemical calculation of its magnetic properties. *Phys Chem Chem Phys* 11(31):6788–6798.
- Hillier W, Messinger J, Wydrzynski T (1998) Kinetic determination of the fast exchanging substrate water molecule in the S<sub>3</sub> state of photosystem II. *Biochemistry* 37(48):16908–16914.
- Hendry G, Wydrzynski T (2003) <sup>18</sup>O isotope exchange measurements reveal that calcium is involved in the binding of one substrate-water molecule to the oxygen-evolving complex in photosystem II. *Biochemistry* 42(20):6209–6217.
- Kusunoki M (2007) Mono-manganese mechanism of the photosystem II water splitting reaction by a unique Mn<sub>4</sub>Ca cluster. *Biochim Biophys Acta* 1767(6):484–492.
- Kusunoki M (2011) S<sub>1</sub>-state Mn<sub>4</sub>Ca complex of Photosystem II exists in equilibrium between the two most-stable isomeric substates: XRD and EXAFS evidence. *J Photochem Photobiol B* 104(1–2):100–110.
- Yamaguchi K, et al. (2012) The nature of chemical bonds of the CaMn<sub>4</sub>O<sub>5</sub> cluster in oxygen evolving complex of photosystem II: Jahn-Teller distortion and its suppression by Ca doping in cubane structures. *Int J Quantum Chem* 113(4):453–473.
- Tagore R, Chen H, Crabtree RH, Brudvig GW (2006) Determination of μ-oxo exchange rates in di-μ-oxo dimanganese complexes by electrospray ionization mass spectrometry. *J Am Chem Soc* 128(29):9457–9465.
- Messinger J (2004) Evaluation of different mechanistic proposals for water oxidation in photosynthesis on the basis of Mn<sub>4</sub>O<sub>5</sub>Ca structures for the catalytic site and spectroscopic data. *Phys Chem Chem Phys* 6(20):4764–4771.
- Hillier W, et al. (2008) *Photosynthesis. Energy from the Sun. 14th International Congress on Photosynthesis, vol. 1*, eds Allen JF, Gantt E, Golbeck J, Osmond B (Springer, Dordrecht), pp 427–430.
- Service RJ, et al. (2011) Participation of glutamate-354 of the CP43 polypeptide in the ligation of manganese and the binding of substrate water in photosystem II. *Biochemistry* 50(1):63–81.
- Yamanaka S, et al. (2011) Possible mechanisms for the O-O bond formation in oxygen evolution reaction at the CaMn<sub>4</sub>O<sub>5</sub>(H<sub>2</sub>O)<sub>4</sub> cluster of PSII refined to 1.9 Å X-ray resolution. *Chem Phys Lett* 511(1–3):138–145.
- Gao Y, Åkermark T, Liu J, Sun L, Åkermark B (2009) Nucleophilic attack of hydroxide on a Mn<sup>V</sup> oxo complex: A model of the O-O bond formation in the oxygen evolving complex of photosystem II. *J Am Chem Soc* 131(25):8726–8727.
- Privalov T, et al. (2007) A computational study of O-O bond formation catalyzed by mono- and bis-Mn<sup>IV</sup>-corrole complexes. *Inorg Chem* 46(17):7075–7086.
- Romain S, Bozoglian F, Sala X, Llobet A (2009) Oxygen-oxygen bond formation by the Ru-Hbpp water oxidation catalyst occurs solely via an intramolecular reaction pathway. *J Am Chem Soc* 131(8):2768–2769.
- Noguchi T (2008) FTIR detection of water reactions in the oxygen-evolving centre of photosystem II. *Philos Trans R Soc Lond B Biol Sci* 363(1494):1189–1194, discussion 1194–1195.
- Boussac A, et al. (2004) Biosynthetic Ca<sup>2+</sup>/Sr<sup>2+</sup> exchange in the photosystem II oxygen-evolving enzyme of *Thermosynechococcus elongatus*. *J Biol Chem* 279(22):22809–22819.
- Sander J, et al. (2010) Functional characterization and quantification of the alternative PsbA copies in *Thermosynechococcus elongatus* and their role in photoprotection. *J Biol Chem* 285(39):29851–29856.

# Supporting Information

Pérez Navarro et al. 10.1073/pnas.1304334110

## SI Materials and Methods

Photosystem II (PSII) core complex preparations from wild-type *Thermosynechococcus elongatus* (1) were isolated as described earlier (2–4). X-band samples were prepared with the following modifications. After the loading of the Ni column with the solubilized membranes, the resin was washed with buffer 2 [1 M betaine, 10% (wt/vol) glycerol, 40 mM Mes, 15 mM MgCl<sub>2</sub>, 15 mM CaCl<sub>2</sub>, 100 mM NaCl, 1 mM L-histidine, 0.03% (wt/vol) β-DM, pH 6.5] until the optical density of the eluate at 665 nm decreased below 0.05 (~15 h). Then, PSII core complexes were eluted with buffer 3 [1 M betaine, 40 mM Mes, 15 mM MgCl<sub>2</sub>, 15 mM CaCl<sub>2</sub>, 200 mM NaCl, 180 mM L-histidine, 0.06% (wt/vol) β-DM, pH 6.5]. The eluate was then concentrated and washed in buffer 4 (1 M betaine, 15 mM MgCl<sub>2</sub>, and 15 mM CaCl<sub>2</sub>) by using centrifugal filter devices (Ultrafree-15; Millipore) until the Mes concentration was estimated to be lower than 0.5 mM. <sup>15</sup>N-labeled PSII samples were prepared from cells grown in a medium with <sup>15</sup>NH<sub>4</sub>Cl and <sup>15</sup>NO<sub>3</sub><sup>-</sup> salts. PSII core complexes were finally resuspended in buffer 4 (+ 40 mM Mes) at a Chl concentration of ~2–3 mg Chl·ml<sup>-1</sup> and stored in liquid N<sub>2</sub> until use. PSII material for Q/W-band measurements was instead stored at -80 °C until use. The S<sub>2</sub> state was generated by short (5 s) white-light illumination with a tungsten lamp at 200 K, using an ethanol bath cooled down with dry ice. Resuspension of the PSII samples in labeled H<sub>2</sub><sup>17</sup>O (90%) buffer was achieved as reported in ref. 5. Ammonia was added at a ratio of 1:10 vol/vol to the samples from a stock solution of 1 M ammonium chloride (<sup>14</sup>NH<sub>4</sub>Cl) in 1 M Hepes (pH 7.6) buffer, yielding a free-base NH<sub>3</sub> concentration of 2 mM. PSII samples were reconcentrated using Millipore microcentrifuge filters to the desired concentration. Samples were then placed in Q/W-band tubes and left in complete darkness for ~10 min. To observe a minimally perturbed S<sub>2</sub> multiline signal, the sample was illuminated at 185 K (ethanol/liquid N<sub>2</sub> bath). To observe the ammonia-modified multiline, the sample was first illuminated at 200 K and then subsequently annealed at ~260 K (ethanol + CO<sub>2</sub>/dry ice bath) for 30 s before freezing to 80 K. X-band samples were given two saturating YAG (532 nm) light flashes and 1 h dark adaptation before the addition of <sup>14</sup>NH<sub>4</sub>Cl solution to maximize S<sub>2</sub> state yields.

Time-resolved membrane inlet mass spectrometry (TR-MIMS) experiments were performed in a stirred, temperature-controlled (20 °C) membrane-inlet cell (165 μL volume) connected to a magnetic sector field isotope ratio mass spectrometer (ThermoFinnigan Delta<sup>PLUS</sup> XP) via a cooling trap (liquid N<sub>2</sub>). Samples were loaded in darkness. After 20 min of degassing, the sample was advanced to the S<sub>2</sub> state with one saturating Xe-lamp flash. Subsequently the sample was rapidly diluted with H<sub>2</sub><sup>18</sup>O (97%, 8 ms mixing time) and two further flashes were applied (interflash separation 10 ms), generating O<sub>2</sub>. The delay between the dilution and the double flash was incremented between 8 ms and 10 s. The final <sup>18</sup>O sample enrichment was 22%. Molecular oxygen dissolved in the H<sub>2</sub><sup>18</sup>O was removed from the delivery syringe (modified Hamilton CR-700-50) by glucose/glucose oxidase and catalase (6). After 5 min, four additional flashes were given at 2 Hz and used for normalization. Data analysis was performed as described earlier (6–8).

Density functional theory calculations used an initial model geometry taken from Ames et al. (9) (model 1d2' of that study), and were performed with the quantum chemical program system "ORCA" (28). This structure was reoptimized for the ammonia-modified S<sub>2</sub> state, after replacement of W1 with NH<sub>3</sub> (1d2'-NH<sub>3</sub>) (Table S5). Geometry optimizations used the BP86 functional (10, 11) along with the 2010 dispersion corrections of Grimme

(12) and the zero-order regular approximation (ZORA) to account for scalar relativistic effects (13–15). All atoms except carbon and hydrogen, for which the split-valence polarized SVP basis set was used, were described with the relativistically contracted def2-TZVP(-f) basis sets (16). Decontracted def2-TZVP/J basis sets (17) were used for the resolution of the identity approximation to Coulomb exchange (RI-J). Tight self-consistent field (SCF) convergence and regular integration grids (Grid4 in ORCA convention) were applied. Optimizations were performed with the conductor-like screening model (COSMO) (18) with a dielectric constant of 8.0. Harmonic vibrational frequencies were computed for the optimized geometries, using numerical two-side differentiation with an increment of 0.01 Bohr. Both structures, with and without NH<sub>3</sub>, were confirmed as genuine minima by the absence of imaginary frequencies (negative Hessian eigenvalues).

Exchange coupling constants were computed by the broken symmetry (BS)-DFT approach, using the TPSSh functional (19) with the RI-J approximation to the Coulomb exchange and the chain-of-spheres approximation to exact exchange (20). Scalar relativistic effects were included with ZORA paired with the segmented all-electron relativistically contracted (SARC) def2-TZVP(-f) basis sets and the decontracted def2-TZVP/J Coulomb fitting basis sets for all atoms. Increased integration grids (Grid5 and GridX5) were used in the calculation of all magnetic parameters. For the calculation of the hyperfine tensors, specially constructed basis sets based on SARC def2-TZVP but with added flexibility in the core region were used for the N and O atoms. These basis sets are described in ref. 21. The radial integration grids were increased to an integration accuracy of 9 (in ORCA convention) for <sup>14</sup>N and <sup>17</sup>O. Picture change effects were included in the calculation of EPR parameters. Details regarding the application of the BS-DFT approach for the calculation of EPR parameters in manganese systems can be found in recent work (9, 22–27).

## SI EPR Theory/Simulations

**EPR and <sup>55</sup>Mn-Electron Nuclear Double Resonance Data and Spin Hamiltonian Simulations.** Spectra were simultaneously fitted assuming an effective spin  $S = 1/2$  ground state (for details, see refs. 26, 29). The basis set that describes the Mn-tetramer spin manifold can be built from the product of the eigenstates of the interacting spins:

$$|\frac{1}{2} MI_1 I_2 I_3 I_4 m_1 m_2 m_3 m_4 \rangle. \quad [\text{S1}]$$

Here,  $M_i$  refers to the electronic magnetic sublevel,  $\pm 1/2$ ;  $I_i$  takes the value  $5/2$  for each <sup>55</sup>Mn; and each  $m_i$  takes the values  $-I_i, 1 - I_i, \dots, I_i - 1, I_i$ .

The spin Hamiltonian that describes the spin manifold is

$$\hat{H} = \beta_e \vec{B}_0 \cdot \hat{G} \cdot \vec{S} + \sum_i \left( g_n \beta_n \vec{B}_0 \cdot \vec{I}_i + \vec{S} \cdot \hat{A}_i \cdot \vec{I}_i \right). \quad [\text{S2}]$$

It contains (i) the electronic Zeeman term for the total electronic spin, (ii) nuclear Zeeman terms for the <sup>55</sup>Mn nuclei, and (iii) hyperfine terms for the <sup>55</sup>Mn nuclei. This Hamiltonian was used to simulate all spectra. The electron Zeeman term was treated exactly. The nuclear Zeeman and hyperfine terms were treated using second-order perturbation theory. The nuclear quadrupole coupling was not explicitly considered. Spectral simulations were performed numerically, using the EasySpin package (30) in MATLAB.

Historically, ammonia binding was thought to significantly alter the electronic structure of the oxygen-evolving complex (OEC), as proposed by Peloquin et al. (29). There, it was suggested that NH<sub>3</sub> binding led to an interchange of the valence states of the Mn cluster such that the only Mn in the +III oxidation state was located at a different Mn site (29). This proposal now seems unlikely. As shown in the main text, the Mn<sub>D1</sub>-His332 signal, which can be considered a spin probe of the electronic structure of the OEC, does not significantly change upon NH<sub>3</sub> binding, requiring that the oxidation state of Mn<sub>D1</sub>, the most likely candidate for the Mn<sup>III</sup>, does not change (9, 26, 27, 31, 32). The effect of NH<sub>3</sub> binding is probably more similar to that seen upon the replacement of the Ca<sup>2+</sup> ion with Sr<sup>2+</sup>. Sr<sup>2+</sup> has only a subtle effect on the electronic structure of the OEC, perturbing the Mn<sub>D1</sub><sup>III</sup> ion, which leads to changes in the hyperfine tensor anisotropy of all four Mn nuclei and thus a modified S<sub>2</sub> multiline EPR spectrum (26). Simulations of the EPR and <sup>55</sup>Mn-electron nuclear double resonance (ENDOR) data are shown in Fig. S1 and support this basic model. The fitted *g* and hyperfine tensors reported in Table S1 are approximately the same in terms of both magnitude and symmetry in both the control and the NH<sub>3</sub> sample, confirming that the oxidation state pattern for the OEC does not change upon ammonia binding, consistent with the <sup>14</sup>N-electron spin echo envelope modulation (ESEEM) Mn<sub>D1</sub>-His332 data shown in Fig. 2 C and D in the main text.

**<sup>14</sup>N-ESEEM/<sup>17</sup>O-Electron–Electron Double-Resonance–Detected NMR Data and Spin Hamiltonian Simulations.** Spectra were simultaneously fitted assuming an effective spin *S* = 1/2 ground state (for details, see ref. 5). The basis set that describes the ligand-Mn-tetramer spin manifold (excluding <sup>55</sup>Mn nuclei) can be built from the product of the eigenstates of the interacting spins:

$$\left| \frac{1}{2} \ M \ I \ m \right\rangle. \quad [\text{S3}]$$

Here *M* refers to the electronic magnetic sublevels ±1/2; *I* takes the value 1 for <sup>14</sup>N and 5/2 for <sup>17</sup>O; and *m<sub>i</sub>* takes the values −*I<sub>i</sub>*, 1 − *I<sub>i</sub>*, ..., *I<sub>i</sub>* − 1, *I<sub>i</sub>*.

The spin Hamiltonian that describes the single nucleus–electron spin manifold is

$$\hat{H} = \beta_e \vec{B}_0 \cdot \hat{G} \cdot \vec{S} + g_o \beta_n \vec{B} \cdot \vec{I} + \vec{S} \cdot \hat{A} \cdot \vec{I}. \quad [\text{S4}]$$

It contains (i) the electronic Zeeman term for the total electronic spin, (ii) the nuclear Zeeman term for the <sup>14</sup>N/<sup>17</sup>O nucleus, and (iii) the hyperfine term for the <sup>14</sup>N/<sup>17</sup>O nucleus. This Hamiltonian was used to simulate all <sup>14</sup>N-ESEEM spectra and <sup>17</sup>O-electron–electron double-resonance–detected NMR (EDNMR) data.

X-band three-pulse ESEEM measurements were performed on both <sup>14</sup>N-PSII and <sup>15</sup>N-PSII treated with ammonia (<sup>14</sup>NH<sub>3</sub>). As PSII contains additional cofactors such as cyt<sub>b559</sub> and cyt<sub>c550</sub>, which also exhibit nitrogen couplings, annealed-minus-dark difference spectra are reported. The annealed S<sub>2</sub> spectrum is generated by low-temperature illumination (185–200 K) and subsequent annealing to allow the ammonia to bind (260 K), whereas the dark S<sub>1</sub> spectrum represents the initial state. Nitrogen signals attributable to the OEC are seen only in the S<sub>2</sub> state whereas the cyt<sub>b559</sub> and cyt<sub>c550</sub> nitrogen signals should be unchanged in both S<sub>1</sub> and S<sub>2</sub>. The annealed-minus-dark subtraction introduced no artifacts as evidenced by the comparison of the <sup>14</sup>N-PSII and universally labeled <sup>15</sup>N-PSII data, which are essentially identical. The annealed-minus-dark difference spectrum is assigned to a single <sup>14</sup>N of the Mn<sub>4</sub>O<sub>5</sub>Ca cluster-bound ammonia. This species displays three sharp nuclear-quadrupole lines at ~0.5, 1.0, and 1.5 MHz in the Fourier-transformed spectra. Spin Hamiltonian simulations of the ESEEM spectra, measured at a series of τ-values, are shown in Fig. S2, *Left* and all fitted parameters are given in Table S2 along with

DFT estimates for the hyperfine and quadrupole couplings. Our DFT calculations nominally reproduce the small experimental isotropic hyperfine coupling and the magnitude of the quadrupole coupling/electric field gradient. A multipole estimate was used to estimate the through-space interaction (*A*<sub>dip</sub>), which suggests *A*<sub>dip</sub> should be approximately axially symmetric, as observed experimentally. This simple calculation does, however, overestimate *A*<sub>dip</sub> by a factor of 2.

The fitted spin Hamiltonian parameters of the <sup>14</sup>NH<sub>3</sub> coupling reported in Table S2 are similar to those reported in the earlier higher-plant study (33). As seen in this earlier study, the quadrupole coupling shows significant asymmetry (*η* ≈ 0.5). The recent crystal structure provides a rationale for this anomalous result, assuming NH<sub>3</sub> displaces the W1 ligand. W1 is in H-bonding distance to the D1-Asp61 and the Asp61/W1 couple has been proposed as important for proton movement from the OEC (34–36). Thus, an NH<sub>3</sub> ligand in the site of W1 is likely to have an electrostatic environment that is distorted away from axial symmetry. The role of such counter ions has recently been shown to be important for the calculation of quadrupole couplings of Mn complexes (21). As Asp61 is not included in our DFT models, this asymmetry is not reproduced in our calculations, although the magnitude of the quadrupole coupling is reproduced.

As a final proof that this signal represents a <sup>14</sup>NH<sub>3</sub> ligand to the OEC, <sup>15</sup>NH<sub>3</sub> instead of <sup>14</sup>NH<sub>3</sub> was added to <sup>14</sup>N-PSII. In annealed-minus-dark difference spectra, the modulation described above was lost, replaced with transitions that now appear near 0 MHz in the Fourier-transformed spectra, consistent with a <sup>15</sup>N ligand interaction.

Spin Hamiltonian simulations were also performed for the <sup>14</sup>N-His332 signal seen using Q-band ESEEM, shown in Fig. S2, *Right*. A complete parameter list is given in Table S2 and compared with earlier literature data along with DFT estimates for the hyperfine and quadrupole couplings. As with the NH<sub>3</sub> ligand, our DFT calculations nominally reproduce the experimental isotropic hyperfine coupling and quadrupole coupling, and the DFT values are not significantly changed by the replacement of W1 with NH<sub>3</sub>. It is noted that the fitted parameters are slightly different from those of our previous report using W-band EDNMR (5) but are similar to those of earlier ESEEM studies of Yeagle et al. (37) and Stich et al. (38), measured using PSII purified from spinach and *Synechocystis* (6803), respectively. This is currently under investigation and may reflect partial breakdown of the *S* = 1/2 ground-state approximation at W-band. In addition, current simulations do not very well reproduce ESEEM data traces collected using longer τ-values (>300 ns) compared to those with shorter τ-values (<300 ns). This is also being further investigated.

**<sup>1</sup>H-ENDOR.** Protons in the vicinity of the OEC can be readily measured using Q-band <sup>1</sup>H-ENDOR (5). The magnitude of a proton coupling within a metallocofactor is usually derived from a simple dipolar (through-space) interaction between the electron spin and the nearby proton spin and thus allows the distance of the proton to the metal center(s) to be obtained. The width of the <sup>1</sup>H-ENDOR signal envelope (of ≈9 MHz) for the OEC in the S<sub>2</sub> state has previously been assigned to the terminal water/OH-ligands (W1/W2) of Mn<sub>A4</sub>, i.e., <sup>1</sup>H protons ~2.4–3 Å away from one of the Mn ions of the OEC that carries a spin projection of ~1 (5, 39–41). In addition, the width of the envelope has been suggested to exclude a protonated oxygen bridge (μ-hydroxo).

The <sup>1</sup>H-ENDOR envelopes for <sup>14</sup>N-PSII with and without ammonia (<sup>14</sup>NH<sub>3</sub>) are shown in Fig. S34. The two are very similar, suggesting that the nearest approach of a <sup>1</sup>H nucleus to the Mn ions is essentially the same for the OEC with and without an NH<sub>3</sub> ligand. In our DFT models, the protons of both the NH<sub>3</sub> and the W1/W2 ligands are between 2.4 and 2.7 Å away from Mn<sub>A4</sub>. As such, the <sup>1</sup>H-ENDOR envelope is expected to not change considerably upon addition of ammonia, as observed

experimentally. Importantly, the absence of a large proton coupling suggests ammonia does not replace one of the oxygen bridges ( $\mu$ -oxo) of the OEC, forming an amido ( $-\text{NH}_2$ ) bridge as previously suggested in ref. 33.

**<sup>17</sup>O-Mims ENDOR.** Water molecules that are not directly coordinated to the Mn ions are not well visualized by using W-band EDNMR, and they provide only a small contribution to the signal envelope (5). These species, i.e., the waters bound to the  $\text{Ca}^{2+}$  ion, W3 and W4, can instead be measured using W-band Mims ENDOR (5). Fig. S3B shows the <sup>17</sup>O-Mims ENDOR spectra of W3/W4 in PSII samples with and without added ammonia. In both samples, a similar signal envelope is observed centered at the Larmor frequency of <sup>17</sup>O [ $\nu_{\text{N}}(^{17}\text{O}) \approx 19.6$  MHz], suggesting ammonia does not displace W3 or W4. The signal has a width of <1 MHz (FWHM) and a near-Lorentzian lineshape, with a resolved splitting of 0.5 MHz.

**<sup>17</sup>O-EDNMR Simulations/Power Dependence.** Spin Hamiltonian simulations of the EDNMR signals in Fig. 3 (<sup>14</sup>N-PSII) and Fig. S4 (<sup>15</sup>N-PSII) were performed as described in ref. 5. All parameters are given in Table S3. The anisotropic (dipolar,  $A_{\text{dip}}$ ) component for each of the three <sup>17</sup>O hyperfine tensors (large, intermediate, and matrix) was kept fixed to that reported in ref. 5 in both the native and the ammonia-treated samples along with all linewidths. It is noted that the fitted linewidths presumably represent the unresolved quadrupole splittings. In addition, the unresolved quadrupole is expected to lead to the nonequal peak intensities for the double-quantum peaks of each <sup>17</sup>O doublet. As such, the relative intensities of each doublet peak are allowed to vary by 50%.

As the <sup>17</sup>O double-quantum region for the ammonia-treated sample was symmetric about twice the <sup>17</sup>O Larmor frequency,

only two hyperfine couplings (large and intermediate) needed to be included to reproduce the double-quantum spectral profile.

In the <sup>17</sup>O-EDNMR experiments described here, the line intensities of the three different <sup>17</sup>O species predominately depend on the magnitude of the anisotropic (dipolar) coupling  $A_{\text{dip}}$  (5, 42) and the amplitude of the pump pulse [high turning angle (HTA) pulse]. As such, the relative line intensity attributable to different <sup>17</sup>O species will change as the amplitude of the HTA pulse is varied. In Rapatskiy et al. (5), the amplitude of the HTA pulse was set such that the signal from the largest coupled species was maximal. Increasing the amplitude of the HTA pulse begins to suppress the largest coupled species relative to more weakly coupled species; it effectively enhances the contribution of the more weakly coupled components. Thus, by monitoring the power dependence (the magnitude of the EDNMR signal as a function of the HTA pulse amplitude) at different positions within the signal envelope, more information on the contribution of each species can be obtained. In a simple sense, the power dependence represents another way to discern the number of species that make up the signal envelope. Unfortunately, the power dependence cannot yet be simulated, and thus, the contribution of each <sup>17</sup>O component is simply fitted (5).

The power dependence of the <sup>17</sup>O-EDNMR envelope is shown in Fig. S4 C and D. In the control sample, the power dependence of the satellite lines (strongly coupled species) about the <sup>17</sup>O Larmor frequency was significantly different from that of the central line (weakly coupled, matrix species) at the <sup>17</sup>O Larmor frequency. This is in contrast to the ammonia-treated sample. Here the power dependences of the satellites and the central line are more similar, suggesting the range of couplings that make up the envelope has decreased. That is to say, the <sup>17</sup>O profile in the ammonia-treated sample contains a smaller contribution from a third matrix component, i.e., W1.

1. Sugiura M, Boussac A, Noguchi T, Rappaport F (2008) Influence of histidine-198 of the D1 subunit on the properties of the primary electron donor, P680, of photosystem II in *Thermosynechococcus elongatus*. *Biochim Biophys Acta* 1777(4):331–342.
2. Boussac A, et al. (2004) Biosynthetic  $\text{Ca}^{2+}/\text{Sr}^{2+}$  exchange in the photosystem II oxygen-evolving enzyme of *Thermosynechococcus elongatus*. *J Biol Chem* 279(22):22809–22819.
3. Sander J, et al. (2010) Functional characterization and quantification of the alternative PsbA copies in *Thermosynechococcus elongatus* and their role in photoprotection. *J Biol Chem* 285(39):29851–29856.
4. Nowaczyk MM, et al. (2012) Deletion of *psbJ* leads to accumulation of Psb27-Psb28 photosystem II complexes in *Thermosynechococcus elongatus*. *Biochim Biophys Acta* 1817(8):1339–1345.
5. Rapatskiy L, et al. (2012) Detection of the water binding sites of the oxygen-evolving complex of Photosystem II using W-band <sup>17</sup>O ELDOR-detected NMR spectroscopy. *J Am Chem Soc* 134(40):16619–16634.
6. Messinger J, Badger M, Wydrzynski T (1995) Detection of one slowly exchanging substrate water molecule in the  $S_3$  state of photosystem II. *Proc Natl Acad Sci USA* 92(8):3209–3213.
7. Hillier W, Messinger J, Wydrzynski T (1998) Kinetic determination of the fast exchanging substrate water molecule in the  $S_3$  state of photosystem II. *Biochemistry* 37(48):16908–16914.
8. Hillier W, Wydrzynski T (2004) Substrate water interactions within the Photosystem II oxygen evolving complex. *Phys Chem Chem Phys* 6(20):4882–4889.
9. Ames W, et al. (2011) Theoretical evaluation of structural models of the  $S_2$  state in the oxygen evolving complex of Photosystem II: Protonation states and magnetic interactions. *J Am Chem Soc* 133(49):19743–19757.
10. Perdew JP (1986) Density-functional approximation for the correlation energy of the inhomogeneous electron gas. *Phys Rev B Condens Matter* 33(12):8822–8824.
11. Becke AD (1988) Density-functional exchange-energy approximation with correct asymptotic behavior. *Phys Rev A* 38(6):3098–3100.
12. Grimme S, Antony J, Ehrlich S, Krieg H (2010) A consistent and accurate ab initio parametrization of density functional dispersion correction (DFT-D) for the 94 elements H-Pu. *J Chem Phys* 132(15):154104–154119.
13. van Lenthe E, Baerends EJ, Snijders JG (1993) Relativistic regular two-component Hamiltonians. *J Chem Phys* 99(6):4597–4610.
14. Van Lenthe E, Baerends EJ, Snijders JG (1994) Relativistic total-energy using regular approximations. *J Chem Phys* 101(11):9783–9792.
15. Van Wüllen C (1998) Molecular density functional calculations in the regular relativistic approximation: Method, application to coinage metal diatomics, hydrides, fluorides and chlorides, and comparison with first-order relativistic calculations. *J Chem Phys* 109:392–399.
16. Pantazis DA, Chen XY, Landis CR, Neese F (2008) All-electron scalar relativistic basis sets for third-row transition metal atoms. *J Chem Theory Comput* 4(6):908–919.
17. Weigend F (2006) Accurate Coulomb-fitting basis sets for H to Rn. *Phys Chem Chem Phys* 8(9):1057–1065.
18. Klamt A, Schüürmann D (1993) COSMO: A new approach to dielectric screening in solvents with explicit expressions for the screening energy and its gradient. *J Chem Soc Perkin Trans 2*:799–805.
19. Staroverov VN, Scuseria GE, Tao J, Perdew JP (2003) Comparative assessment of a new nonempirical density functional: Molecules and hydrogen-bonded complexes. *J Chem Phys* 119:12129–12137.
20. Neese F, Wennmoths F, Hansen A, Becker U (2009) Efficient, approximate and parallel Hartree-Fock and hybrid DFT calculations. A 'chain-of-spheres' algorithm for the Hartree-Fock exchange. *Chem Phys* 356(1–3):98–109.
21. Cox N, et al. (2011) Electronic structure of a weakly antiferromagnetically coupled  $\text{Mn}^{\text{II}}/\text{Mn}^{\text{III}}$  model relevant to manganese proteins: A combined EPR, <sup>55</sup>Mn-ENDOR, and DFT study. *Inorg Chem* 50(17):8238–8251.
22. Pantazis DA, et al. (2009) A new quantum chemical approach to the magnetic properties of oligonuclear transition-metal complexes: Application to a model for the tetranuclear manganese cluster of photosystem II. *Chemistry* 15(20):5108–5123.
23. Orio M, Pantazis DA, Petrenko T, Neese F (2009) Magnetic and spectroscopic properties of mixed valence manganese(III,IV) dimers: A systematic study using broken symmetry density functional theory. *Inorg Chem* 48(15):7251–7260.
24. Neese F, et al. (2010) Dealing with complexity in open-shell transition metal chemistry from a theoretical perspective: Reaction pathways, bonding, spectroscopy, and magnetic properties. *Adv Inorg Chem* 62:301–349.
25. Pantazis DA, Ames W, Cox N, Lubitz W, Neese F (2012) Two interconvertible structures that explain the spectroscopic properties of the oxygen-evolving complex of photosystem II in the  $S_2$  state. *Angew Chem Int Ed Engl* 51(39):9935–9940.
26. Cox N, et al. (2011) Effect of  $\text{Ca}^{2+}/\text{Sr}^{2+}$  substitution on the electronic structure of the oxygen-evolving complex of photosystem II: A combined multifrequency EPR, <sup>55</sup>Mn-ENDOR, and DFT study of the  $S_2$  state. *J Am Chem Soc* 133(10):3635–3648.
27. Pantazis DA, et al. (2009) Structure of the oxygen-evolving complex of photosystem II: Information on the  $S_2$  state through quantum chemical calculation of its magnetic properties. *Phys Chem Chem Phys* 11(31):6788–6798.
28. Neese F (2012) The ORCA program system. *Comput Mol Sci* 2(1):73–78.
29. Peloquin JM, et al. (2000) <sup>55</sup>Mn ENDOR of the  $S_2$ -state multiline EPR signal of photosystem II: Implications on the structure of the tetranuclear Mn cluster. *J Am Chem Soc* 122(44):10926–10942.
30. Stoll S, Schweiger A (2006) EasySpin, a comprehensive software package for spectral simulation and analysis in EPR. *J Magn Reson* 178(1):42–55.

31. Teutloff C, et al. (2009) Electronic structure of the tyrosine D radical and the water-splitting complex from pulsed ENDOR spectroscopy on photosystem II single crystals. *Phys Chem Chem Phys* 11(31):6715–6726.
32. Schinzel S, Schraut J, Arbuznikov AV, Siegbahn PE, Kaupp M (2010) Density functional calculations of  $^{55}\text{Mn}$ ,  $^{14}\text{N}$  and  $^{13}\text{C}$  electron paramagnetic resonance parameters support an energetically feasible model system for the  $S_2$  state of the oxygen-evolving complex of photosystem II. *Chemistry* 16(34):10424–10438.
33. Britt RD, Zimmermann JL, Sauer K, Klein MP (1989) Ammonia binds to the catalytic manganese of the oxygen-evolving complex of photosystem II. Evidence by electron spin-echo envelope modulation spectroscopy. *J Am Chem Soc* 111(10):3522–3532.
34. Dilbeck PL, et al. (2012) The D1-D61N mutation in *Synechocystis* sp. PCC 6803 allows the observation of pH-sensitive intermediates in the formation and release of  $\text{O}_2$  from photosystem II. *Biochemistry* 51(6):1079–1091.
35. Rivalta I, et al. (2011) Structural-functional role of chloride in photosystem II. *Biochemistry* 50(29):6312–6315.
36. Pokhrel R, McConnell IL, Brudvig GW (2011) Chloride regulation of enzyme turnover: Application to the role of chloride in photosystem II. *Biochemistry* 50(14):2725–2734.
37. Yeagle GJ, Gilchrist ML, Jr., Walker LM, Debus RJ, Britt RD (2008) Multifrequency electron spin-echo envelope modulation studies of nitrogen ligation to the manganese cluster of photosystem II. *Philos Trans R Soc Lond B Biol Sci* 363 (1494):1157–1166, discussion 1166.
38. Stich TA, Yeagle GJ, Service RJ, Debus RJ, Britt RD (2011) Ligation of D1-His332 and D1-Asp170 to the manganese cluster of photosystem II from *Synechocystis* assessed by multifrequency pulse EPR spectroscopy. *Biochemistry* 50(34):7390–7404.
39. Kawamori A, Inui T, Ono T, Inoue Y (1989) ENDOR study on the position of hydrogens close to the manganese cluster in  $S_2$  state of photosystem II. *FEBS Lett* 254(1–2):219–224.
40. Aznar CP, Britt RD (2002) Simulations of the  $^1\text{H}$  electron spin echo-electron nuclear double resonance and  $^2\text{H}$  electron spin echo envelope modulation spectra of exchangeable hydrogen nuclei coupled to the  $S_2$ -state photosystem II manganese cluster. *Philos Trans R Soc Lond B Biol Sci* 357(1426):1359–1365, discussion 1365–1367.
41. Britt RD, et al. (2004) Recent pulsed EPR studies of the photosystem II oxygen-evolving complex: Implications as to water oxidation mechanisms. *Biochim Biophys Acta* 1655(1–3):158–171.
42. Schosseler P, Wacker T, Schweiger A (1994) Pulsed ELDOR detected NMR. *Chem Phys Lett* 224(3–4):319–324.

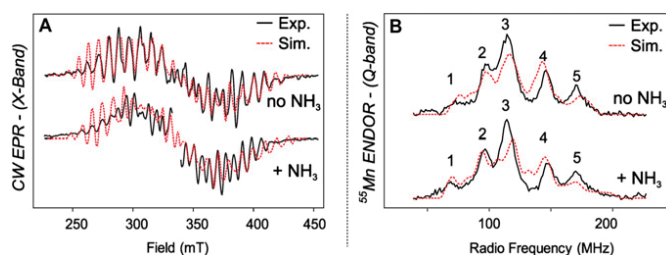


**Fig. S1.** X-band CW-EPR and Q-band pulse-EPR  $^{55}\text{Mn}$ -ENDOR spectra of the control and  $\text{NH}_3$ -containing OEC of PSII derived from *Thermosynechococcus elongatus* poised in the  $S_2$  state (1, 2). (A) X-band CW EPR. The  $S_1$ -state background of cyt b559 and cyt c550 was subtracted from the data after illumination. In native samples, a point mutation was made to replace the tyrosine  $Y_D$  (D2-Tyr160) with a phenylalanine, removing from the spectrum the  $Y_D^*$  signal. In samples, treated with ammonia, the  $Y_D^*$  signal, centered at about  $g \approx 2$ , was removed for clarity of presentation. Experimental parameters: microwave frequencies, 9.4097 GHz (control) and 9.4075 GHz ( $\text{NH}_3$ ); microwave power, 20 mW; modulation amplitude, 25 G; time constant, 80 ms; temperature, 8.6 K. (B) Q-band pulse  $^{55}\text{Mn}$ -Davies ENDOR. The  $S_1$ -state spectrum was subtracted from the  $S_2$ -state data to remove a small  $\text{Mn}^{2+}$  contamination. Experimental parameters: microwave frequencies, 34.0368 GHz (native) and 34.0159 GHz ( $\text{NH}_3$ ); magnetic field, 1,220 mT; shot repetition time, 1 ms; microwave pulse length ( $\pi$ ), 24 ns;  $\tau$ , 268 ns; radio frequency pulse ( $\pi_{RF}$ ), 3.5  $\mu\text{s}$ ; temperature, 5.2 K. The red dotted lines represent a least-squares fitting to the whole dataset, using a model based on the spin Hamiltonian formalism. The optimized parameter sets are given in Table S2.

1. Boussac A, Sugiura M, Inoue Y, Rutherford AW (2000) EPR study of the oxygen evolving complex in His-tagged photosystem II from the cyanobacterium *Synechococcus elongatus*. *Biochemistry* 39(45):13788–13799.
2. Boussac A, Rutherford AW, Styring S (1990) Interaction of ammonia with the water splitting enzyme of photosystem II. *Biochemistry* 29(1):24–32.

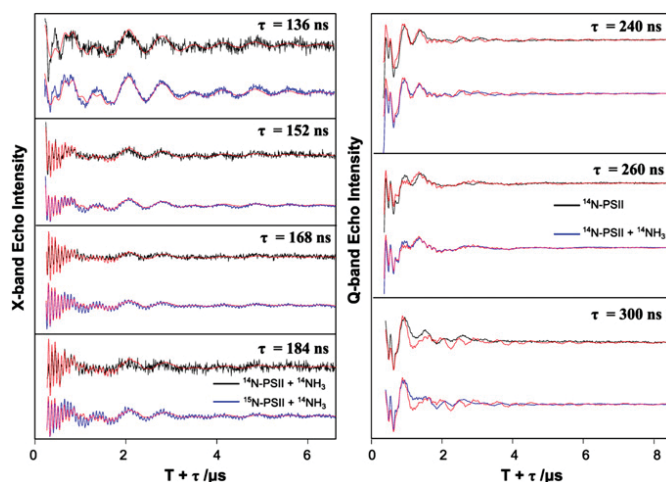


**Fig. S2.** (Left) X-band three-pulse ESEEM annealed-minus-dark difference spectra of ammonia ( $^{14}\text{NH}_3$ )-treated  $^{14}\text{N}$ -PSII and  $^{15}\text{N}$ -PSII (*SI Materials and Methods*). (Right) Q-band three-pulse ESEEM light-minus-dark and annealed-minus-dark difference spectra of control and ammonia ( $^{14}\text{NH}_3$ )-treated  $^{14}\text{N}$ -PSII, respectively. Spectra were collected using the sequence  $t_p - \tau - t_p - T - t_p - \tau - \text{echo}$ , where the length of the  $\pi/2$  microwave pulse was set to  $t_p = 8$  ns (X-band) and  $t_p = 12$  ns (Q-band); the interpulse distance ( $\tau$ ) was set to the values  $\tau = 136, 152, 168,$  and  $184$  ns (X-band) and  $\tau = 240, 260,$  and  $300$  ns (Q-band); and the interpulse distance ( $T$ ) was swept over the range from 64 to 6,464 ns in steps of  $\Delta T = 8$  ns (X-band) and from 100 to 8,176 ns in steps of  $\Delta T = 16$  ns (Q-band). Experimental parameters:  $B_0 = 333$  mT (X-band), 1.22 T (Q-band); temperature, 4.2 K (X-band), 5.2 K (Q-band); shot repetition time of 5 ms (X-band), 1 ms (Q-band). The red dashed lines superimposing the data represent simulations using the spin Hamiltonian formalism (Table S4). The modulation due to protons in the X-band data was simulated using a single, isolated  $^1\text{H}$  species. The decay of the ESEEM traces (data and simulations) was fitted to a third-order polynomial (X-band) and a biexponential decay (Q-band) function. A low-pass filter (3 dB, 10 MHz) was applied to the Q-band ESEEM simulations in an attempt to model the resonator bandwidth.



**Table S1. Principal values of the effective  $G$  and hyperfine tensors ( $A_i$ ) for the EPR and  $^{55}\text{Mn}$ -ENDOR simulations (Fig. S1)**

Sample	$G$	$A_i$ , MHz			
		$A_1$	$A_2$	$A_3$	$A_4$
Control					
x	1.988	321	259	191	161
y	1.978	345	244	219	179
z	1.974	273	272	249	230
iso	1.980	313	258	220	190
aniso	0.009	60	-20	-44	-60
+NH <sub>3</sub>					
x	1.993	314	230	185	167
y	1.974	379	264	215	153
z	1.964	248	279	244	218
iso	1.981	321	246	209	170
aniso	0.019	98	-31	-44	-58

The isotropic  $G$  and  $A_i$  ( $i = 1-4$ ) values are the average of the individual values:  $G_{iso} = (G_x + G_y + G_z)/3$  and  $A_{i,iso} = (A_{i,x} + A_{i,y} + A_{i,z})/3$ . The anisotropy in the  $G$  and  $A_i$  values is expressed as the difference between equatorial (average of  $x$  and  $y$ ) and the axial ( $z$ ) components of the tensor.

**Table S2. Fitted and DFT-calculated spin Hamiltonian parameters for the  $^{14}\text{NH}_3$  ligand and the  $^{14}\text{N}$ -His332 ligand of the OEC: Comparison with literature values**

OEC ligand	Spin Hamiltonian parameters/MHz				
	$ A_{iso} $	$A_{dip}^*$	$ e^2Qq/h $	$\eta$	
$^{14}\text{NH}_3$					
Experiment	2.36	0.41, 0.26, -0.67	1.52	0.47	
DFT 1d2'-NH <sub>3</sub> <sup>†</sup>	1.46	0.78, 0.73, -1.51	2.52	0.06	
(1)	2.29	0.2, 0.2, -0.4	1.61	0.59	
$^{14}\text{N}$ -His332					
Experiment	7.17	0.11, 1.43, -1.54	2.00 <sup>‡</sup>	0.81	
DFT 1d2' <sup>†</sup>	4.83	1.17, 0.97, -2.14	2.13	0.78	
DFT 1d2'-NH <sub>3</sub> <sup>†</sup>	5.23	1.16, 0.97, -2.13	2.15	0.77	
(2)	6.95	0.2, 1.3, -1.5	1.98 <sup>‡</sup>	0.82	

\*Theoretical  $A_{dip}$  values represent a multipole estimate as described in Force et al. (3).

<sup>†</sup>The 1d2' model as reported in Ames et al. (4). 1d2'-NH<sub>3</sub> is an optimized DFT model with NH<sub>3</sub> bound instead of W1.

<sup>‡</sup>The quadrupole tensor was rotated relative to the hyperfine tensor around the Euler angles  $[\alpha \ \beta \ \gamma] = [0 \ -13 \ 26]^\circ$ , similar to ref. 2, where  $[\alpha \ \beta \ \gamma] = [-30 \ 0 \ 40]^\circ$ .

1. Britt RD, Zimmermann JL, Sauer K, Klein MP (1989) Ammonia binds to the catalytic manganese of the oxygen-evolving complex of photosystem II. Evidence by electron spin-echo envelope modulation spectroscopy. *J Am Chem Soc* 111(10):3522-3532.
2. Stich TA, Yeagle GJ, Service RJ, Debus RJ, Britt RD (2011) Ligation of D1-His332 and D1-Asp170 to the manganese cluster of photosystem II from *Synechocystis* assessed by multifrequency pulse EPR spectroscopy. *Biochemistry* 50(34):7390-7404.
3. Force DA, Randall DW, Lorigan GA, Clemens KL, Britt RD (1998) ESEEM studies of alcohol binding to the manganese cluster of the oxygen evolving complex of photosystem II. *J Am Chem Soc* 120(51):13321-13333.
4. Ames W, et al. (2011) Theoretical evaluation of structural models of the S<sub>2</sub> state in the oxygen evolving complex of Photosystem II: Protonation states and magnetic interactions. *J Am Chem Soc* 133(49):19743-19757.

**Table S3. Fitted spin Hamiltonian parameters for the exchangeable  $^{17}\text{O}$  ligands of the OEC in the presence and absence of ammonia**

$^{17}\text{O}$ signal	Fitted spin Hamiltonian parameters/MHz			BS-DFT calculations/MHz	
	$ A_{\text{iso}} $	$A_{\text{dip}}$	$A(\eta)$	$ A_{\text{iso}} $	Site
Strong	9.7	2.2	0.55	—	—
Intermediate	4.5	0.6	0.08	5.20	W2
Matrix	1.4	0.6	0.06	1.69	W1
$\text{NH}_3$					
Strong	7.0	2.2	0.55	—	—
Intermediate	3.1	0.6	0.08	4.32	W2
Matrix	—	—	—	—	—

EDNMR linewidth for  $^{17}\text{O}$  signals: strong, 3.5 MHz [single quantum (SQ)], 7.4 MHz [double quantum (DQ)]; intermediate, 3.3 MHz (SQ), 5.0 MHz (DQ); and matrix, 2.2 MHz (SQ), 3.8 MHz (DQ).

**Table S4. Calculated  $^{17}\text{O}$   $\mu$ -oxo bridge hyperfine couplings: Comparison with experimental parameters**

Method	$S_T$	$\Delta E/\text{cm}^{-1}$	$^{17}\text{O}$ $\mu$ -oxo bridge hyperfine couplings $ A_{\text{iso}} /\text{MHz}^*$				
			O1	O2	O3	O4	O5
DFT							
$1d2^{\dagger}$	1/2	25.6	0.52	23.05	4.90	4.48	17.41
$1d2^{\dagger}\text{-NH}_3^{\ddagger}$	1/2	27.6	1.07	23.19	4.81	5.34	12.21
$\Delta^{\ddagger}$	—	2.0	0.55	0.14	-0.09	0.86	-5.20
$\Delta, \%^{\ddagger}$		7.8	106	1	-2	19	-30
Experiment							
Native	1/2	—			9.7		
+ $\text{NH}_3$	1/2	—					7.0
$\Delta^{\ddagger}$	—	—			2.7		
$\Delta, \%^{\ddagger}$					$-28 \geq O5^{\S}$		

$\Delta E$ , energy-gap between the ground and first excited spin state.  
 $*$ Calculated (raw) BS-DFT hyperfine values are not directly comparable to experiment; the percentage change ( $\Delta$ ) due to ammonia binding can, however, be compared.  
 $^{\dagger}$ The  $1d2^{\dagger}$  model as reported in Ames et al. (9).  $1d2^{\dagger}\text{-NH}_3$  is an optimized DFT model with  $\text{NH}_3$  bound instead of W1.  
 $^{\ddagger}\Delta$  = difference between control and + $\text{NH}_3$  samples.  
 $^{\S}$ The experimental 28% decrease in the oxo bridge hyperfine best matches O5.

**Table S5. Optimized model geometries used for EPR parameter and vibrational frequency calculations**

DFT model	x/Å	y/Å	z/Å
1d2'			
Atom			
Mn	29.19414	36.61847	65.00569
Mn	28.9668	36.43165	67.6823
Mn	29.01561	38.18004	69.82962
Mn	26.62394	38.66455	68.47251
Ca	29.67399	39.73626	66.98265
O	28.45455	37.61803	66.31241
O	30.00886	35.70723	66.38433
O	30.065	37.71235	68.40141
O	28.18288	39.5523	68.91232
O	27.66949	37.12485	68.98152
H	33.26521	35.97244	63.9053
C	33.39239	36.9531	63.41026
H	34.41265	36.98277	62.98899
C	33.18412	38.1003	64.4023
C	31.81431	38.16099	65.07295
O	31.64374	38.90592	66.0647
O	30.89382	37.43168	64.51395
H	23.41284	44.20104	66.83036
C	23.14235	43.30812	66.23537
H	22.05665	43.14138	66.35523
C	23.94833	42.07976	66.67913
C	25.46034	42.28601	66.52075
C	26.33971	41.10987	66.91852
O	27.54446	41.08187	66.55113
O	25.76884	40.18857	67.63863
H	20.97205	34.9217	66.73777
C	21.79667	34.56477	66.09691
C	22.62626	33.58101	66.91447
C	22.67446	35.75242	65.61673
C	23.51361	36.39167	66.68698
N	23.0952	36.51948	68.00583
C	24.74607	37.02593	66.64159
C	24.0326	37.18614	68.71421
N	25.04427	37.51441	67.90507
N	23.39158	32.71597	66.19706
C	24.54488	32.0307	66.78717
H	24.22685	31.56093	67.73365
C	25.70247	33.00813	67.05431
C	26.16809	33.7335	65.79022
C	27.20746	34.80999	66.03121
O	27.51408	35.11177	67.22407
O	27.70084	35.35641	64.97236
H	26.17566	32.17784	73.8084
C	26.68915	33.03106	74.28791
H	26.75269	32.8301	75.37319
C	25.94358	34.34991	74.00002
C	25.82893	34.64465	72.53042
N	24.80965	34.12276	71.74217
C	26.694	35.38315	71.73127
C	25.05611	34.54574	70.49867
N	26.18938	35.30448	70.44992
H	26.4334	38.28926	75.03005
C	26.97487	38.34995	74.06977
H	27.68597	39.19239	74.12322
C	25.99156	38.52463	72.91222
C	26.61796	38.59626	71.52631
O	27.89489	38.44788	71.45365
O	25.83464	38.77529	70.53788
C	31.08901	40.1793	70.05314
O	30.97748	40.51983	68.85136





Table S5. Cont.

DFT model	x/Å	y/Å	z/Å
H	30.91212	33.63988	74.57757
C	30.34207	34.59037	72.68664
C	30.08174	34.22837	71.22035
C	29.73268	35.3885	70.30494
O	29.65	36.55815	70.82011
O	29.52379	35.0971	69.07459
O	22.63212	33.64156	68.16378
H	32.64395	37.33271	62.40745
H	23.33231	32.74842	65.1982
H	26.61563	35.82718	69.6621
H	27.68996	33.06006	73.87756
H	23.29614	43.60325	65.31689
H	31.69436	32.9252	73.13928
H	33.96276	38.11455	65.11608
H	33.29138	39.25805	63.9558
H	26.44387	35.17345	74.50128
H	24.90083	34.29822	74.42841
H	27.58398	35.95587	71.96173
H	24.42251	34.36841	69.61547
H	23.95416	37.43523	69.74653
H	25.43716	37.11327	65.79072
H	22.25621	36.07664	68.38556
H	24.83963	31.22306	66.13913
C	32.09504	40.84653	70.92733
H	31.69138	41.0155	71.93913
H	32.9616	40.16622	71.02109
H	32.43528	41.79442	70.48261
H	31.12589	35.36899	72.73767
H	29.43042	35.0494	73.11437
H	30.95714	33.71789	70.77268
H	29.24247	33.5093	71.13545
H	23.58046	41.26812	66.30434
H	25.65847	42.48922	65.45299
H	23.83853	41.96767	67.90357
H	25.91014	43.15412	67.06524
H	21.99747	36.49542	65.13914
H	21.32706	34.05997	65.20558
H	23.33661	35.39808	64.7911
H	27.53211	37.42481	73.93458
H	25.34557	39.43297	73.00199
H	25.25336	37.67509	72.83987
H	25.35394	33.78164	67.79864
H	25.33028	34.23023	65.29115
H	26.57369	32.9981	65.06393
H	26.52601	32.48263	67.55564
O	29.1129	39.96224	64.51792
H	28.27681	40.44473	64.68325
H	28.81983	39.06806	64.14843
O	28.51217	37.49962	63.55323
H	30.34963	42.45934	67.47842
O	30.04879	42.12468	66.61083
H	29.08907	42.33828	66.57039
H	29.1594	37.55246	62.82261
N	30.03583	35.04332	63.67935
H	30.8881	35.37261	63.21632
H	29.35264	34.77193	62.96706
H	30.27283	34.21138	64.22815

### ***3.2. Characterization of the Oxygen Bridged Manganese Model Complexes Using Multifrequency $^{17}\text{O}$ -Hyperfine EPR Spectroscopies and Density Functional Theory.***

*Leonid Rapatskiy, William M. Ames, Montserrat Pérez-Navarro, Anton Savitsky, Julia J. Griese, Thomas Weyhermüller, Hannah S. Shafaat, Martin Högbom, Frank Neese, Dimitrios A. Pantazis, and Nicholas Cox.*

*Reprinted (adapted) with permission from Journal of Physical Chemistry B, 2015 Vol. 119 (43), pp 13904–1. Copyright 2015 American Chemical Society.*

In this study we examined a series of manganese model complexes by labeling them with the magnetic isotope  $^{17}\text{O}$  and using multifrequency and multiresonance EPR techniques to analyze in detail the electronic properties of their oxygen ligands. The following complexes were studied in this work: synthetic DTNE, BIPY and pivOH complexes, the dimanganese cofactor of Mn catalase, which catalyses the dismutation of  $\text{H}_2\text{O}_2$  to  $\text{H}_2\text{O}$  and  $\text{O}_2$ , and the manganese-iron cofactor of R2lox protein. Interestingly, the experimental isotropic hyperfine coupling seen between different complexes is approximately invariant and lies within the range, from +5.2 to +6.4 MHz, despite the differences in the exact geometry of the bridge, ligand environment, and the polarity of the local environment. That insensitivity can then be used as a marker for this type of bridging unit.

The DFT calculations show a similar invariance in the  $^{17}\text{O}$  bridge hyperfine coupling value within the tolerance typically achieved for ligand hyperfine couplings. It is also unaffected by a different net Mn oxidation state as well. The observed hyperfine coupling was significantly changed only with the protonation of the bridge, leading to a 2-fold increase. This result demonstrates that we should be able to experimentally distinguish  $\mu$ -oxo and  $\mu$ -hydroxo bridging types and defines a kind of fingerprint for the protonation state of the bridge. This fingerprint provides a means of monitoring the  $\mu$ -oxo bridges of metallocofactors, such as the OEC of PS II throughout its catalytic cycle. This is

critical for understanding the chemistry that these metallocofactors perform, since they often use substrates for the reaction they catalyze as bridging species. For example, the Mn catalase takes up hydrogen peroxide (HOOH) as a  $\mu$ -oxo bridge during the dismutation reaction.

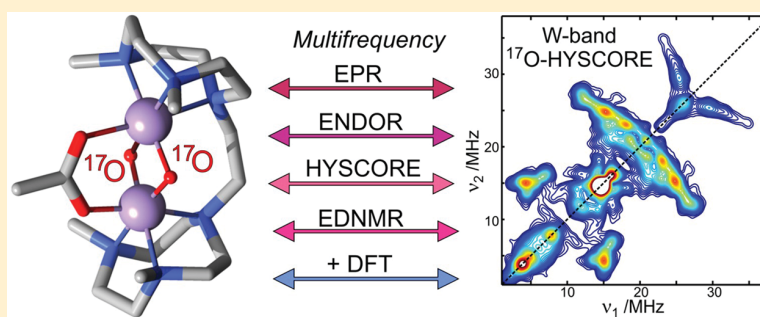
# Characterization of Oxygen Bridged Manganese Model Complexes Using Multifrequency $^{17}\text{O}$ -Hyperfine EPR Spectroscopies and Density Functional Theory

Leonid Rapatskiy,<sup>†</sup> William M. Ames,<sup>†,§</sup> Montserrat Pérez-Navarro,<sup>†</sup> Anton Savitsky,<sup>†</sup> Julia J. Griese,<sup>‡</sup> Thomas Weyhermüller,<sup>†</sup> Hannah S. Shafaat,<sup>†,||</sup> Martin Högbom,<sup>‡</sup> Frank Neese,<sup>†</sup> Dimitrios A. Pantazis,<sup>†</sup> and Nicholas Cox<sup>\*,†</sup>

<sup>†</sup>Max-Planck Institute for Chemical Energy, Stiftstr. 34-36, Mülheim an der Ruhr, DE-45470 Germany

<sup>‡</sup>Department of Biochemistry and Biophysics, Stockholm University, Stockholm SE-106 91, Sweden

**S** Supporting Information



**ABSTRACT:** Multifrequency pulsed EPR data are reported for a series of oxygen bridged ( $\mu$ -oxo/ $\mu$ -hydroxo) bimetallic manganese complexes where the oxygen is labeled with the magnetically active isotope  $^{17}\text{O}$  ( $I = 5/2$ ). Two synthetic complexes and two biological metallocofactors are examined: a planar bis- $\mu$ -oxo bridged complex and a bent, bis- $\mu$ -oxo- $\mu$ -carboxylato bridge complex; the dimanganese catalase, which catalyzes the dismutation of  $\text{H}_2\text{O}_2$  to  $\text{H}_2\text{O}$  and  $\text{O}_2$ , and the recently identified manganese/iron cofactor of the R2lox protein, a homologue of the small subunit of the ribonucleotide reductase enzyme (class 1c). High field (W-band) hyperfine EPR spectroscopies are demonstrated to be ideal methods to characterize the  $^{17}\text{O}$  magnetic interactions, allowing a magnetic fingerprint for the bridging oxygen ligand to be developed. It is shown that the  $\mu$ -oxo bridge motif displays a small positive isotropic hyperfine coupling constant of about +5 to +7 MHz and an anisotropic/dipolar coupling of  $-9$  MHz. In addition, protonation of the bridge is correlated with an increase of the hyperfine coupling constant. Broken symmetry density functional theory is evaluated as a predictive tool for estimating hyperfine coupling of bridging species. Experimental and theoretical results provide a framework for the characterization of the oxygen bridge in Mn metallocofactor systems, including the water oxidizing cofactor of photosystem II, allowing the substrate/solvent interface to be examined throughout its catalytic cycle.

## 1. INTRODUCTION

The development of synthetic catalysts to address a diverse number of chemical problems, from water oxidation to energy storage processes, is turning to nature for inspiration. Biological systems use inexpensive, abundant materials to carry out complex, multielectron chemistry. Of particular interest is the water oxidizing complex (WOC) of photosystem II, which performs the four-electron, four-proton water-splitting reaction. Recent crystallographic data at atomic resolution has resolved the basic topology of the manganese tetramer that comprises the WOC.<sup>1</sup> Five oxygen atoms provide a network of bridges linking the four manganese atoms together.<sup>2</sup> This  $\mu$ -oxo/hydroxo motif is a common structural feature of homo- and heteronuclear metal clusters, where such bridges govern the magnetic (exchange) coupling between the metal ions.

Examples of manganese-containing bioinorganic cofactors include (a) the dimanganese catalase,<sup>3–5</sup> (b) the recently identified Mn containing class Ib and 1c ribonucleotide reductases,<sup>6–9</sup> and (c) the purple acid phosphatases.<sup>10</sup> In each of these examples, the oxygen bridge represents either a substrate of the catalyzed reaction or a structural element introduced during catalyst activation.

Multifrequency electron paramagnetic resonance (EPR) spectroscopies, including multiresonance techniques such as electron spin echo envelope modulation (ESEEM) and

**Special Issue:** Wolfgang Lubitz Festschrift

**Received:** May 13, 2015

**Revised:** July 24, 2015

**Published:** July 30, 2015

electron–nuclear double resonance (ENDOR), represent experimental methods to probe the electronic structure of the oxygen bridge via isotopic labeling with the paramagnetic  $^{17}\text{O}$  nucleus. There are, however, a relatively small number of examples of oxo bridge cofactors characterized by these methods described in the literature. This is due to the low natural abundance (0.038%) of the  $^{17}\text{O}$  isotope together with its less than ideal magnetic properties, including (i) a large nuclear spin  $I = 5/2$ , (ii) a small nuclear  $g$ -factor ( $g_n = -0.757$ ), and (iii) a substantial nuclear quadrupole moment ( $Q = -2.558 \text{ fm}^2$ ). These magnetic characteristics generally yield broad nuclear spectral lines, which are often difficult to characterize via ESEEM. Simultaneously, such signals are expected to appear over the 0–20 MHz range (at low X/Q-microwave frequencies), rendering ENDOR difficult both to perform and to interpret, as the  $^{17}\text{O}$  spectral lines overlap with other nuclei, e.g.,  $^1\text{H}/^2\text{H}$  and  $^{14}\text{N}/^{15}\text{N}$ . Nevertheless, X/Q-ENDOR has been successfully employed to characterize the  $\mu$ -oxo bridge of two Fe containing metallocofactors: the mixed  $\text{Fe}^{\text{II}}\text{Ni}^{\text{III}}$  ( $S = 1/2$ )<sup>11</sup> active site of a class of hydrogenase enzymes and the homometallic  $\text{Fe}^{\text{III}}\text{Fe}^{\text{IV}}$  ( $S = 1/2$ )<sup>12</sup> of the small subunit of class I ribonucleotide reductase. As expected, the reported ENDOR spectra are very broad, with hyperfine couplings in the range 10–15 MHz which display large quadrupole splittings (3–11 MHz), a consequence of the large electric field gradient experienced by the coordinating ligands. Constrained fitting of these data sets was only achieved by resorting to two-dimensional (2D) techniques, where the magnetic field (orientation) dependence of the ENDOR signals was determined.<sup>12</sup>

Mixed valence complexes such as  $\text{Mn}^{\text{II}}\text{Mn}^{\text{III}}$  and  $\text{Mn}^{\text{III}}\text{Mn}^{\text{IV}}$  form an important set of models used to benchmark spectroscopic studies of Mn metallocofactors. These complexes typically exhibit antiferromagnetic coupling leading to the ground state configuration of total electron spin  $S_T = 1/2$ .<sup>4,13–16</sup> The  $S_T = 1/2$  state manifests itself in CW-EPR as a characteristic multiline signal centered at  $g \approx 2$ . This is in contrast to the Ni–Fe and Fe–Fe cofactor systems discussed above,<sup>11,12</sup> both of which display a large  $g$ -anisotropy which defines the width of the signal. The EPR spectrum of Mn complexes is instead defined by the  $^{55}\text{Mn}$  hyperfine structure, as the intrinsic  $g$ -anisotropy is small. These properties however make the characterization of ligand hyperfine coupling of these complexes much more difficult, as 2D experiments are harder to implement.

The Brudvig and Scholes laboratories were the first to characterize the  $\mu$ -oxo bridge for a Mn complex using magnetic resonance techniques, specifically Q-band  $^{17}\text{O}$ -ENDOR.<sup>23</sup> Upon  $^{17}\text{O}$  labeling of the planar BIPY complex, they observed a broad structureless peak from which an isotropic coupling estimate of  $A_{\text{iso}} = 12.8 \text{ MHz}$  was made, consistent with commensurate line broadening observed in the EPR spectrum. No estimates were reported for either the hyperfine anisotropy or quadrupole coupling. A similar signal was later observed for the Mn catalase system, chemically poised in the “super-oxidized”  $\text{Mn}^{\text{III}}\text{Mn}^{\text{IV}}$  oxidation state.<sup>24</sup>

Recently, W-band (95 GHz) EPR has been shown to be ideal for the study of nuclei with low nuclear  $g$ -values, i.e.,  $^{14}\text{N}$  and  $^{17}\text{O}$ .<sup>25–29</sup> At these high frequencies, the nuclear Zeeman term is significantly larger than both the hyperfine and quadrupole terms of the spin Hamiltonian, and thus, these two terms can be treated only to first order. An example is the solvation sphere of  $\text{Ga}^{\text{III}}$  complexes using Mims ENDOR.<sup>27</sup> Similarly,

ESEEM techniques such as hyperfine sublevel correlation (HYSCORE) can be applied at high field to detect the  $^{17}\text{O}$  nucleus,<sup>26</sup> a feat only previously achieved for selected Mo complexes.<sup>30</sup> In our own work, we have used yet another hyperfine spectroscopy, electron–electron double resonance (ELDOR)-detected NMR (EDNMR), a polarization transfer technique analogous to ENDOR.<sup>31,32</sup> Using this technique at the W-band, we could readily detect  $^{17}\text{O}$  signals for Mn model complexes and metallocofactors,<sup>28,29,33</sup> resolving the entire signal envelope. The values we measure for bridge coupling are very different, approximately 2-fold smaller than that of earlier studies. This has prompted us to perform an expanded multifrequency study for a series of oxygen bridged Mn complexes. We thus confirm that our earlier high field estimates are sound. In addition, we can now show that the bridging  $^{17}\text{O}$  hyperfine coupling is sensitive to the protonation state of the bridge. Various broken-symmetry density functional theory (BS-DFT) based methods for estimating hyperfine coupling of bridging ligands are evaluated with respect to their ability to reproduce the experimental data.

## 2. EXPERIMENTAL SECTION

**2.1. DTNE and BIPY Complexes.** The mixed valence  $\text{Mn}^{\text{III}}\text{Mn}^{\text{IV}}$  complexes BIPY and DTNE were prepared using procedures described in the literature.<sup>16–20</sup> Labeling of the  $\mu$ -oxo bridge for each complex is described in Supporting Information S1. The labeling efficiency was assessed using electrospray ionization (ESI) mass spectrometry: BIPY (56% double labeling, 37% mono labeled, 7% unlabeled), DTNE (57% double labeling, 36% mono labeled, 7% unlabeled); see Supporting Information Figures S1.1–6. EPR samples were prepared in either butyronitrile (DTNE) or 1:3 acetonitrile:dichloromethane (BIPY) as a solvent. The final concentration was about 500  $\mu\text{M}$ . Sample tubes were degassed, sealed under a vacuum, and stored in liquid nitrogen.

**2.2. Manganese Catalase.** Mn catalase (MnCat) protein from the thermophilic bacterium *Thermus thermophilus* was used for all EPR measurements. The protein was isolated and purified as described by Barynin et al.<sup>34</sup> The protein was stored in the form of a fine crystalline precipitate in 50%-saturated ammonium sulfate at 4  $^{\circ}\text{C}$ .<sup>34,35</sup> To prepare the superoxidized state, the sample was first washed with aqueous buffer (10 mM  $\text{K}_2\text{HPO}_4$ , pH 6.8). Two 50  $\mu\text{L}$  fractions of the washed sample were then used to prepare the superoxidized state in unlabeled and  $^{17}\text{O}$  labeled water. Both were resuspended in 450  $\mu\text{L}$  of  $\text{KIO}_4$  buffer (5 mM) for 1 h and washed with  $\text{K}_2\text{HPO}_4$  buffer and concentrated to a volume of 20  $\mu\text{L}$ . One sample was washed with 40  $\mu\text{L}$  of  $\text{H}_2^{17}\text{O}$  buffer ( $\times 5$ , 90%  $^{17}\text{O}$  enrichment), and the other sample was washed with unlabeled water ( $\times 5$ ) as a control.  $^{17}\text{O}$  labeled samples were either frozen to  $-80 \text{ }^{\circ}\text{C}$  immediately after preparation or kept for 24 h at room temperature.

**2.3. The Mn/Fe Cofactor of R2lox.** R2lox protein from the thermophilic bacterium *Geobacillus kaustophilus* (*GkR2loxI*) was produced and purified as previously described by Griese et al.<sup>9</sup> The oxidized Mn/Fe cofactor was reconstituted as follows. 200  $\mu\text{M}$  of apoprotein was incubated with 2 equiv of  $\text{MnCl}_2$  and 1 or 2 equiv of  $(\text{NH}_4)_2\text{Fe}(\text{SO}_4)_2$  in 100 mM HEPES-Na pH 7.0, 50 mM NaCl for 1 h at room temperature. Excess metal ions were removed by passing the sample through a HiTrap desalting column equilibrated in 25 mM HEPES-Na pH 7.0, 50 mM NaCl. The  $\text{Mn}^{\text{III}}\text{Fe}^{\text{III}}$  reconstituted protein was concentrated to 0.4–0.6 mM and exchanged into  $\text{H}_2^{17}\text{O}$ -based

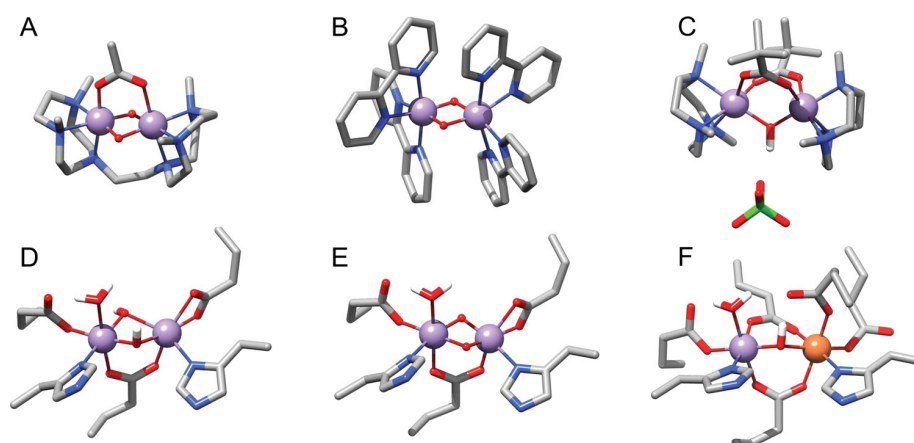


**Figure 1.** Structures of compounds studied in this work. (A) Bent bis- $\mu$ -oxo, mono- $\mu$ -carboxylato  $\text{Mn}^{\text{III}}-(\mu\text{O})_2-\text{Mn}^{\text{IV}}$  DTNE complex;<sup>16,17</sup> (B) planar bis- $\mu$ -oxo  $\text{Mn}^{\text{III}}-(\mu\text{O})_2-\text{Mn}^{\text{IV}}$  BIPY complex;<sup>18–20</sup> (C) mono- $\mu$ -hydroxo, bis- $\mu$ -carboxylato  $\text{Mn}^{\text{II}}-(\mu\text{OH})-\text{Mn}^{\text{III}}$  PivOH complex;<sup>21</sup> (D, E) the Mn/Mn cofactor of *Thermus thermophilus* catalase (**MnCat**) poised in the  $\text{Mn}^{\text{II}}\text{Mn}^{\text{III}}$  (bis- $\mu$ -hydroxo, mono- $\mu$ -carboxylato) and  $\text{Mn}^{\text{III}}\text{Mn}^{\text{IV}}$  (bis- $\mu$ -oxo, mono- $\mu$ -carboxylato) oxidation level;<sup>3,4</sup> (F) the  $\text{Mn}^{\text{III}}\text{Fe}^{\text{III}}$  cofactor of the **R2lox** protein (mono- $\mu$ -hydroxo, bis- $\mu$ -carboxylato).<sup>9,22</sup> The bridging  $\mu$ -oxo oxygen atoms of the BIPY complex are identical, whereas the bridging  $\mu$ -oxo oxygen atoms of the DTNE and MnCat complexes are not strictly identical.

buffer (25 mM HEPES-Na pH 7.0, 50 mM NaCl in 90%  $\text{H}_2^{17}\text{O}$ ) by four rounds of dilution and concentration. 50% (v/v) glycerol was added to the samples before transfer into sample holders and flash cooling in liquid nitrogen, so that the final protein concentration was 0.2–0.3 mM.

**2.4. X-, Q-Band EPR Experiments.** X-Band CW and pulse EPR measurements were performed using a Bruker ELEXSYS 580 spectrometer, equipped with an Oxford Instruments ESR 935 cryostat and ITC4 temperature controller. Q-band pulse EPR measurements were performed at 40 K using a Bruker ELEXSYS E580 Q-band pulse EPR spectrometer, equipped with a home-built TE<sub>011</sub> microwave cavity,<sup>36</sup> Oxford-CF935 liquid helium cryostat, and ITC-503 temperature controller. All ENDOR data were collected using an external home-built computer console (SpecMan4EPR control software<sup>37</sup>) with the ELEXSYS E580 X-band pulse EPR spectrometer, coupled to an external RF generator and RF amplifier (ENI S100L). Electron spin echo-detected (ESE) field-swept spectra were measured using the pulse sequence  $t_p-\tau-2t_p-\tau$ -echo. The length of the  $\pi/2$  microwave pulse was generally set to  $t_p = 8$  ns (X-band), 36 ns (Q-band). The interpulse distance was varied in the range  $\tau = 200$ –500 ns (X/Q-band). Using either an FID detection or Hahn echo sequence did not significantly change the measured pulse spectrum. The relatively slow  $T_1$  relaxation time observed for these complexes required the measurement temperature to be above 30 K for efficient data collection (shot repetition rates of 1 kHz).

Davies type  $^{17}\text{O}$  ENDOR spectra were acquired using the pulse sequence  $t_{\text{inv}}-t_{\text{RF}}-T-t_p-\tau-2t_p-\tau$ -echo using a length of inversion microwave  $\pi$  pulse of  $t_{\text{inv}} = 128$  ns and a radio frequency  $\pi$  pulse length of  $t_{\text{RF}} = 6$   $\mu\text{s}$ . The length of  $\pi/2$  microwave pulse in the detection sequence was generally set to  $t_p = 64$  ns and the interpulse delays to  $T = 1.5$   $\mu\text{s}$  and  $\tau = 468$  ns. Mims type  $^{17}\text{O}$  ENDOR spectra were collected using the pulse sequence  $t_p-\tau-t_p-t_{\text{RF}}-T-t_p-\tau$ -echo, with  $t_p = 8$  ns,  $t_{\text{RF}} = 6$   $\mu\text{s}$ ,  $\tau = 300$ –500 ns, and  $T = 2$   $\mu\text{s}$ . The RF frequency was swept 20 MHz around the  $^{17}\text{O}$ -Larmor frequency of about 3 MHz (340 mT) in 50 kHz steps. All ENDOR measurements were performed using the random (stochastic) acquisition technique, as described in Epel et al.<sup>37</sup>

**2.5. W-Band EPR Experiments.** High-field EPR experiments were performed using a W-band EPR spectrometer (Bruker EleXsys E680), equipped with a home-built ENDOR microwave cavity optimized for maximum RF performance at low RF frequencies (<100 MHz, optimum performance at 20 MHz).<sup>29</sup> Electron spin echo-detected (ESE) field-swept spectra were measured using the pulse sequence  $t_p-\tau-2t_p-\tau$ -echo with  $t_p = 24$  ns and  $\tau = 200$ –500 ns. HYSOCORE spectra were collected using the  $t_p-\tau-t_p-t_1-2t_p-t_2-t_p-\tau$ -echo sequence with  $t_p = 20$  ns,  $\tau = 396, 408,$  and 420 ns, and  $t_1, t_2 = 100$ –1124 ns in 8 ns steps. Davies type  $^{17}\text{O}$ -ENDOR spectra were collected using the  $t_{\text{inv}}-t_{\text{RF}}-T-t_p-\tau-2t_p-\tau$ -echo sequence with  $t_{\text{inv}} = 128$  ns,  $t_p = 64$  ns,  $t_{\text{RF}} = 15$   $\mu\text{s}$ ,  $T = 4$   $\mu\text{s}$ , and  $\tau = 600$  ns.  $T$ -averaged Mims type  $^{17}\text{O}$  ENDOR spectra were collected using the  $t_p-\tau-t_p-t_{\text{RF}}-T-t_p-\tau$ -echo sequence with  $t_p = 24$  ns,  $t_{\text{RF}} = 15$   $\mu\text{s}$ ,  $T = 4$   $\mu\text{s}$ , and  $\tau = 164$ –332 ns in 12 ns steps. The RF frequency was swept 23.5 MHz around the  $^{17}\text{O}$ -Larmor frequency of about 19.7 MHz (3.4 T) in 200 kHz steps. ELDOR-detected NMR (EDNMR) measurements were performed using the pulse sequence  $t_{\text{HTA}}-T-t_p-\tau-2t_p-\tau$ -echo. The high tuning angle (HTA) microwave pulse was applied at microwave frequency  $\nu_{\text{mw}}$ . The detection Hahn echo pulse sequence  $t_p-\tau-2t_p-\tau$ -echo at microwave frequency  $\nu_{\text{mw}}^{(0)}$  matched to the cavity resonance was set 2  $\mu\text{s}$  post HTA pulse to ensure the decay of the electron spin coherence. The pulse length for a detection  $\pi/2$  pulse  $t_p = 40$ –200 ns and the pulse separation  $\tau = 600$  ns were generally set. The echo was integrated  $\sim 1000$  ns around its maximum. The spectra were acquired continuously sweeping the HTA frequency  $\nu_{\text{mw}}$  at fixed  $B_0$ . A low-power HTA microwave pulse of  $t_{\text{HTA}} \approx 8$   $\mu\text{s}$  length was used to minimize the width of the central hole. Tabulated pulse EPR parameters for each experiment are given in Supporting Information Table S2.1.

**2.6. Spectral Simulations.** EPR/ENDOR/HYSOCORE/EDNMR spectra were simultaneously fit assuming an effective spin  $S = 1/2$  ground state (see section 3.2). The electron Zeeman, nuclear Zeeman, and hyperfine terms were treated exactly. Spectral simulations were performed numerically using the EasySpin package<sup>38,39</sup> in MATLAB.

**2.7. Geometry Optimizations and EPR Parameter Calculations Using BS-DFT.** The models were optimized in their high spin states using the B3LYP functional<sup>40–42</sup> along with the D3 dispersion corrections from Grimme with the Becke–Johnson damping scheme.<sup>43,44</sup> The zero-order regular approximation (ZORA) was used to account for relativistic effects, while the conductor-like screening model (COSMO) was used to model solvent effects.<sup>45–49</sup> For small molecule complexes, acetonitrile was used as the solvent ( $\epsilon = 36.60$ ). The ZORA-recontracted versions of the def2-TZVP(-f) basis sets were used for all atoms except C and H, for which the corresponding ZORA SVP basis sets were employed.<sup>50,51</sup> Optimizations took advantage of the resolution of the identity approximation for Coulomb exchange (RI-J)<sup>52</sup> and the chain-of-spheres approximation (COSX) for Hartree–Fock exchange,<sup>53</sup> as implemented in ORCA,<sup>54</sup> with the decontracted auxiliary def2-TZVPP/J Coulomb fitting basis sets.<sup>55</sup> Tight SCF convergence criteria were used throughout. All broken-symmetry single-point calculations and all calculations of reported EPR parameters were computed with the TPSSh functional<sup>56</sup> and ZORA def2-TZVP(-f) basis sets on all atoms. Hyperfine tensors for the N, O, Mn, and Fe atoms were calculated from the broken-symmetry solution using the same methodology as described previously for model Mn<sup>II</sup>Mn<sup>III</sup> PivOH and R2lox  $S = 1/2$  complexes,<sup>22,57</sup> with locally dense integration grids and basis sets extended in the core region.

**2.8. Construction of Protein Cluster Models.** For protein bioinorganic complexes, cluster models were constructed from available published crystal structures (2V8U and 4HR0 for dimanganese catalase<sup>5</sup> and R2lox,<sup>9</sup> respectively). Cluster models were constructed using all transition metal (Mn or Fe) coordinating residues,  $\mu$ -oxo/hydroxo bridges, and water molecules from chain A of the crystal structures. Amino acids were truncated at the  $\alpha$ -C, while the fatty acid ligand of R2lox was truncated as a three carbon atom hydrocarbon chain (see Figure 1). Hydrogen atoms were then added to fill in the remaining valence, after which a preliminary optimization of only the hydrogen atoms was performed. Subsequent to the hydrogen-only optimization, the positions of the hydrogen atoms on the terminal carbon atoms were constrained and a full geometry optimization with all other atoms free was performed. These models were then used in the single point broken-symmetry and EPR parameter calculations. All calculations of the protein models used a dielectric constant of  $\epsilon = 4.0$  in conjunction with COSMO. In all other aspects, the optimizations of the cluster models followed the same methodology as that for the small molecule complexes.

### 3. THEORY

**3.1. The Spin Hamiltonian Formalism.** Here we consider an antiferromagnetically exchange coupled Mn<sup>III</sup>-O<sub>2</sub>-Mn<sup>IV</sup> dimer. A basis set that describes the Mn-dimer spin manifold can be built from the product of the eigenstates of the interacting spins:

$$|S_1M_1\rangle \otimes |S_2M_2\rangle \otimes |I_1m_1\rangle \otimes |I_2m_2\rangle \quad (1)$$

Here  $S_i$  refers to the electronic spin state of Mn<sub>*i*</sub>,  $M_i$  refers to the electronic magnetic sublevel,  $I_i$  refers to the nuclear spin state of <sup>17</sup>O, and  $m_i$  refers to the nuclear magnetic sublevel of <sup>17</sup>O. The metal (<sup>55</sup>Mn) spin quantum numbers are excluded for simplicity. The full basis set is given in Supporting Information S6.  $S_i$  takes the value 2 for Mn<sup>III</sup> and 3/2 for Mn<sup>IV</sup>;  $M_i$  takes the values  $S_i, S_i - 1, \dots, 1 - S_i, -S_i$ ;  $I_i$  takes the value 5/2 for <sup>17</sup>O

and  $m_i$  takes the values  $-I_i, 1 - I_i, \dots, I_i - 1, I_i$ . The spin Hamiltonian that describes the spin manifold of the <sup>17</sup>O labeled Mn dimer is

$$\begin{aligned} \hat{H} = & -2J\vec{S}_1\cdot\vec{S}_2 + \sum_{i=1,2} \vec{S}_i\cdot\mathbf{d}_i\cdot\vec{S}_i + \beta \sum_{i=1,2} \vec{B}_0\cdot\mathbf{g}_i\cdot\vec{S}_i \\ & - g_n\beta_n \sum_{k=1,2} \vec{B}_0\cdot\vec{I}_k + \sum_{i=1,2} \sum_{k=1,2} \vec{S}_i\cdot\mathbf{a}_{i,k}\cdot\vec{I}_k \\ & + \sum_{k=1,2} \vec{I}_k\cdot\mathbf{p}_k\cdot\vec{I}_k \end{aligned} \quad (2)$$

It contains (i) an electron–electron spin coupling term for the Mn–Mn interaction, (ii) a fine structure term for each Mn ion, (iii) an electronic Zeeman term for each Mn ion, (iv) a nuclear Zeeman term for each <sup>17</sup>O nucleus, (v) an electron–nuclear hyperfine term for each <sup>17</sup>O nucleus, and (vi) a nuclear quadrupole term for each <sup>17</sup>O nucleus.

**3.2. The Effective Spin 1/2 Ground State.** The electronic coupling between the two Mn ions in mixed valence Mn dimers is usually dominated by the through bond exchange interaction and is sufficiently large that the spin manifold can be treated within the strong exchange limit. In this instance, the exchange interaction between the two Mn ions is significantly larger than any other term of the spin Hamiltonian.<sup>14,19,58</sup> The resultant electronic spin states of the manifold are then adequately described by a single quantum number, the total spin ( $S_T$ ).<sup>59</sup> The “multiline” EPR signal observed is derived from only one total spin state, the ground state of the spin manifold with total spin  $S_T = 1/2$ . The basis set that describes this subspace takes the form

$$|S_T M_T I_1 m_1 m_2\rangle \quad (3)$$

where  $M$  takes all half-integer values:  $-1/2 \leq M \leq 1/2$  and  $m_i$  (where  $i = 1-2$ ) takes all half integer values:  $-5/2 \leq m_i \leq 5/2$ . The effective spin Hamiltonian that describes the ground state of the spin manifold ( $S_T = 1/2$ ) is

$$\begin{aligned} \hat{H} = & +\beta\vec{B}_0\cdot\mathbf{G}\cdot\vec{S}_T - g_n\beta_n \sum_{k=1,2} \vec{B}_0\cdot\vec{I}_k + \sum_{k=1,2} \vec{S}_T\cdot\mathbf{A}_k\cdot\vec{I}_k \\ & + \sum_{k=1,2} \vec{I}_k\cdot\mathbf{p}_k\cdot\vec{I}_k \end{aligned} \quad (4)$$

It contains (i) an effective electronic Zeeman term for the total electronic spin, (ii) nuclear Zeeman terms for each <sup>17</sup>O nucleus, (iii) effective electron–nuclear hyperfine terms for each <sup>17</sup>O nucleus, and (iv) nuclear quadrupole terms for each <sup>17</sup>O nucleus. Note that throughout the text lower case letters are used for spin Hamiltonian parameters in the uncoupled representation (site parameters) whereas upper case letters are used for spin Hamiltonian parameters in the coupled representation (measured / projected parameters).

**3.3. Hyperfine Tensor Decomposition.** The ligand terms described here are described in terms of two tensor components, the isotropic coupling  $A_{\text{iso}}$  and the anisotropic coupling  $A_{\text{aniso}}$  (ignoring the antisymmetric term)

$$\mathbf{A} = A_{\text{iso}}\mathbf{I} + \mathbf{A}_{\text{aniso}} \quad (5)$$

where  $A_{\text{iso}}$  is the trace of the hyperfine tensor and  $I$  is the identity matrix.  $A_{\text{aniso}}$  in its diagonalized form is defined here in terms of two parameters  $D$  and  $\eta$ :

$$\mathbf{A}_{\text{aniso}} = D \cdot \begin{bmatrix} -(1 + \eta) & 0 & 0 \\ 0 & -(1 - \eta) & 0 \\ 0 & 0 & 2 \end{bmatrix} \quad (6)$$

The rhombicity ( $\eta$ ) is expected to be small for terminal ligands but may be large for bridging ligands due to the interaction with more than one spin center/fragment (see [Supporting Information S7](#)).

**3.4. Isotropic Spin Projections.** A mapping of the spin subspace in [section 3.2](#) onto the original basis set as described in [section 3.1](#) can be made. This allows the intrinsic  $g$  and hyperfine tensors ( $\mathbf{g}_i, \mathbf{a}_{i,k}$ , see [eq 2](#)) to be calculated from the effective  $G$  and hyperfine tensors ( $\mathbf{G}, \mathbf{A}_k$ , see [eq 4](#)).<sup>58–60</sup> These weighting factors are termed spin-projection coefficients. The isotropic spin projection coefficients ( $\rho_i$ ) are defined in terms of the ratio of the spin expectation value  $S_z$  of the  $i$ th spin center and the total spin  $S_T$ :

$$\rho_i = \frac{\langle S_{i,z} \rangle}{S_T} \quad (7)$$

For a two-spin system ( $S_1, S_2$ ), there exists an explicit solution for the two spin projections ( $\rho_1, \rho_2$ ) which define this mapping.<sup>59</sup>

$$\rho_{i=1,2} = \frac{S_i(S_i + 1) - S_{3-i}(S_{3-i} + 1) + S_T(S_T + 1)}{2S_T(S_T + 1)} \quad (8)$$

Expressing then the effective isotropic  $G$  and hyperfine values ( $A_k$ ) yields<sup>59</sup>

$$G = \sum_{i=1,2} \rho_i g_i \quad \text{and} \quad A_{k=1,2} = \sum_{i=1,2} \rho_i a_{i,k} \quad (9)$$

For example, for a  $\text{Mn}^{\text{III}}\text{Mn}^{\text{IV}}$  dimer,  $S_1(\text{Mn}^{\text{III}}) = 2$  and  $S_2(\text{Mn}^{\text{IV}}) = 3/2$ , [eq 8](#) yields isotropic spin projection values of  $\rho_1 = 2$  and  $\rho_2 = -1$ , respectively. Inserting these values into [eq 9](#) yields formulas for the effective  $G$  and hyperfine tensors:  $G = 2g_1 - g_2$ ,  $A_1 = 2a_{\text{O},11} - a_{\text{O},12}$ ;  $A_2 = 2a_{\text{O},12} - a_{\text{O},22}$ .<sup>60,61</sup>

**3.5. Broken Symmetry DFT Calculation of Hyperfine Coupling Constants.** The projection of the hyperfine coupling constants calculated using broken symmetry DFT (BS-DFT) for terminal ligands coordinated to a metal spin center has been discussed previously in the literature.<sup>62</sup> As described above, the measured (projected) hyperfine coupling for a particular nucleus ( $k$ ) represents the site hyperfine coupling ( $a_k$ ) multiplied by the spin projection factor  $\rho_i$  associated with the metal ( $i$ th spin center) it is ligated to

$$A_k = \rho_i a_k \quad (10)$$

with the spin projection ( $\rho_i$ ) calculated as the ratio of spin expectation value  $S_z$  of the broken symmetry wave function and the total spin quantum number ( $S_T$ ). It is noted that the site hyperfine is not directly calculated using BS-DFT. The as-calculated “raw” BS-DFT value, labeled with the superscript “BS” ( $a_k^{\text{BS}}$ ), must first be multiplied by a constant to account for the BS calculation being incorrectly scaled; in the broken symmetry solution, the calculated hyperfine values reflect the coupling of the nuclear spin  $k$  to a fictitious  $S = 1/2$  electronic spin. To calculate the site hyperfine, this value must be scaled to take into account the actual spin state of the metal which ligates the nuclear spin; i.e., the raw hyperfine is scaled by the ratio of the expectation value of the fictitious electronic spin

operator (i.e.,  $M_z$ ), divided by the site spin quantum number ( $S_i$ ).

$$a_k = \pm a_k^{\text{BS}} \frac{\langle S_z \rangle^{\text{BS}}}{S_i} \quad (11)$$

For the calculations presented here,  $S_i$  refers to the spin quantum number of the spin fragment the nuclear spin couples to, in this instance either the  $\text{Mn}^{\text{III}}$  ion ( $S_{i=1} = 2$ ) or the  $\text{Mn}^{\text{IV}}$  ion ( $S_{i=2} = 3/2$ ).  $\langle S_z \rangle^{\text{BS}}$  is the spin expectation value for the broken system solution. This takes only one value, i.e.,  $1/2$ , as only the ground state configuration is considered. Note that the spin density (Fermi contact interaction) appears only once in [eq 11](#); it is contained in the raw hyperfine value. The hyperfine values are signed quantities. Assuming a fixed sign for the site hyperfine coupling, the projected hyperfine of nucleus ( $k$ ) will be either positive or negative depending on whether it is ligated to the spin center (forms part of the spin fragment) that carries either majority ( $\alpha$ ) or minority ( $\beta$ ) spin. The formalism shown in [eq 11](#) generalizes for all components of the hyperfine tensor. For more information on the projection of calculated BS-DFT values for comparison with experiment, we refer the reader to refs [62–65](#).

For bridging ligands, the  $k$ th nucleus cannot be assigned to a single spin-centered system. This then poses a problem as to how to best interpret the raw hyperfine values. Although at present no rigorous method exists to achieve an appropriate spin projection as described above for terminal ligands. Here we have evaluated three possible approximations.

- (i) As the spin density of the bridging ligand cannot be sensibly decomposed into two site interactions with each spin fragment and the BS-DFT solution is correctly scaled in terms of the total spin multiplicity, the raw hyperfine value ( $a_k^{\text{BS}}$ ) might be used as a first approximation for the correct value. Importantly, as  $a_k^{\text{BS}}$  scales with the Fermi contact term, this parameter should at least reproduce the trend in hyperfine couplings seen across the different models. Thus, this serves as the simplest way to validate if BS-DFT is appropriate for the calculation of bridging hyperfine coupling constants.
- (ii) The second approach is simply to average the two projected hyperfine couplings for the bridging ligand, as has been proposed in earlier literature by Noodleman and co-workers.<sup>66,67</sup> In this instance, the raw hyperfine value ( $a_k^{\text{BS}}$ ) for the bridging ligand is projected for each metal ion (spin fragment) individually ([eqs 10 and 11](#)), summed and averaged

$$A_{k=1,2} = \frac{\rho_1 a_{1k} + \rho_2 a_{2k}}{2} \quad (12)$$

For this method, as the same raw hyperfine value is used to calculate the two site hyperfine values, [eq 12](#) can be re-expressed as

$$A_{k=1,2} = \frac{a_k^{\text{BS}}}{2} \left( \frac{\langle S_z \rangle^{\text{BS}}}{S_1} |\rho_1| + \frac{\langle S_z \rangle^{\text{BS}}}{S_2} |\rho_2| \right) \quad (13)$$

For a  $\text{Mn}^{\text{III}}\text{Mn}^{\text{IV}}$  complex, [eq 13](#) simply reduces to

$$A_{k=1,2} = \frac{5}{12} a_k^{\text{BS}} \quad (14)$$

And the corresponding  $\text{Mn}^{\text{II}}\text{Mn}^{\text{III}}$  complex and the isoelectronic  $\text{Mn}^{\text{III}}\text{Fe}^{\text{III}}$  complex:

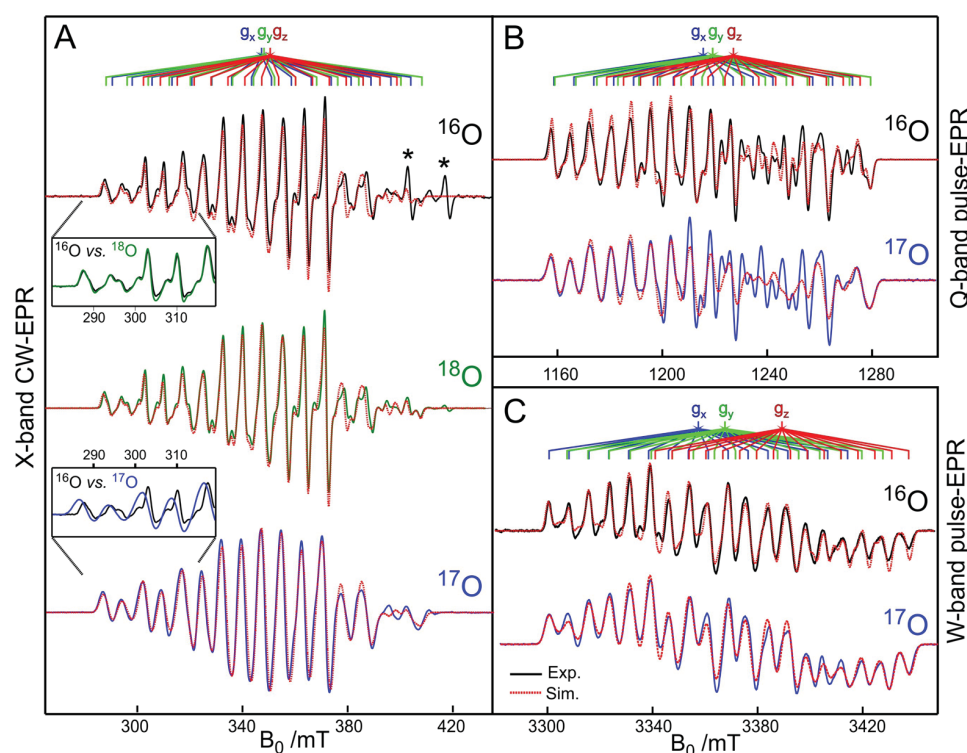


**Figure 2.** (A) CW X-band EPR spectra of the DTNE complex containing the  $^{16}\text{O}$ ,  $^{17}\text{O}$ , and  $^{18}\text{O}$  isotopes in frozen solution of butyronitrile (40 K). (B, C) Corresponding Q-band and W-band pulse EPR data. Pulse EPR data are pseudomodulated with a Bessel function of the first kind. Spin Hamiltonian simulations are shown by the red dashed lines superimposing the data. All experimental parameters are given in [Supporting Information S2](#), and simulation parameters are given in [Supporting Information S6](#). Asterisks (\*) indicate background resonator signals.

$$A_{k=1,2} = \frac{4}{10} a_k^{\text{BS}} \quad (15)$$

- (iii) The third approach directly follows from the spin projection mapping used to scale hyperfine parameters from the uncoupled to the coupled spin Hamiltonian representation. As with the second approach, it does however assume that the calculated hyperfine value ( $a_k$ ) represents the site hyperfine coupling for the bridging ligand interacting with each metal site. In practice, this cannot be the case, as these two interactions involve different orbitals. Thus, *ab initio* methods, beyond the scope of this work, are necessary to decompose the calculated hyperfine into its two components for a completely robust methodology. As implied from eq 7, the projected hyperfine is the sum of the two site interactions:

$$A_{k=1,2} = \sum_{i=1,2} \rho_i a_{ik} = \rho_1 a_{1k} + \rho_2 a_{2k} \quad (16)$$

As per eq 12, the raw hyperfine value is the same for both terms of eq 16, and as such, it can be re-expressed as

$$A_{k=1,2} = a_k^{\text{BS}} \left( \pm \frac{\langle S_z \rangle^{\text{BS}}}{S_1} \rho_1 \mp \frac{\langle S_z \rangle^{\text{BS}}}{S_2} \rho_2 \right) \quad (17)$$

For a  $\text{Mn}^{\text{III}}\text{Mn}^{\text{IV}}$  complex, eq 17 simply reduces to

$$A_{k=1,2} = \frac{5}{6} a_k^{\text{BS}} \quad (18)$$

And the corresponding  $\text{Mn}^{\text{II}}\text{Mn}^{\text{III}}$  complex and the isoelectronic  $\text{Mn}^{\text{III}}\text{Fe}^{\text{III}}$  complex:

$$A_{k=1,2} = \frac{4}{5} a_k^{\text{BS}} \quad (19)$$

Thus, it can be readily inferred that method i will always give the largest hyperfine estimate, method ii will always give the smallest hyperfine estimate, which for these systems is approximately half the raw hyperfine coupling, and method iii will yield a value in between.

## 4. RESULTS AND DISCUSSION

**4.1. EPR Spectroscopy.** **4.1.1. Multifrequency CW/Pulse EPR.** CW and pulse EPR data of the  $\text{Mn}^{\text{III}}\text{Mn}^{\text{IV}}$  DTNE complex in frozen solution of butyronitrile are presented in [Figure 2A](#). A 16-line EPR pattern of approximately the same total spectral breadth was observed at all microwave frequencies.<sup>15,16,68</sup> Such spectra are typical for mixed valence  $\text{Mn}^{\text{II}}\text{Mn}^{\text{IV}}$  complexes in which the *g*-anisotropy is small and the two metal hyperfine couplings define the structure of the signal. The EPR line width of the 16 major lines is narrow, and additional side lines are resolved throughout the EPR spectrum (fwhm  $\approx$  3 mT – X-band). This side structure is more readily observed at X-band, suggesting field inhomogeneity (*g*-strain) contributes to the EPR line width at higher frequencies. Similar results were obtained for the  $^{16}\text{O}$  labeled BIPY complex; see [Supporting Information S2](#). The  $^{17}\text{O}$  label was incorporated via isotope exchange with  $^{17}\text{O}$  labeled water; see [Supporting Information S1](#). As expected, incorporation of the  $^{17}\text{O}$  isotope caused a significant increase in the EPR line width observed at all microwave frequencies. This is because each spectral line splits

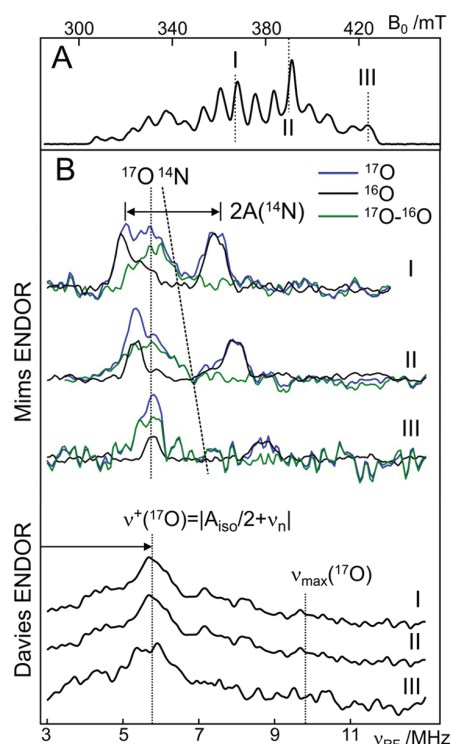
due to the new hyperfine interaction between the electron spin and the  $^{17}\text{O}$  nucleus. This splitting is however smaller than the intrinsic EPR line width, and as such manifests only as an EPR line broadening. The extent of this broadening is most readily observed at X-band (fwhm  $\approx 4$  mT – X-band). The same labeling procedure was repeated with  $^{18}\text{O}$  labeled water to demonstrate that oxygen atom exchange does not influence the intrinsic EPR line width. As expected, the  $^{18}\text{O}$  labeled DTNE complex was identical to the unlabeled  $^{16}\text{O}$  DTNE complex, as both the  $^{16}\text{O}$  and  $^{18}\text{O}$  isotopes do not have a nuclear spin.

Figure 2 shows a spin Hamiltonian simulation to account for the observed line width broadening. These simulations assume a  $^{17}\text{O}$  labeling efficiency of 57% double, 36% mono, and 7% unlabeled, as determined by ESI mass spectrometry; see Supporting Information S1. The effective G tensor and  $^{55}\text{Mn}$  hyperfine tensor values used for the simulation are approximately the same as those determined previously.<sup>15,16,68</sup> The line broadening seen upon  $^{17}\text{O}$  label incorporation was reproduced with an equivalent hyperfine coupling for the two  $\mu$ -oxo bridges of  $\sim 15$  MHz. Approximately the same line broadening was observed for the  $^{17}\text{O}$ -BIPY complex as compared to the  $^{16}\text{O}$ -BIPY complex. This was modeled with an equivalent hyperfine coupling for the two  $\mu$ -oxo bridges of  $\sim 13$  MHz, equivalent to the value reported by Usov et al.,<sup>23</sup> see Supporting Information S2.

**4.1.2. X-Band Mims/Davies  $^{17}\text{O}$ -ENDOR.** To further characterize the  $^{17}\text{O}$  hyperfine interaction, both Mims and Davies ENDOR experiments were performed for the  $^{16}\text{O}$  and  $^{17}\text{O}$  labeled DTNE complex (Figure 3). For the  $^{16}\text{O}$  sample, two sharp lines at 5.5 and 7.5 MHz were observed using Mims ENDOR, split by  $\sim 2$  MHz. The doublet had a pronounced magnetic field dependence, with the center of the doublet shifting 0.5–1.0 MHz to higher frequency when comparing to the ENDOR spectrum, collected at the high and low edge of the EPR signal. This doublet is consistent with its assignment to the  $^{14}\text{N}$  ligand(s). These signals were not as readily observed in the corresponding Davies ENDOR experiment, presumably because they exhibit only a small hyperfine coupling and are thus likely suppressed.

For the corresponding  $^{17}\text{O}$  labeled DTNE complex, a new, broad signal was observed in both Mims and Davies ENDOR spectra, extending from less than 4 MHz to at least 10 MHz with a peak maximum at  $\sim 6$  MHz. Unlike the background  $^{14}\text{N}$  doublet, the frequency position/line shape of this new signal does not significantly change with the external magnetic field, consistent with its assignment to an  $^{17}\text{O}$  ligand in the strong hyperfine coupling limit ( $|A| \gg 2\nu_n$ ). It is suspected that this turning point only represents half of the  $^{17}\text{O}$ -ENDOR signal, specifically the plus ( $\nu^+$ ) branch of the total signal; see section 4.1.8. Assuming the hyperfine coupling is isotropic and quadrupole splitting is ignored, the position of the  $^{17}\text{O}$ -ENDOR signal is given by the equation  $\nu^+ = |A_{\text{iso}}|/2 + \nu_n$ , where  $A_{\text{iso}}$  is the isotropic hyperfine coupling and  $\nu_n$  the Larmor frequency of the  $^{17}\text{O}$  nucleus at a given magnetic field [ $\nu_n(^{17}\text{O}) = 2.02$  MHz,  $B_0 = 350$  mT]. This yields a  $^{17}\text{O}$  hyperfine coupling estimate of  $\sim 7.5$  MHz, significantly smaller than that inferred from the line width broadening seen in the EPR spectrum.

**4.1.3. W-Band  $^{17}\text{O}$ -EDNMR.** The EPR line shape analysis and X-band ENDOR data presented above clearly do not give the same hyperfine coupling value. The reason for this however is already evident from the ENDOR data. These spectra resolve very broad  $^{17}\text{O}$  spectral lines, indicating that the hyperfine



**Figure 3.** (A) X-band echo detected EPR spectrum of the DTNE complex. (B) Corresponding  $^{17}\text{O}$ -ENDOR data collected at three magnetic field positions marked in part A. The colored traces represent Mims ENDOR spectra of the  $^{17}\text{O}$  labeled (blue) and  $^{16}\text{O}$  labeled (black) complex. The difference is shown in green. The black trace at the bottom represents corresponding Davies ENDOR spectra. For all data, a 3 pt point smoothing function was applied. I, II, and III indicate the three magnetic field positions ( $B_0$ ) where the ENDOR spectra were collected. All EPR parameters are given in the Experimental Section.

tensor has a large anisotropic contribution. They may also indicate that the nuclear quadrupole interaction is large. To better determine these parameters, EPR measurements at W-band frequency were performed. At high field (3.4 T), the nuclear Zeeman term for all first coordination sphere  $^{17}\text{O}/^{14}\text{N}$  ligands is significantly larger as compared to the hyperfine estimate, falling now in the weak coupling regime ( $|A| < 2\nu_n$ ). Spectral peaks should now appear as a simpler pattern about the Larmor frequency split by the hyperfine. It is also noted that the Larmor frequency of  $^{17}\text{O}$  [ $\nu_n(^{17}\text{O}) = 19.6$  MHz,  $B_0 = 3.4$  T] is significantly different from that of  $^{14}\text{N}$  [ $\nu_n(^{14}\text{N}) = 10.5$  MHz], thus allowing both components to be readily distinguished from each other, as they appear in different frequency regions. ENDOR measurements at W-band were attempted for both the DTNE and BIPY complex; however, spectra of sufficient quality for analysis could not be obtained.

In contrast to ENDOR, high quality EDNMR spectra were obtained for both complexes. The 2D EDNMR surface of the  $^{17}\text{O}$  labeled mixed-valent  $\text{Mn}^{\text{III}}\text{-}\mu\text{O}_2\text{-Mn}^{\text{IV}}$  DTNE complex is shown in Figure 4. The key advantage of this technique were outlined in our earlier study.<sup>29</sup> In particular, the high sensitivity of this technique allows 2D experiments, where the EDNMR data are collected across the EPR spectrum. Control  $^{16}\text{O}$  DTNE complex data are shown in black in Figure 4B, resolving signals attributable to a  $^{14}\text{N}$  ligand. Both single and double

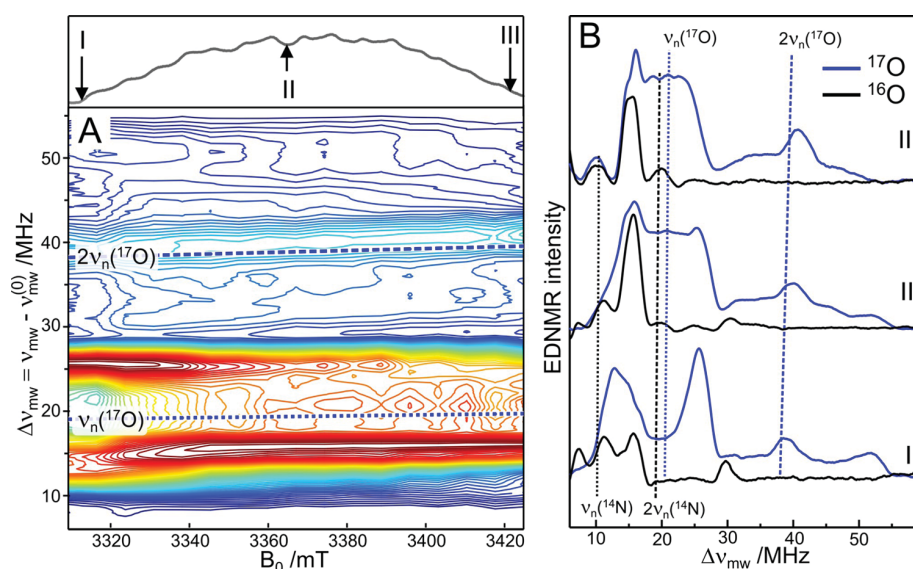


**Figure 4.** (A) Two dimensional representation (contour map) of the W-band EDNMR spectrum of the  $^{17}\text{O}$  labeled DTNE complex. (B) A comparison of the EDNMR signal seen for the  $^{17}\text{O}$  labeled complex (blue lines) compared to the unlabeled complex (black lines) at three field positions I, II, and III marked at the top of panel A. The spectra represent the average of the left- and right-hand sides of the raw EDNMR spectrum.

**Table 1. Fitted Spin Hamiltonian Hyperfine Tensor Parameters for All Mn Model Systems; Comparison to BS-DFT**

		$^{17}\text{O}$ bridge hyperfine tensor $ A_i /\text{MHz}$								
		experiment							BS-DFT	
		$A_1$	$A_2$	$A_3$	$A_{\text{iso}}$	$D$	$\eta$	$A_{\text{iso}}(\text{av.})^a$	unique axis	
DTNE	$\text{Mn}^{\text{III}}-\mu(\text{O})_2-\text{Mn}^{\text{IV}}$	1	16.9	11.5	-12.5	+5.3	-8.9	0.3	+5.2	$z$
		2	16.2	2.9	9.0	+9.4	+3.4	0.9		$x$
BIPY	$\text{Mn}^{\text{III}}-\mu(\text{O})_2-\text{Mn}^{\text{IV}}$	1	17.1	13.5	-11.4	+6.4	-8.9	0.2	+8.2	$z$
		2	17.0	2.2	7.8	+9.0	+4.0	0.7		$x$
MnCat	$\text{Mn}^{\text{III}}-\mu(\text{O})_2-\text{Mn}^{\text{IV}}$		18.1	7.5	-10.0	+5.2	-7.6	0.7	+6.7 to +7.9 <sup>b</sup>	$z$
R2lox	$\text{Fe}^{\text{III}}-\mu(\text{OH})-\text{Mn}^{\text{III}}$		17.0	13.0	33.0	+21.0	+6.0	0.3	-21.6 <sup>c</sup>	$z$

<sup>a</sup>Average calculated value for the two oxygen bridges using the summation method, i.e., approach iii; see Table 2. <sup>b</sup>Average calculated value for the two oxygen bridges, dependent on assignment of  $\text{Mn}^{\text{IV}}$  site. <sup>c</sup>Projected using the averaging method.

quantum transitions are observed, centered at 10.4 and 20.8 MHz, respectively. The single quantum transitions are split by the hyperfine coupling ( $A \approx 10$  MHz), whereas the double quantum transitions are split by twice the hyperfine coupling. The  $^{14}\text{N}$  peaks are characteristically narrow with peak widths of  $\text{fwhm} = 3$  MHz, similar to that seen for the BIPY complex,<sup>29</sup> and represent the strongly coupled axial ligand which sits along the Jahn–Teller axis of the  $\text{Mn}^{\text{III}}$  ion.<sup>69</sup> The remaining equatorial  $^{14}\text{N}$  ligands of the  $\text{Mn}^{\text{III}}$  and all  $^{14}\text{N}$  ligands of the  $\text{Mn}^{\text{IV}}$  appear as a “matrix” line centered at the  $^{14}\text{N}$  Larmor frequency. The corresponding  $^{17}\text{O}$  labeled DTNE complex EDNMR data are shown in blue in Figure 4B. The  $^{17}\text{O}$  signal observed is significantly different from that of the background  $^{14}\text{N}$  signal. It is much broader and does not resolve any structure. The single quantum  $^{17}\text{O}$  transitions do not appear as a doublet centered about the Larmor frequency of  $^{17}\text{O}$  [ $\nu_n(^{17}\text{O}) = 19.4$  MHz,  $B_0 = 3.37$  T]. It instead is a broad envelope, where a two-peak structure is only observed for the EDNMR spectrum measured on the low field edge (Figure 4B, I). An apparent splitting is all but lost for the EDNMR spectrum, measured on the high field edge (Figure 4B, III), and the spectrum in the center represents an average of the two edge spectra (Figure 4B, II). While a discrete peak structure is absent for the  $^{17}\text{O}$  signal, the total width of the envelope still provides

a complete description of the  $^{17}\text{O}$  hyperfine tensor. Spin Hamiltonian simulations are shown in Supporting Information S6. However, as is often the case, there are two equally valid interpretations of this data set, which differ depending on the relative signs of the isotropic and anisotropic hyperfine terms. This is because the transitions strongly overlap such that only two hyperfine tensor components are observed in isolation. In the instance where  $A_{\text{iso}}$  and  $D$  take opposite signs,  $A_{\text{iso}}$  is small and the  $A_{\text{aniso}}$  tensor is approximately axial (Table 1). In contrast, if  $A_{\text{iso}}$  and  $D$  take the same sign,  $A_{\text{iso}}$  is instead large and  $A_{\text{aniso}}$  is highly rhombic. Furthermore, the two different tensor geometries assign the unique tensor axis differently. In the case of solution 1, the unique tensor axis is the smallest in absolute magnitude and coincides with  $g_z$ , whereas, in solution 2, it is instead largest in absolute magnitude and coincides with  $g_x$  (Table 1). The corresponding 2D-EDNMR surface for the BIPY complex was previously published in Rapatskiy et al.<sup>29</sup> The EDNMR data for both complexes are very similar in terms of the structure of the  $^{17}\text{O}$  signal profile and its dependence on the magnetic field. However, the BIPY complex is systematically broader by  $\sim 2$  MHz. Spin Hamiltonian simulations of the BIPY EDNMR data are also shown in Supporting Information S6, and all parameters are listed in Table 1. As above, two equally valid interpretations exist for this data set; it is of note

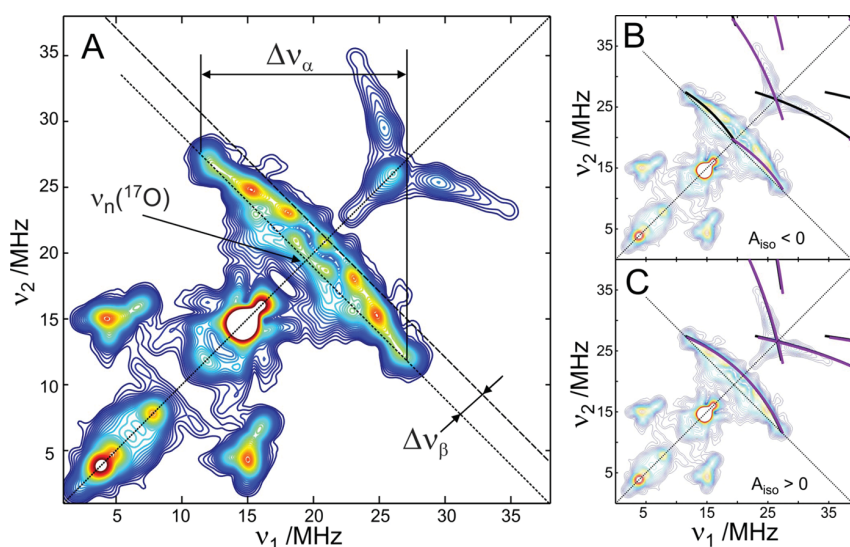


**Figure 5.** (A) W-Band  $^{17}\text{O}$ -HYSCORE of the  $\text{Mn}^{\text{III}}\text{Mn}^{\text{IV}}$  DTNE complex measured at the center field 3.372 T. The spectrum is an average of three  $\tau$  values (396, 408, and 420 ns) and is symmetrized about the diagonal. Raw data shown in Supporting Information S3. (B, C) Simulation showing the first and second  $^{17}\text{O}$  correlation ridges assuming an axial hyperfine tensor. In panels B and C,  $A_{\text{iso}}$  was fixed as either negative or positive, respectively, assuming a negative anisotropic/dipolar hyperfine term ( $A_{\text{aniso}}$  or  $D$ ).

that this was not identified in our original study. Solution 2 is approximately that given in Rapatskiy et al.<sup>29</sup>

**4.1.4. W-Band  $^{17}\text{O}$ -HYSCORE.** To address the remaining ambiguity in assigning the relative signs of the  $A_{\text{iso}}$  and  $D$  terms, we turned to ESEEM, namely, 2D-ESEEM techniques such as HYSCORE.<sup>70</sup> As compared to EDNMR, this technique has intrinsic advantages including enhanced line width resolution. Furthermore, HYSCORE transparently isolates the two anisotropic contributions to the spectral pattern, namely, the hyperfine anisotropy and quadrupole interaction. Hyperfine anisotropy broadens along the antidiagonal, whereas the quadrupole interaction broadens along the diagonal.<sup>26,32</sup> In this instance, however, it is the resolution of multiple correlation ridges that allows a definite assignment of the relative signs of the two hyperfine tensor components. Figure 5 shows HYSCORE data of the  $^{17}\text{O}$  labeled DTNE complex. In the unlabeled  $^{16}\text{O}$  DTNE sample, two discrete cross peaks were observed in the ++ frequency quadrant, centered about the Larmor frequency of  $^{14}\text{N}$  [ $\nu_{\text{n}}(^{14}\text{N}) = 10.4$  MHz,  $B_0 = 3.37$  T]. They both have a crescent structure with the maxima appearing at [5 15, 15 5] MHz. These cross peaks are consistent with a dominantly isotropic  $^{14}\text{N}$  hyperfine coupling of  $\sim 10$  MHz. In the corresponding  $^{17}\text{O}$  labeled DTNE complex, two new signals are observed: a structured correlation ridge centered about the Larmor frequency of  $^{17}\text{O}$  [ $\nu_{\text{n}}(^{17}\text{O}) = 19.4$  MHz,  $B_0 = 3.37$  T] and a second ridge which appears about 1.5 times the Larmor frequency (29.3 MHz). The latter ridge is distorted due to the limited microwave excitation bandwidth ( $\approx 30$  MHz). When measured at single  $\tau$  values, the first correlation ridge resolves approximately 6 peaks spaced by about 2 MHz (Supporting Information S3). These represent blind spot artifacts that are partially suppressed by averaging spectra at a series of  $\tau$  values. The spectrum shown in Figure 5A is an average of three  $\tau$  values (396, 408, and 420 ns). The two structured ridges observed for the  $^{17}\text{O}$  DTNE complex are derived from the single–single quantum transition and single–double quantum transition correlations within the  $^{17}\text{O}$  submanifold. As two correlation ridges are observed in the

HYSCORE spectrum, an estimate of both the  $A_{\text{iso}}$  and  $D$  terms can be made by inspection.  $D$  must clearly be large, as there is no separation of the first correlation ridge; for comparison, see the background  $^{14}\text{N}$  signal (Figure 5A). However,  $A_{\text{iso}}$  must also be large to account for the overlap of the second correlation ridge about the diagonal; although a large  $A_{\text{aniso}}$  (see eq 6) could also explain this overlap, in the instance where  $A_{\text{iso}}$  is zero, the corresponding first correlation ridge would be significantly too broad. Thus,  $A_{\text{iso}}$  and  $D$  must be of approximately the same size to reproduce the pattern. An explicit solution exists for the width and curvature of the first correlation ridge of a  $I = 1/2$  nucleus assuming an axial hyperfine tensor; see eqs 20 and 21. The total width of the ridge ( $\Delta\nu_{\alpha}$ ) represents the largest hyperfine tensor component, whereas the curvature is given by the ratio of the dipolar component to the nuclear Larmor frequency ( $\Delta\nu_{\beta}$ ).

$$\Delta\nu_{\alpha} = |A_{\text{iso}} + 2D| \quad (20)$$

$$\Delta\nu_{\beta} = \frac{9D^2}{32|\nu_{\text{n}}|} \quad (21)$$

Two solutions exist depending on the relative sign of the isotropic component ( $A_{\text{iso}}$ ) to the anisotropic/dipolar term ( $D$ ). However, calculated correlation maps shown in Figure 5B and C show that only the solution where  $A_{\text{iso}}$  is positive (assuming  $D$  is negative) is valid, as only this solution reproduces the curvature/diagonal crossing point of the first correlation ridge. Using this constraint, eqs 14 and 15 yield estimates for  $A_{\text{iso}} = 4$  MHz and  $D = -8.5$  MHz. These parameters are in good agreement with solution 1 simulation of the EDNMR data set. The HYSCORE data presented in Figure 5 however does not constrain the nonaxiality of the hyperfine tensor, and the inclusion of tensor rhombicity does influence estimates for the magnitude of  $A_{\text{iso}}$  and  $D$ . As shown in Supporting Information S4, a hyperfine rhombicity of  $\eta = 0.5$  is consistent with the structure of both correlation ridges. It is estimated that the inclusion of rhombicity leads to an uncertainty in  $A_{\text{iso}}$  and  $D$  values of  $\pm 1$  MHz. As a final

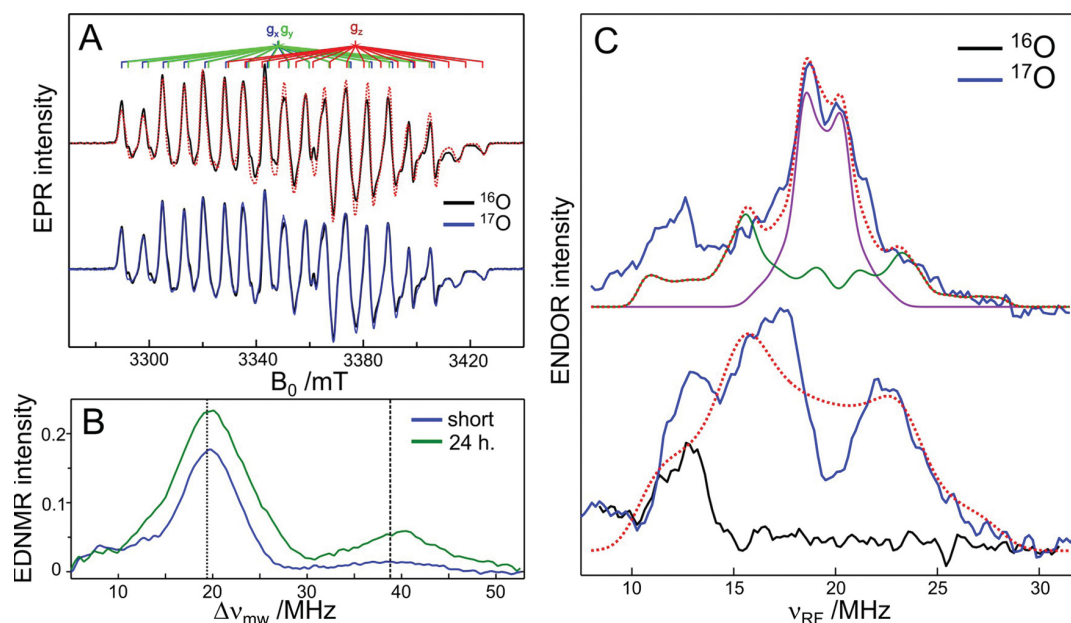


**Figure 6.** (A) W-band EPR spectra of **MnCat** suspended in  $^{17}\text{O}$  labeled water. (B) Corresponding  $^{17}\text{O}$ -EDNMR spectra for of the **MnCat** as a function of incubation time. (C) Corresponding  $\tau$ -averaged Mims and Davies  $^{17}\text{O}$  ENDOR measured at the center field after 24 h of incubation in  $\text{H}_2^{17}\text{O}$ . Back solid lines represent the unlabeled **MnCat**, and blue lines, the  $^{17}\text{O}$ -labeled **MnCat**. Red dashed lines represent a spin Hamiltonian simulation (see Table 1, Supporting Information S6). The different components of the simulation are shown by solid purple and green lines.

comment, it is noted that the structure of the first correlation ridge along the diagonal should provide an estimate of the quadrupole coupling. As no structure is observed, the quadrupole coupling must be small and is constrained by the line width, i.e.,  $|e^2qQ/hI| < 2$  MHz; see Supporting Information S4.

**4.1.5.  $^{17}\text{O}$ -EDNMR of the Mn Catalase, a  $\text{Mn}^{\text{III}}-(\mu\text{-O})_2\text{-Mn}^{\text{IV}}$  Complex.** X-ray structures exist for the manganese catalase (**MnCat**) enzyme isolated and purified from two organisms, *Lactobacillus plantarum*<sup>3</sup> and the species used in this study, *Thermus thermophilus*.<sup>5</sup> In both structures, each Mn ion has one terminal histidine and one glutamate ligand, which acts as a bidentate ligand for one Mn site and a monodentate ligand for the second Mn site, with the last coordination site filled by a water molecule. The two Mn ions are bridged by a  $\mu$ -carboxylato group of a glutamate and two oxygen bridges, one of which is derived from the substrate  $\text{H}_2\text{O}_2$ . During its catalytic cycle, the **MnCat** moves between two net oxidation states:  $\text{Mn}^{\text{II}}\text{Mn}^{\text{II}}$  and  $\text{Mn}^{\text{III}}\text{Mn}^{\text{III}}$ . In the  $\text{Mn}^{\text{III}}\text{Mn}^{\text{III}}$  state, the two oxygen bridges are assigned as a  $\mu$ -oxo/ $\mu$ -hydroxo linkage. It is possible to chemically oxidize the **MnCat** by one electron to generate the  $\text{Mn}^{\text{III}}\text{Mn}^{\text{IV}}$  oxidation state, termed the super-oxidized state. This state is EPR active ( $S_T = 1/2$ ), displaying a multiline EPR spectrum centered at  $g = 2$ , similar to the model complexes discussed above. Of the two, its structure is akin to the **DTNE** complex, with bis- $\mu$ -oxo,  $\mu$ -carboxylato linkage between the two Mn sites. It has been previously demonstrated that oxygen atoms of the bis- $\mu$ -oxo bridge(s) and terminal water ligand of the **MnCat** exchange with  $^{17}\text{O}$  labeled water. The rate of exchange of the terminal water ligand is rapid ( $< 5$  s),<sup>24</sup> whereas the exchange of the  $\mu$ -oxo bridge occurs much more slowly ( $\sim 2$  h at room temperature).<sup>24</sup> As the characterization of the oxo-bridge was the target of this study, we performed a relatively slow isotope exchange procedure.

The **MnCat** was resuspended five times in  $^{17}\text{O}$  labeled water at room temperature, with the total procedure taking in excess of an hour. To ensure complete exchange had occurred, samples were subsequently incubated for 24 h at room temperature.

Figure 6A shows a comparison of W-band EPR spectra recorded for the unlabeled and  $^{17}\text{O}$  labeled **MnCat**. Line broadening is more difficult to resolve as compared to the models, in part because the intrinsic EPR line width is broader; see also refs 23 and 24. The corresponding EDNMR spectrum resolves a broad envelope of  $\approx 10$  MHz. The shape of the signal is reminiscent of the  $^{17}\text{O}$  signal profile seen in PSII treated with ammonia. The envelope was measured as a function of the amplitude of the pump pulse (power dependence) to assess whether it represented one or two exchanged water ligands. At high pump amplitudes, the center of the pattern is enhanced, indicating the profile is made up of a narrow, more weakly coupled species and a broader, more strongly coupled species, similar to that seen for the model complexes described above. The former signal is instead assigned to the exchanged water ligand. As a further check, the EDNMR profile was measured for samples which did not receive a 24 h incubation in  $\text{H}_2^{17}\text{O}$  buffer. As expected, the narrow component of the EDNMR profile is enhanced in these samples (Figure 6B). The EDNMR profile measured is nominally consistent with the earlier Q-band ENDOR study of McConnell et al.;<sup>24</sup> see also section 4.1.8.

The putative exchangeable bridge signal, i.e., the broad envelope, was further characterized by measuring the complete 2D EDNMR surface. This data set is again very similar to that seen for the two model complex systems described above. A spin Hamiltonian simulation constrained such that the sign of  $A_{\text{iso}}$  is positive relative to the  $D$  value is consistent with this interpretation (Supporting Information S6). As a final step, both Mims and Davies W-band  $^{17}\text{O}$ -ENDOR were attempted

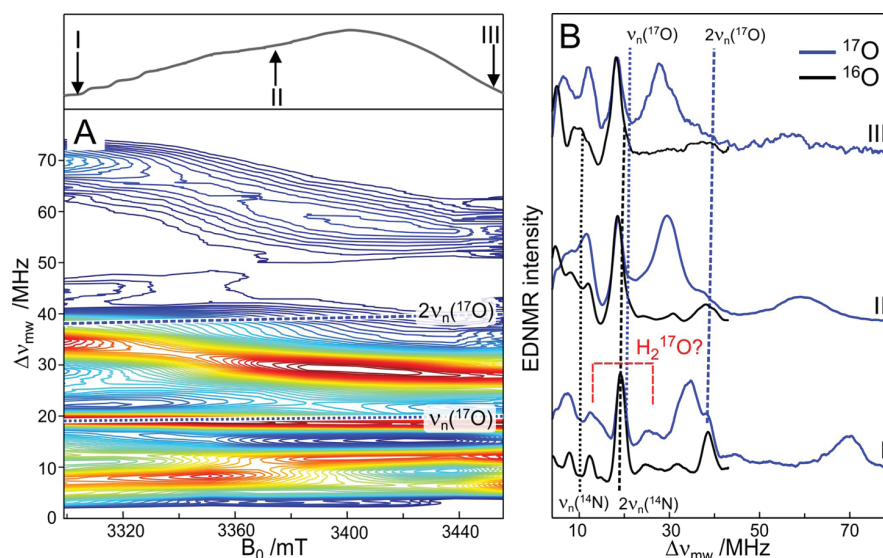


**Figure 7.** (A) 2D-EDNMR spectra of the  $^{17}\text{O}$  labeled **R2lox** cofactor. (B) Comparison of the EDNMR signal seen for the  $^{17}\text{O}$  labeled cofactor (blue lines) compared to unlabeled cofactor (black lines) at three field positions I, II, and III, marked at the top of the left panel.

to improve the resolution of the spectral profile (Figure 6C). The Davies ENDOR spectrum is of approximately the same width as the EDNMR envelope and thus is assigned to the exchanged bridge species; note the loss of signal intensity in the center of the profile is due to blind spotting, with the width of this central hole proportional to the inverse of the preparation/inversion pulse. In contrast, the  $\tau$ -averaged Mims ENDOR profile selectively picks out the narrow component of the EDNMR profile, assigned to the water ligand. In the ENDOR experiment, a splitting is resolved ( $\approx 1.5$  MHz), and the line shape, which appears to be Lorentzian, is better visualized. The Davies ENDOR spectrum can be fit using the same spin Hamiltonian parameters inferred for the exchanged  $\mu$ -oxo bridge signal. The same species also explains the wings of the Mims ENDOR profile, which extend to  $\pm 7$ – $8$  MHz. It cannot however explain the central component. No constrained fit can be achieved. However, if approximately the same parameters are assumed as for the water ligand of ferric heme iron,<sup>71</sup> a good fit of the data is obtained. The characteristic feature of this fit is the inclusion of a larger quadrupole coupling ( $Q = 8$  MHz,  $\eta = 1$ ), much larger than inferred for the  $\mu$ -oxo bridge, which gives the spectrum its characteristic Lorentzian line shape. A large quadrupole coupling has also been measured for  $^{17}\text{O}$  labeled water bound to  $\text{Gd}^{3+}$ .<sup>27</sup>

**4.1.6.  $^{17}\text{O}$ -EDNMR of the Mn/Fe Cofactor of R2lox, a Mn<sup>III</sup>-( $\mu$ -OH)-Fe<sup>III</sup> Complex.** Heterobimetallic Mn/Fe cofactors represent a new paradigm in enzymology.<sup>10</sup> One such example is the cofactor found in the small subunit (R2) of the ribonucleotide reductase class Ic (R2c).<sup>6,8,9</sup> It is activated by  $\text{O}_2$ , forming an oxygen-bridged cofactor which serves as an in situ  $1e^-$  oxidant, initiating the enzymatic reaction. We have recently characterized a homologue of the R2c cofactor, termed **R2lox**.<sup>9,72,73</sup> Although its precise biological function is not yet known, it is thought to catalyze oxidative chemistry, hence its name, R2-like ligand binding oxidase. Unlike R2c,<sup>74</sup> there exists a crystal structure of the  $\text{O}_2$ -activated heterobimetallic cofactor in a homogeneous state.<sup>9</sup> Each site has one terminal histidine ligand, and the two metals are bridged by the  $\mu$ -carboxylato group of one glutamate residue and one fatty acid ligand. The

ligand field of the Fe ion is completed by two monodentate glutamate residues, whereas the Mn ion has a monodentate glutamate and a water ligand, which sits along the Mn<sup>III</sup> Jahn–Teller axis. An oxygen from the  $\text{O}_2$  is subsumed into the complex as a  $\mu$ -hydroxo bridge; its protonation state was recently confirmed using Q-band  $^2\text{H}$ -HYSCORE.<sup>22</sup> As with the **MnCat**, the aim here is to characterize the oxygen bridge, i.e.,  $\mu$ -hydroxo.

As the  $\mu$ -OH bridge is much more labile than the  $\mu$ -oxo bridges of **MnCat**, complete labeling of the **R2lox** could be more easily achieved without long incubations in  $\text{H}_2^{17}\text{O}$ . Background EDNMR data for the **R2lox** cofactor resolve a  $^{14}\text{N}$  signal, previously characterized by W-band three pulse ESEEM.<sup>22</sup> The signal is obtained under cancellation conditions, i.e.,  $A = 2\nu_{\text{N}}$ , and as such, only the  $\nu^+$  line is observed ( $\nu^-$  appears at 0 MHz, inside the blind zone). Double quantum transitions are also observed for this species at  $\sim 34$  MHz. Spin Hamiltonian simulations of this data set (see Supporting Information S6), using published parameters, reproduce the 2D-EDNMR profile, and thus serve as a means to validate subsequent simulations of the  $^{17}\text{O}$  profile.

Upon  $^{17}\text{O}$  buffer exchange, two new signal envelopes are resolved in the EDNMR spectrum; see Figure 7. Unlike all earlier data, the hyperfine coupling is sufficiently large that a splitting (doublet structure) is observed. The two peaks are split by about 20 MHz, requiring that the isotropic hyperfine coupling of this species is large, and thus the bridge carries significant spin density. The same result was inferred from the large  $^1\text{H}/^2\text{H}$  hyperfine coupling assigned to the  $\mu$ -OH bridge, i.e.,  $A_{\text{iso}}(^1\text{H}) = 10$  MHz.<sup>22</sup> The signal also displays a strong field dependence demonstrating that the  $D$  term is also large, as seen for Mn/Mn dimer models discussed above. In contrast to the bridge, the water ligand is not readily observed. It is speculated though that the smaller splitting seen for the EDNMR spectrum measured on the low field edge ( $A \approx 10$  MHz) may represent this species. At the other two field positions, the bridge hyperfine strongly overlaps with this region, masking these transitions.

**4.1.7.  $\mu$ -oxo- $^{17}\text{O}$  Model Complex Data, Comparison to Literature.** The above sections demonstrate that the observed EPR line broadening seen upon  $^{17}\text{O}$  bridge labeling systematically overestimates the isotropic hyperfine coupling. The value determined using this methodology instead best matches the largest component of the  $^{17}\text{O}$  hyperfine tensor, i.e.,  $A_{\text{iso}} + 2D$ . Similarly, low field ENDOR does not provide a robust description of the  $^{17}\text{O}$  bridge hyperfine tensor for these systems. Owing to the small  $g$ -anisotropy and large  $^{55}\text{Mn}$  hyperfine, orientation selective measurements at low fields cannot be implemented. As such, ENDOR measurements at these frequencies, be it X- or Q-band, resolve only broad featureless spectra which are not readily interpretable. This explains why the earlier studies which sought to characterize the  $\mu$ -oxo bridges of Mn complexes<sup>23</sup> are at variance with the results presented here. In both Usov et al.<sup>23</sup> and McConnell et al.,<sup>24</sup> the approach that was taken was to attempt to match the  $^{17}\text{O}$  hyperfine coupling estimate from EPR line width broadening with that inferred from Q-band ENDOR. In both studies, a broad, structureless  $^{17}\text{O}$  ENDOR signal was observed centered at 13.5 MHz which could be interpreted to match the line-broadening estimate of  $A_{\text{iso}} \approx 13$  MHz. We suspect though that the ENDOR profile as measured in these earlier studies does not represent a true average coupling but instead emphasizes the largest component of the hyperfine tensor. A pictorial demonstration of how this could occur is shown in Figure 8. Due to nonlinearity of the  $B_2$  (RF) field, we suspect

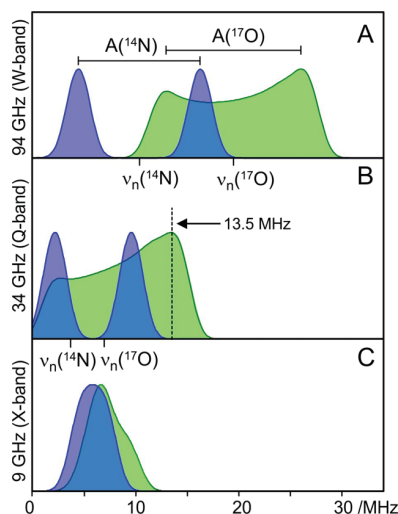


**Figure 8.** Pictorial representation of the  $^{17}\text{O}$  ( $\mu$ -oxo) and  $^{14}\text{N}$  (on the Jahn–Teller axis of the  $\text{Mn}^{\text{III}}$  ion) ENDOR signals seen for the BIPY complex at three microwave frequencies: (A) 94 GHz (W-band); (B) 34 GHz (Q-band); (C) 9 GHz (X-band).

that the Q-band signal envelope below 7 MHz, i.e., the  $\nu(^{17}\text{O})$  and  $\nu(^{14}\text{N})$  branches, is strongly suppressed. The only resolved component is a broad featureless line extending to 15 MHz (Figure 8B). Its interpretation is further hampered by the overlapping  $^{14}\text{N}$  signal which is suspected to coincide with one of the major turning points of the  $\nu(^{17}\text{O})$  signal branch. It can also be seen in Figure 8C that, at frequencies lower than Q-band (X-band), all spectral components strongly overlap, making any interpretation difficult.

**4.1.8. Experimental Summary—A Magnetic Fingerprint for an Oxygen Bridge.** From the measurements described

above, a magnetic fingerprint for the  $\mu$ -oxo bridge of Mn complexes can be developed. In these systems, the sign of the isotropic hyperfine (relative to  $D$ ) is positive, of magnitude 5–10 MHz. Terminal ligand hyperfine couplings ( $^{14}\text{N}$ , etc.) for  $\text{Mn}^{\text{III}}$  and  $\text{Mn}^{\text{IV}}$  model complexes typically fall in the range 2–4 MHz, with the exception of ligands along the Jahn–Teller axis of  $\text{Mn}^{\text{III}}$  which instead are approximately 12 MHz. Thus,  $\mu$ -oxo bridge hyperfine couplings fall between these two ranges, and can be termed intermediate. Interestingly, the magnitude of the anisotropic hyperfine is larger than that of the isotropic term. This is not the case for terminal ligands where the hyperfine anisotropy can usually be approximated in terms of the magnetic dipolar interaction between the ligand nucleus and the electron spin. The through space magnetic dipole estimate for the  $^{17}\text{O}$  bridge of the DTNE and BIPY complex is  $D \approx 4.5$  MHz, 2-fold smaller than that observed experimentally, i.e., 9 MHz (see Supporting Information S7). The experimental  $D$  value is, however, of approximately the same magnitude as that reported for the oxygen bridge of the  $\text{Fe}^{\text{III}}\text{Fe}^{\text{IV}}$  cofactor of class 1a ribonucleotide reductase, i.e.,  $D = 8$  MHz, and the relative signs of  $A_{\text{iso}}$  and  $D$  also match this previous study.<sup>12</sup> The only difference is in the magnitude of  $A_{\text{iso}}$ . For the di-Fe cofactor,  $A_{\text{iso}}$  is much larger ( $A = 15$  MHz) presumably because  $\text{Fe}^{\text{III/IV}}$  delocalizes its valence d-electrons across its ligands to a greater extent than Mn (see section 4.2.4).

The orientation of the bridge hyperfine tensor relative to the  $g$ -axis and its axial nature are also not consistent with a through space dipolar interaction explaining the hyperfine anisotropy. The unique  $g$ -tensor axis ( $g_z$ ), which for bis- $\mu$ -oxo Mn complexes is the smallest value, is typically perpendicular the plane defined by the  $\text{Mn}-(\mu\text{O})_2\text{-Mn}$  atoms, with  $g_x$  and  $g_y$  instead lying within the plane. This result can be readily understood. The octahedral  $\text{Mn}^{\text{IV}}$  ion of the spin system has a high spin  $d^3$  local electronic configuration. This electronic state is approximately spherically symmetric, leading to this ion exhibiting isotropic site spin Hamiltonian properties ( $g$ ,  $a$ , etc.). In contrast, the octahedral  $\text{Mn}^{\text{III}}$  ion of the spin system has a high spin  $d^4$  local electronic configuration. This electronic state is stabilized by a Jahn–Teller distortion, breaking the symmetry of the site. The distortion is typically along the ligand axis perpendicular to the  $\mu$ -oxo plane, and thus, this defines the unique  $g$  (and hyperfine) tensor axis of both the  $\text{Mn}^{\text{III}}$  ion itself and of the whole complex. As the unique  $g$ -tensor axis coincides with the Jahn–Teller axis of the  $\text{Mn}^{\text{III}}$  ion, it can be identified in the crystal for both the BIPY and DTNE complexes.<sup>17,68</sup> Consistent with this picture, the unique hyperfine axis of the nitrogen ligand (N1) coincides with  $g_z$ . In the MnCat and R2lox systems, the unique axis is expected to lie along the  $\text{Mn}-\text{OH}_2$  bond.

As described earlier,<sup>14,24,75</sup> the magnetic dipole tensor component of a bridging ligand consists of contributions from the hyperfine coupling of the ligand to each metal site, with the contribution of each weighted by the spin projection coefficient for each metal site.<sup>14,24,75</sup> The unique axis for the site hyperfine for each oxygen bridge should lie along the  $\text{Mn}-\text{O}$  bond. Assuming an  $\sim 90^\circ$   $\text{Mn}-\text{O}-\text{Mn}$  bond, summing the two site hyperfine tensors yields a projected  $^{17}\text{O}$  hyperfine tensor that has approximately rhombic symmetry ( $\eta = 0.6$ ). Its unique axis should lie in the plane that is defined by the  $\text{Mn}-\text{O}_2-\text{Mn}$  bridging motif with its middle component, in signed magnitude, perpendicular to the  $\text{Mn}-\text{O}_2-\text{Mn}$  plane. The exact opposite is seen for the experimental data, where the unique axis instead coincides with  $g_z$ , i.e., is perpendicular to the  $\text{Mn}-(\mu\text{O})_2-\text{Mn}$

Table 2. Calculated BS-DFT  $^{17}\text{O}$  Bridge Hyperfine Coupling Constants for Mn Model Complexes

		$^{17}\text{O}$ bridge hyperfine tensor/MHz									
		raw BS-DFT			site, $a_k$		average		projected		
		exp.	$a_k^{\text{BS}}$	% error	Mn <sup>III</sup>	Mn <sup>IV</sup>	$A_k$	% error	$A_k$	% error	
DTNE	1	+5.3	+6.1	+18.1	+1.5	-2.1	+2.6	-52	+5.1	-4	
	2		+6.3	+20.6	+1.6	-2.1	+2.6	-51	+5.2	-2	
BIPY	1	+6.4	+9.8	+53.8	+2.5	-3.3	+4.1	-36	+8.2	+28	
	2		+9.7	+52.2	+2.4	-3.3	+4.1	-37	+8.1	+27	
MnCat (A)	1	+5.2	+9.8	+88.5	+2.4	-3.3	+4.1	-21	+8.2	+58	
	2		+8.0	+53.8	+2.0	-2.7	+3.4	-40	+6.7	+29	
MnCat (B)	1		+8.8	+69.2	+2.2	-2.9	+3.7	-29	+7.3	+41	
	2		+7.4	+42.3	+2.2	-3.0	+3.1	-40	+7.5	+44	
PivO			-11.1		-2.2	-2.8	-4.4		-8.9		

plane. This observation suggests that, if indeed the net hyperfine coupling can be decomposed into two on-site interactions, the two site contributions are approximately equal and should be added without consideration of the sign of the local spin projections.

Interestingly, the principal axis orientation of the bridge hyperfine tensor appears consistent with the assignment seen for Fe<sup>III</sup>Fe<sup>IV</sup> cofactor of class 1a ribonucleotide reductase.<sup>12</sup> In this earlier study, it was observed that the unique hyperfine axis for the bridge coincides with the unique hyperfine axis of the terminal water ligand; the latter should sit orthogonal to the oxygen bridge plane.

**4.2. DFT Calculations.** The set of model complexes principally investigated in this study (see Figure 1) are all geometrically and electronically similar. Spin Hamiltonian parameters for the transition metal centers are provided in Supporting Information S8. Antiferromagnetic exchange-coupling between the two metal sites is facilitated by the overlap of a set of magnetic orbitals which reside largely on the metal centers and the p-orbitals of the  $\mu$ -oxo/hydroxo bridge(s) (Supporting Information S10).<sup>62,76</sup> As has been noted in the literature, the Mn<sup>III</sup> spin center has a large Jahn–Teller elongation along one axis which is orthogonal to the plane formed by the metal centers and the  $\mu$ -oxo or  $\mu$ -hydroxo bridge(s).<sup>64,76</sup> In terms of their bridging ligand motif, the set of complexes falls into four categories:

- bis- $\mu$ -oxo (BIPY)
- bis- $\mu$ -oxo,  $\mu$ -carboxylato (DTNE and Mn<sup>III</sup>Mn<sup>IV</sup> MnCat)
- $\mu$ -hydroxo, di- $\mu$ -carboxylato bridges (PivO, PivOH, and R2lox)
- mono/di- $\mu$ -hydroxo (Mn<sup>II</sup>Mn<sup>III</sup> MnCat)

The same complexes can equally be grouped into two isoelectronic sets: the set of Mn<sup>III</sup>Mn<sup>IV</sup> complexes (i, ii) and the set of Mn<sup>II</sup>Mn<sup>III</sup> complexes (iii, iv), including R2lox which is isoelectronic to Mn<sup>II</sup>Mn<sup>III</sup> being a Mn<sup>III</sup>Fe<sup>III</sup> complex. As will be shown below, neither of these groupings are appropriate for describing trends seen in the calculated bridge hyperfine coupling. Instead, it is the simpler criterion, namely, the protonation state of the bridge (oxo vs hydroxo), that is the principal factor in determining the magnitude of the calculated  $^{17}\text{O}$  hyperfine coupling (see Tables 1 and 2).

**4.2.1. BS-DFT Estimates for the Hyperfine Constant of  $\mu$ -Oxo Bridge(s) of Synthetic Model Complexes.** As described in the Theory section, there is no consensus methodology using BS-DFT for the calculation of ligand hyperfines which involve more than one spin carrying fragment (metal center). Here we examine three approaches, all of which should be considered as

largely empirical: (i) using the raw bridge hyperfine without correction; (ii) projecting the raw hyperfine for each spin fragment the bridge ligates and averaging the result; and (iii) projecting the raw hyperfine for each spin fragment the bridge ligates and summing the values. The results appear in Table 2. Before comparing the three methods, it should be noted that the raw calculated hyperfines are similar for all bis- $\mu$ -oxo bridged Mn dimers (6.1–9.8 MHz), suggesting that BS-DFT can be used to discriminate this type of species, even if the absolute value is uncertain.

The raw hyperfine though seems to systematically overestimate the measured hyperfine, in some cases by a factor of 2. In contrast, averaging the two projected hyperfine couplings systematically underestimates the measured hyperfine, by up to a factor of 2. The third method yields the best results, but this also has a tendency to overestimate the hyperfine coupling. Agreement between experiment and theory is particularly good for the DTNE complex, the best characterized of the set of three models, and poorest for the catalase, for which bridge estimates are less robust owing to the overlapping water ligand signal and the inequivalence and likely incomplete exchange of the two bridging oxygen atoms.

Good agreement for the summation method may, to some extent, be rationalized in the context of terminal ligand hyperfine estimates. For the set of Mn<sup>III</sup>Mn<sup>IV</sup> model complexes, it has been observed that the magnitude of the isotropic hyperfine coupling constants is significantly different for the set of first coordination sphere ligands. Ligand hyperfines broadly fall into three categories: (i) axial ligands of the Mn<sup>III</sup> ion which lie along the Jahn–Teller axis; (ii) the terminal equatorial ligand of the Mn<sup>III</sup> ion and all terminal ligands of the Mn<sup>IV</sup> ion; and (iii) bridging ligands, which represent equatorial ligands of both the Mn<sup>III</sup> and Mn<sup>IV</sup> ions. Category i has the largest hyperfine coupling constants, greater than 10 MHz, whereas category ii is 5–10 fold smaller. Such observations have been made both experimentally and computationally. As has been shown in the previous experimental sections, bridging hyperfine coupling constants (category iii) fall in between these two ranges. The simple projection method described in the Theory section readily rationalizes this result. As seen from eqs 7–19, the magnitude of the bridge hyperfine coupling constant is the weighed sum of the on-site hyperfine from each Mn. As such, it should be approximately twice that seen for corresponding terminal equatorial ligands, which only have one contribution. For example, for the BIPY model, the individual calculated on-site hyperfine couplings for the Mn<sup>III</sup> and Mn<sup>IV</sup> spin fragments are 4.8 and 3.2 MHz, respectively, yielding an overall coupling of 8.0 MHz. By way of comparison, the averaging method, by

Table 3. Calculated BS-DFT Hyperfine Coupling Constants for the R2lox and Related Model Systems

	<sup>17</sup> O hyperfine tensor/MHz							
	raw BS-DFT $a_k^{\text{BS}}$		site, $a_k$			projected, $A_k$		average, $A_k$
	H <sub>2</sub> O	bridge	H <sub>2</sub> O	bridge	H <sub>2</sub> O	H <sub>2</sub> O	bridge	
				Fe <sup>III</sup> (Mn <sup>II</sup> )	Mn <sup>III</sup>			
R2lox Mn-( $\mu$ OH)-Fe	42.9	-53.9	-10.7	-10.8	13.5	14.3	-43.2	-21.6
PivOH Mn/Fe		-58.5		-11.7	14.6		-46.8	-23.4
PivOH Mn/Mn		-34.8		-7.0	8.7		-27.8	-13.9
MnCat Mn/Mn II,III	-28.5	-24.5	-5.7	-4.9	6.1	-13.3	-19.6	-9.8
		-34.8		-7.0	8.7		-27.9	-13.9
MnCat Mn/Mn III,II	28.9	-24.7	-7.2	-5.0	6.2	9.6	-19.8	-9.9
		-38.0		-7.6	9.5		-22.3	-15.2

design, will yield a bridge estimate that is of the same magnitude as for a terminal ligand, i.e., 4 MHz. Additionally, it is important to note that the hyperfine coupling constants for <sup>17</sup>O ligands should be approximately 2 fold larger than those calculated for the <sup>14</sup>N ligands, as the Fermi contact term scales with the nuclear  $g$ -value (eq 22)

$$a_{\text{iso}} = \frac{4\pi}{3} \frac{g g_n \beta \beta_n}{\langle S_z \rangle} \rho(\vec{R}_n) \quad (22)$$

where  $g$ ,  $g_n$ ,  $\beta$ , and  $\beta_n$  are as defined in the Theory section and  $\rho$  is the spin density at the nucleus. The ratio of  $g_n$  for <sup>17</sup>O and <sup>14</sup>N is -1.88. Thus, as a back of the envelope calculation, assuming an equivalent spin population for a bridging <sup>14</sup>N in place of the  $\mu$ -oxo bridge, the expected contributions from Mn<sup>III</sup> and Mn<sup>IV</sup> would be -2.5 and -1.7 MHz. Both values are within the range seen for terminal equatorial nitrogen ligands coordinated to Mn<sup>III</sup> or Mn<sup>IV</sup> spin centers.<sup>62</sup>

The influence of the implicit solvation (COSMO) dielectric constant was also tested. Calculations on a DTNE Mn<sup>III</sup>Mn<sup>IV</sup> complex without methyl groups on the DTNE ligand were completed with varying values of the dielectric constant ranging from zero to 80. Additionally, a completely conductive solvent was also tested ( $\epsilon = \infty$ ). The calculated results indicate that there is a small, less than 0.5 MHz change, with respect to the implicit solvent model chosen (see Supporting Information S9). These results imply that the choice of a dielectric constant will only minimally impact the results of protein cluster models. The effect of explicit solvation is beyond the scope of this work.

**4.2.2. BS-DFT Estimates for the Hyperfine Constant of  $\mu$ -Oxo Bridges and the Water Ligand of MnCat Poised in the Superoxidized State.** The same good agreement is seen for the summation method for the superoxidized state of the MnCat. For this system, there is some ambiguity however with regard to assignment of local oxidation states to +III or +IV. Both options were tested, termed here catalase model A and catalase model B. The key difference between the two models is whether the H<sub>2</sub>O ligand is coordinated to the Mn<sup>III</sup> (model A) or Mn<sup>IV</sup> (model B). As can be seen in Table 2, the calculated values for the superoxidized state of MnCat fall within the same range as those of the model complexes DTNE and BIPY. Interestingly, but perhaps not surprisingly, the two different models do not allow for the absolute oxidation states of the Mn centers to be determined.

The assignment of the Mn oxidation states is far more important when considering the estimate for the <sup>17</sup>O hyperfine of the H<sub>2</sub>O ligand. <sup>1</sup>H-ENDOR resolves large hyperfine coupling for exchangeable hydrogens  $\approx$ 17 MHz. Such couplings have been interpreted in terms of the water ligand

being associated with the Mn ion that carries majority spin ( $\rho = 2$ ), i.e., the Mn<sup>III</sup> ion, and subsequent inhibition studies support this assignment. Similarly, a theoretical study of Sinnecker et al.<sup>77</sup> supported the Mn<sup>III</sup> being the 5-coordinate Mn with its open coordination site filled with water. If this is the case, though, comparison to the model complexes above would suggest that the water ligand is the axial ligand of the Mn<sup>III</sup> ion on the Jahn–Teller axis. Calculations of the <sup>17</sup>O hyperfine of this terminal water ligand place it at about -20.5 vs +1.5 MHz for models catalase A and catalase B, respectively. Notably, the calculated hyperfine for the water occupying the axial position is significantly larger than results reported here and for the aforementioned proton/<sup>17</sup>O ENDOR study. As such, the experimental results and interpretation do not agree with the calculated values, a discrepancy which is still undergoing investigation.

**4.2.3. The Bis- $\mu$ -oxo vs Mono- $\mu$ -oxo Bridging Motif.** Lower valence Mn complexes have a tendency to stabilize the mono- $\mu$ -oxo bridge motif instead of a bis- $\mu$ -oxo motif.<sup>78</sup> Although measurements were attempted for these systems, the more liable nature of the Mn<sup>II</sup> ion in aqueous solution led to complex decomposition during labeling. Nevertheless, these systems could be examined *in silico*. Table 2 lists calculated ligand hyperfine coupling for the Mn<sup>II</sup>/Mn<sup>III</sup> PivO. Terminal nitrogen hyperfine coupling for these complexes fall into the same two classes described above for Mn<sup>III</sup>/Mn<sup>IV</sup> complexes. Interestingly, the calculated bridge hyperfine for the mono- $\mu$ -oxo bridge is within the range seen for the higher valence Mn<sup>III</sup>/Mn<sup>IV</sup> bis- $\mu$ -oxo bridge complexes. This is somewhat unexpected but not truly surprising, as the exchange pathway between the two Mn ions is qualitatively similar to those of the bis- $\mu$ -oxo complexes, comprised mostly of combinations of ligand p-orbitals along with metal d-orbitals (Supporting Information S10). Thus, the general rule of thumb outlined above appears to be robust toward the precise structure of the bridge with the bridge hyperfine being approximately 2-fold larger than a terminal nitrogen ligand (accounting for the nuclear  $g$ -value), and smaller than that seen for ligands along the Jahn–Teller axis of the Mn<sup>III</sup> ion.

**4.2.4. The Effect of Protonation of the Bridge.** Although not experimentally accessible for the same reasons as the Mn<sup>II</sup>Mn<sup>III</sup> PivO complex, BS-DFT calculations were performed on the mono- $\mu$ -hydroxo bridged PivOH complex. Here, unlike the complexes presented previously, the  $\mu$ -hydroxo bridge has a much larger (27 vs 9 MHz) calculated hyperfine coupling constant upon the protonation of the  $\mu$ -oxo bridge. This result is somewhat counterintuitive, as the protonation of the bridge should result in a lowered covalency of the Mn–oxo bond.

However, protonation of the  $\mu$ -oxo bridge simultaneously leads to an increase in s-character of the Mn–oxo bonds (Supporting Information S10), resulting in a larger core spin polarization which in turn leads to larger isotropic hyperfine values (via the Fermi contact term). Interestingly the Mulliken spin populations show the expected intuitive trend with spin populations of  $-0.10$  and  $-0.02$  for the oxygen atoms of the  $\mu$ -oxo and  $\mu$ -hydroxo bridges, respectively. It should be noted, however, that such a spin population analysis for either ligand has been shown to not correlate with the actual calculated isotropic hyperfine couplings, which is only representative of the core spin polarization (eq 22), and not the total unpaired spin density of the EPR active nuclei.<sup>79</sup> Similar results are seen in the bis- $\mu$ -hydroxo bridged  $\text{Mn}^{\text{II}}\text{Mn}^{\text{III}}$  catalase models which further support the notion that the bridge hyperfine coupling should increase upon bridge protonation, specifically that the experimental hyperfine of  $\mu$ -hydroxo bridges should be approximately 2 fold larger; note this estimate takes into account the expected overestimation of the calculated hyperfine couplings (see Table 2).

**4.2.5. BS-DFT Estimates for the Hyperfine Constant of the  $\mu$ -Hydroxo Bridge and Water Ligand of R2lox.** Calculated hyperfine coupling constants for the cluster model of R2lox are presented in Table 3. R2lox itself presents an interesting deviation from the other model systems studied in that it represents a heterometallic complex with a  $\mu$ -hydroxo bridge. As stated above, it can be considered structurally and electronically similar to the  $\text{Mn}^{\text{II}}\text{Mn}^{\text{III}}$  PivOH complex, as  $\text{Fe}^{\text{III}}$  is isoelectronic to  $\text{Mn}^{\text{II}}$ , the two metals are bridged by a  $\mu$ -hydroxo ligand, and the two metal ions couple together antiferromagnetically to give a ground state spin of  $S = 1/2$ . As per the last section, the expectation is that the theoretical  $^{17}\text{O}$  hyperfine would be approximately the same as calculated for the PivOH complex ( $\approx 20$  MHz), which would be consistent with the experimental R2lox data. This, however, is not the case. As can be readily seen from Table 3, the calculated results are approximately 2 fold larger using the summation method. Here it seems instead that the averaging model<sup>66</sup> is more appropriate, reproducing the experimental result, i.e., 21 MHz. The same good agreement using the averaging method was seen previously by Noodleman and co-workers of the di-Fe cofactor of ribonucleotide reductase.<sup>66</sup> It can be further shown that this effect is solely a consequence of the R2lox cofactor containing an Fe ion. Calculations performed on the hypothetical  $\text{Mn}^{\text{III}}\text{Fe}^{\text{III}}$  PivOH complex where the  $\text{Mn}^{\text{II}}$  was replaced with  $\text{Fe}^{\text{III}}$  yield essentially the same 2-fold increase in the estimated bridge hyperfine coupling as compared to the di-Mn homologue. This significant difference indicates that the  $\text{Fe}^{\text{III}}$  ion plays a different role from that of the  $\text{Mn}^{\text{II}}$  ion in the distribution of spin across the molecule. A difference of one unit of nuclear charge for the Fe vs Mn counterintuitively results in Fe complexes having more delocalized unpaired d-shell electrons, leading to more spin polarization on the ligands coordinated to the Fe metal center. Mn, on the other hand, has much more localized d-shell electrons, as can be seen in a comparison of Mn vs Fe Mulliken or Löwdin spin populations. Consequently, this means that the larger calculated bridge hyperfine coupling values seen in complexes that contain a  $\text{Fe}^{\text{III}}$  metal center can be rationalized as indicating that a significantly larger portion of the spin polarization located on the  $\mu$ -hydroxo bridging ligand is derived from electronic overlap with the orbitals of the  $\text{Fe}^{\text{III}}$  ion rather than the  $\text{Mn}^{\text{III}}$  ion. Thus, the fundamental assumption presented in the Theory section,

namely, that the bridging ligand is “shared” by both spin sites, is not met for such complexes, and therefore, the summation method fails. Clearly, we are not at the point where BS-DFT can provide confident predictions for bridging hyperfine coupling constants for an arbitrary system, and indeed, it may be necessary to move beyond BS-DFT to develop a fully consistent methodology.

## 5. CONCLUSIONS AND OUTLOOK

The above study demonstrates that oxygen bridges of Mn complexes can be described in depth using multifrequency, multiresonance EPR techniques. Interestingly, the experimental isotropic hyperfine coupling seen between different complexes, +5.3 MHz (DTNE), +6.4 MHz (BIPY), and +5.2 MHz (MnCat), is approximately invariant. The insensitivity of the isotropic hyperfine coupling to the exact geometry of the bridging unit, the ligand scaffold, and the polarity of the local environment (solvent vs protein) suggests that its magnitude can be used as a robust marker for this bridging type. This result is extended by DFT calculations which show a similar invariance in the  $^{17}\text{O}$  bridge hyperfine coupling value within the tolerance typically achieved for ligand hyperfine couplings. It also holds for complexes of different net Mn oxidation state, or for complexes that contain either a single or bis- $\mu$ -oxo bridging network. The only parameter that significantly changed the observed hyperfine coupling was protonation of the bridge, leading to a 2-fold increase. As stated above, this observation is counterintuitive. As bridge protonation should lead to a decrease in covalency of the bridging oxygen, the hyperfine coupling should instead decrease. It is hypothesized that this effect is due to interplay between the spin density, which is predominantly associated with the p-orbitals of the bridging oxygen, and the spin polarization as described above.

This  $\mu$ -oxo vs  $\mu$ -hydroxo fingerprint will serve as benchmarks for expanded catalytic studies on metallocofactors. From the perspective of studying the catalysis of such Mn metallocofactors, the protonation state of the bridge is of critical importance. While the metal oxidation state, etc., can be assessed by measuring the metal hyperfine, the net bridge protonation state of the bridging network can be ambiguous. An example would be if the complex contains both a deprotonated  $\mu$ -oxo bridge and a singly protonated  $\mu$ -hydroxo bridge. As demonstrated here,  $^{17}\text{O}$  labeling of this hypothetical complex should provide a marker for each oxygen bridge type, allowing the connectivity of the complex to be experimentally constrained. The Mn/Mn cofactor found in the ribonucleotide reductase enzyme class 1b is one such example<sup>7,80</sup> which could be studied using this approach.

Of particular interest is the characterization of reaction intermediates.<sup>81</sup> Several metal cofactors activate small molecules via  $\mu$ -oxo bridge assembly. The precise fate of such reactants can thus be tracked using the methods described above. One such example is nature's water oxidizing complex, a tetramanganese–calcium cofactor, found in photosystem II. Our recent work has shown that the cofactor contains a fast exchanging oxo bridge midway through its catalytic cycle. This bridge is considered the most likely candidate for the first substrate water bound during catalysis. The identity of the exchangeable bridge has previously been assigned to O5, the oxo bridge between Mn3 and Mn4.

This assignment was based on site perturbation: addition of  $\text{NH}_3$ , which displaces a terminal water ligand of the cofactor (W1), was seen to strongly perturb the exchangeable bridge's

hyperfine coupling (30% decrease). This change has been rationalized by a *trans* effect; the oxo bridge *trans* to W1 is O5. BS-DFT calculations quantitatively supported this assignment. While projected hyperfine couplings were not available at the time, it could be shown that calculated raw hyperfine coupling of the  $\mu$ -oxo bridge O5 is sensitive to NH<sub>3</sub> binding, owing to an elongation of the Mn–O5 bond. The BS-DFT calculations presented here suggest that the use of the summation method may be appropriate for this system to calculate the true hyperfine coupling. Indeed, taking raw hyperfine coupling constants from our previous study<sup>33</sup> and using the summation method yields estimates within 30% of experiment. The calculation of such bridging hyperfine couplings and the detection of bound substrate sites in all catalytic states of the WOC cofactor forms ongoing work of our laboratory.

## ■ ASSOCIATED CONTENT

### ■ Supporting Information

The Supporting Information is available free of charge on the ACS Publications website at DOI: 10.1021/acs.jpcc.5b04614.

(S1) <sup>17</sup>O/<sup>18</sup>O labeling of synthetic complexes as monitored by mass spectrometry; (S2) multifrequency CW and pulse EPR spectra of the BIPY complex; (S3) raw HYSORE data of the DTNE complex; (S4) additional spin Hamiltonian simulations of the W-band HYSORE data collected for the DTNE complex; (S5) additional EDNMR data of the MnCat; (S6) spin Hamiltonian simulations of the DTNE, BIPY, MnCat, and R2lox 2D-EDNMR data; (S7) tabulated magnetic-dipole coupling for all structural models; (S8) additional DFT calculated parameters for models studied; (S9) effect of dielectric constant used in calculations; (S10) magnetic unrestricted corresponding orbitals (UCO) for the PivO, PivOH, and Mn<sup>III</sup>Fe<sup>III</sup> PivOH model complexes; (S11) references; (S12) tabulated *xyz* coordinates for all structural models (PDF)

## ■ AUTHOR INFORMATION

### Corresponding Author

\*E-mail: nicholas.cox@cec.mpg.de.

### Present Addresses

<sup>§</sup>Department of Chemistry, Juniata College, Huntingdon, Pennsylvania 16652.

<sup>||</sup>Department of Chemistry and Biochemistry, Ohio State University, Columbus, Ohio 43210.

### Author Contributions

The manuscript was written through contributions of all authors. All authors have given approval to the final version of the manuscript.

### Notes

The authors declare no competing financial interest.

## ■ ACKNOWLEDGMENTS

Prof. S. Antonyuk (University of Liverpool) and V. Barynin (University of Sheffield) are acknowledged for the gift of the manganese catalase samples. This work is supported by the Cluster of Excellence RESOLV (EXC 1069) funded by the Deutsche Forschungsgemeinschaft, the Max-Planck-Gesellschaft, the Swedish Research Council, the Swedish Foundation for Strategic Research, the Knut and Alice Wallenberg Foundation, and the Alexander von Humboldt Foundation.

## ■ ABBREVIATIONS

EPR, electron paramagnetic resonance; ENDOR, electron nuclear double resonance; ELDOR, electron–electron double resonance; NMR, nuclear magnetic resonance; EDNMR, ELDOR detected NMR; SQ, single quantum; DQ, double quantum

## ■ REFERENCES

- (1) Cox, N.; Pantazis, D. A.; Neese, F.; Lubitz, W. Biological water oxidation. *Acc. Chem. Res.* **2013**, *46*, 1588.
- (2) Umena, Y.; Kawakami, K.; Shen, J.-R.; Kamiya, N. Crystal structure of oxygen-evolving photosystem II at a resolution of 1.9 Å. *Nature* **2011**, *473*, 55.
- (3) Barynin, V. V.; Whittaker, M. M.; Antonyuk, S. V.; Lamzin, S. V.; Harrison, P. M.; Artymiuik, A. J.; Whittaker, J. M. Crystal Structure of Manganese Catalase from *Lactobacillus plantarum*. *Structure* **2001**, *9*, 725.
- (4) Dismukes, G. C. Manganese Enzymes with Binuclear Active Sites. *Chem. Rev.* **1996**, *96*, 2909.
- (5) Antonyuk, S. V.; Melik-Adamyanyan, V. R.; Popov, A. N.; Lamzin, V. S.; Hempstead, P. D.; Harrison, P. M.; Artymyuk, P. J.; Barynin, V. V. Three-dimensional structure of the enzyme dimanganese catalase from *Thermus Thermophilus* at 1 Å resolution. *Crystallogr. Rep.* **2000**, *45*, 105.
- (6) Cotruvo, J. A.; Stubbe, J. An Active Dimanganese(III)-Tyrosyl Radical Cofactor in *Escherichia coli* Class Ib Ribonucleotide Reductase. *Biochemistry* **2010**, *49*, 1297.
- (7) Cox, N.; Ogata, H.; Stolle, P.; Reijerse, E.; Auling, G.; Lubitz, W. A Tyrosyl Dimanganese Coupled Spin System is the Native Metalloradical Cofactor of the R2F Subunit of the Ribonucleotide Reductase of *Corynebacterium ammoniagenes*. *J. Am. Chem. Soc.* **2010**, *132*, 11197.
- (8) Jiang, W.; Yun, D.; Saleh, L.; Barr, E. W.; Xing, G.; Hoffart, L. M.; Maslak, M.-A.; Krebs, C.; Bollinger, J. M., Jr. A Manganese(IV)/Iron(III) Cofactor in *Chlamydia trachomatis* Ribonucleotide Reductase. *Science* **2007**, *316*, 1188.
- (9) Griese, J. J.; et al. Direct observation of structurally encoded metal discrimination and ether bond formation in a heterodinuclear metalloprotein. *Proc. Natl. Acad. Sci. U. S. A.* **2013**, *110*, 17189.
- (10) Schenk, G.; Boutchard, C. L.; Carrington, L. E.; Noble, C. J.; Moubaraki, B.; Murray, K. S.; de Jersey, J.; Hanson, G. R.; Hamilton, S. A Purple Acid Phosphatase from Sweet Potato Contains an Antiferromagnetically Coupled Binuclear Fe–Mn Center. *J. Biol. Chem.* **2001**, *276*, 19084.
- (11) Carepo, M.; Tierney, D. L.; Brondino, C. D.; Yang, T. C.; Pamplona, A.; Telsler, J.; Moura, I.; Moura, J. J. G.; Hoffman, B. M. <sup>17</sup>O ENDOR Detection of a Solvent-Derived Ni(OH<sub>x</sub>)Fe Bridge That Is Lost upon Activation of the Hydrogenase from *Desulfovibrio gigas*. *J. Am. Chem. Soc.* **2002**, *124*, 281.
- (12) Burdi, D.; Willems, J.-P.; Riggs-Gelasco, P.; Antholine, W. E.; Stubbe, J.; Hoffman, B. M. The Core Structure of X Generated in the Assembly of the Diiron Cluster of Ribonucleotide Reductase: <sup>17</sup>O<sub>2</sub> and H<sub>2</sub><sup>17</sup>O ENDOR. *J. Am. Chem. Soc.* **1998**, *120*, 12910.
- (13) Cooper, S. R.; Dismukes, G. C.; Klein, M. P.; Calvin, M. Mixed valence interactions in Di- $\mu$ -oxo bridged manganese complexes. Electron paramagnetic resonance and magnetic susceptibility studies. *J. Am. Chem. Soc.* **1978**, *100*, 7248.
- (14) Randall, D. W.; Sturgeon, B. E.; Ball, J. A.; Lorigan, G. A.; Chan, M. K.; Klein, M. P.; Armstrong, W. H.; Britt, R. D. <sup>55</sup>Mn ESE-ENDOR of a Mixed Valence Mn(III)Mn(IV) Complex: Comparison with the Mn Cluster of the Photosynthetic Oxygen-Evolving Complex. *J. Am. Chem. Soc.* **1995**, *117*, 11780.
- (15) Schäfer, K. O.; Bittl, R.; Lendzian, F.; Barynin, V. V.; Weyhermüller, T.; Wieghardt, K.; Lubitz, W. Multifrequency EPR Investigation of Dimanganese Catalase and Related Mn(III)Mn(IV) Complexes. *J. Phys. Chem. B* **2003**, *107*, 1242.
- (16) Schäfer, K. O.; Bittl, R.; Zweggart, W.; Lendzian, F.; Haselhorst, G.; Weyhermüller, T.; Wieghardt, K.; Lubitz, W. Electronic structure

- of antiferromagnetically coupled dinuclear manganese ( $\text{Mn}^{\text{III}}\text{Mn}^{\text{IV}}$ ) complexes studied by magnetic resonance techniques. *J. Am. Chem. Soc.* **1998**, *120*, 13104.
- (17) Weyhermüller, T. Synthese und Charakterisierung oxo-verbrückter Mangankomplexe mit Azamakrozyklen. Modelle für das Photosystem II; Ruhr Universität, 1994.
- (18) Plaksin, P. M.; Stoufer, R. C.; Mathew, M.; Palenik, G. J. Novel antiferromagnetic oxo-bridged manganese complex. *J. Am. Chem. Soc.* **1972**, *94*, 2121.
- (19) Cooper, S. R.; Calvin, M. Mixed valence interactions in Di- $\mu$ -oxo bridged manganese complexes. *J. Am. Chem. Soc.* **1977**, *99*, 6623.
- (20) Jensen, A. F.; Su, Z.; Hansen, N. K.; Larsen, F. K. X-Ray Diffraction Study of the Correlation between Electrostatic Potential and K-Absorption Edge Energy in a Bis( $\mu$ -oxo) Mn(III)-Mn(IV) Dimer. *Inorg. Chem.* **1995**, *34*, 4244.
- (21) Bossek, U.; Hummel, H.; Weyhermüller, T.; Wieghardt, K.; Russell, S.; van der Wolf, L.; Kolb, U. The  $[\text{Mn}_2^{\text{IV}}(\mu\text{-O}(\mu\text{-PhBO}_2)_2)]^{2+}$  Unit: A Structural Model for Manganese-Containing Metalloproteins. *Angew. Chemie, Int. Ed. Engl.* **1996**, *35*, 1552.
- (22) Shafaat, H. S.; et al. Electronic Structural Flexibility of Heterobimetallic Mn/Fe Cofactors: R2lox and R2c Proteins. *J. Am. Chem. Soc.* **2014**, *136*, 13399.
- (23) Usov, O. M.; Grigoryants, V. M.; Tagore, R.; Brudvig, G. W.; Scholes, C. P. Hyperfine Coupling to the Bridging  $^{17}\text{O}$  in the Di- $\mu$ -oxo Core of a  $\text{Mn}^{\text{III}}\text{Mn}^{\text{IV}}$  Model Significant to the Core Electronic Structure of the  $\text{O}_2$ -Evolving Complex in Photosystem II. *J. Am. Chem. Soc.* **2007**, *129*, 11886.
- (24) McConnell, I. L.; Grigoryants, V. M.; Scholes, C. P.; Myers, W. K.; Chen, P.-Y.; Whittaker, J. W.; Brudvig, G. W. EPR-ENDOR Characterization of ( $^{17}\text{O}$ ,  $^1\text{H}$ ,  $^2\text{H}$ ) Water in Manganese Catalase and Its Relevance to the Oxygen-Evolving Complex of Photosystem II. *J. Am. Chem. Soc.* **2012**, *134*, 1504.
- (25) Baute, D.; Goldfarb, D. The  $^{17}\text{O}$  Hyperfine Interaction in  $\text{V}^{17}\text{O}(\text{H}_2^{17}\text{O})_5^{2+}$  and  $\text{Mn}(\text{H}_2^{17}\text{O})_6^{2+}$  Determined by High Field ENDOR Aided by DFT Calculations. *J. Phys. Chem. A* **2005**, *109*, 7865.
- (26) Goldfarb, D.; Lipkin, Y.; Potapov, A.; Gorodetsky, Y.; Epel, B.; Raitsimring, A. M.; Radoul, M.; Kaminker, I. HYSCORE and DEER with an upgraded 95 GHz pulse EPR spectrometer. *J. Magn. Reson.* **2008**, *194*, 8.
- (27) Raitsimring, A. M.; Astashkin, A. V.; Baute, D.; Goldfarb, D.; Caravan, P. W-Band  $^{17}\text{O}$  Pulsed Electron Nuclear Double Resonance Study of Gadolinium Complexes with Water. *J. Phys. Chem. A* **2004**, *108*, 7318.
- (28) Cox, N.; Lubitz, W.; Savitsky, A. W-band ELDOR-detected NMR (EDNMR) spectroscopy as a versatile technique for the characterisation of transition metal-ligand interactions. *Mol. Phys.* **2013**, *111*, 2788.
- (29) Rapatskiy, L.; et al. Detection of the Water Binding Sites of the Oxygen-evolving Complex of Photosystem II Using W-band  $^{17}\text{O}$  ELDOR-detected NMR Spectroscopy. *J. Am. Chem. Soc.* **2012**, *134*, 16619.
- (30) Astashkin, A. V.; Feng, Raitsimring, A. M.; Enemark, J. H.  $^{17}\text{O}$  ESEEM Evidence for Exchange of the Axial Oxo Ligand in the Molybdenum Center of the High pH Form of Sulfite Oxidase. *J. Am. Chem. Soc.* **2005**, *127*, 502.
- (31) Schosseler, P.; Wacker, T.; Schweiger, A. Pulsed ELDOR detected NMR. *Chem. Phys. Lett.* **1994**, *224*, 319.
- (32) Schweiger, A.; Jeschke, G. *Principles of Pulsed Electron Paramagnetic Resonance*; Oxford University Press: Oxford, U.K., 2001.
- (33) Pérez Navarro, M.; et al. Ammonia binding to the oxygen-evolving complex of photosystem II identifies the solvent-exchangeable bridge ( $\mu$ -oxo) of the manganese tetramer. *Proc. Natl. Acad. Sci. U. S. A.* **2013**, *110*, 15561.
- (34) Barynin, V. V.; Grebenko, A. I. *Dokl. Akad. Nauk SSSR* **1986**, *286*, 461.
- (35) Khangulov, S. V.; Barynin, V. V.; Voevodskaya, N. V.; Grebenko, A. I. ESR spectroscopy of the binuclear cluster of manganese ions in the active center of Mn-catalase from *Thermus thermophilus*. *Biochim. Biophys. Acta, Bioenerg.* **1990**, *1020*, 305.
- (36) Reijerse, E.; Lendzian, F.; Isaacson, R.; Lubitz, W. A tunable general purpose Q-band resonator for CW and pulse EPR/ENDOR experiments with large sample access and optical excitation. *J. Magn. Reson.* **2012**, *214*, 237.
- (37) Epel, B.; Gromov, I.; Stoll, S.; Schweiger, A.; Goldfarb, D. Spectrometer manager: A versatile control software for pulse EPR spectrometers. *Concepts Magn. Reson., Part B* **2005**, *26B*, 36.
- (38) Stoll, S.; Schweiger, A. EasySpin, a comprehensive software package for spectral simulation and analysis in EPR. *J. Magn. Reson.* **2006**, *178*, 42.
- (39) Stoll, S.; Britt, R. D. General and efficient simulation of pulse EPR spectra. *Phys. Chem. Chem. Phys.* **2009**, *11*, 6614.
- (40) Becke, A. D. *Phys. Rev. A: At, Mol., Opt. Phys.* **1988**, *38*, 3098.
- (41) Lee, C.; Yang, W.; Parr, R. G. *Phys. Rev. B: Condens. Matter Mater. Phys.* **1988**, *37*, 785.
- (42) Vosko, S. H.; Wilk, L.; Nusair, M. Accurate spin-dependent electron liquid correlation energies for local spin density calculations: a critical analysis. *Can. J. Phys.* **1980**, *58*, 1200.
- (43) Grimme, S.; Antony, J.; Ehrlich, S.; Krieg, H. A consistent and accurate ab initio parametrization of density functional dispersion correction (DFT-D) for the 94 elements H-Pu. *J. Chem. Phys.* **2010**, *132*, 154104.
- (44) Grimme, S.; Ehrlich, S.; Goerigk, L. Effect of the damping function in dispersion corrected density functional theory. *J. Comput. Chem.* **2011**, *32*, 1456.
- (45) Lenthe, E. v.; Baerends, E. J.; Snijders, J. G. Relativistic regular two-component hamiltonians. *J. Chem. Phys.* **1993**, *99*, 4597.
- (46) Van Lenthe, E.; Ehlers, A.; Baerends, E.-J. Geometry optimizations in the zero order regular approximation for relativistic effects. *J. Chem. Phys.* **1999**, *110*, 8943.
- (47) Van Wüllen, C. Molecular density functional calculations in the regular relativistic approximation: Method, application to coinage metal diatomics, hydrides, fluorides and chlorides, and comparison with first-order relativistic calculations. *J. Chem. Phys.* **1998**, *109*, 392.
- (48) Klamt, A.; Schuurman, D. COSMO: a new approach to dielectric screening in solvents with explicit expressions for the screening energy and its gradient. *J. Chem. Soc., Perkin Trans. 2* **1993**, 799.
- (49) Sinnecker, S.; Rajendran, A.; Klamt, A.; Diedenhofen, M.; Neese, F. Calculation of solvent shifts on electronic g-tensors with the conductor-like screening model (COSMO) and its self-consistent generalization to real solvents (Direct COSMO-RS). *J. Phys. Chem. A* **2006**, *110*, 2235.
- (50) Weigend, F.; Ahlrichs, R. Balanced basis sets of split valence, triple zeta valence and quadruple zeta valence quality for H to Rn: Design and assessment of accuracy. *Phys. Chem. Chem. Phys.* **2005**, *7*, 3297.
- (51) Pantazis, D. A.; Chen, X. Y.; Landis, C. R.; Neese, F. All-electron scalar relativistic basis sets for third-row transition metal atoms. *J. Chem. Theory Comput.* **2008**, *4*, 908.
- (52) Neese, F. An improvement of the resolution of the identity approximation for the formation of the Coulomb matrix. *J. Comput. Chem.* **2003**, *24*, 1740.
- (53) Neese, F.; Wennmohs, F.; Hansen, A.; Becker, U. Efficient, approximate and parallel Hartree-Fock and hybrid DFT calculations. A 'chain-of-spheres' algorithm for the Hartree-Fock exchange. *Chem. Phys.* **2009**, *356*, 98.
- (54) Neese, F. The ORCA program system. *WIREs Comput. Mol. Sci.* **2012**, *2*, 73.
- (55) Weigend, F. Accurate Coulomb-fitting basis sets for H to Rn. *Phys. Chem. Chem. Phys.* **2006**, *8*, 1057.
- (56) Staroverov, V. N.; Scuseria, G. E.; Tao, J.; Perdew, J. P. Comparative assessment of a new nonempirical density functional: Molecules and hydrogen-bonded complexes. *J. Chem. Phys.* **2003**, *119*, 12129.
- (57) Cox, N.; Ames, W.; Epel, B.; Kulik, L. V.; Rapatskiy, L.; Neese, F.; Messinger, J.; Wieghardt, K.; Lubitz, W. Electronic Structure of a

Weakly Antiferromagnetically Coupled Mn(II)Mn(III) Model Relevant to Manganese Proteins: A Combined EPR,  $^{55}\text{Mn}$ -ENDOR, and DFT Study. *Inorg. Chem.* **2011**, *50*, 8238.

(58) Zheng, M.; Khangulov, S. V.; Dismukes, G. C.; Barynin, V. V. Electronic structure of dimanganese(II,III) and dimanganese(III,IV) complexes and dimanganese catalase enzyme: a general EPR spectral simulation approach. *Inorg. Chem.* **1994**, *33*, 382.

(59) Bencini, A.; Gatteschi, D. *EPR of Exchange Coupled Systems*; Springer-Verlag: Berlin, 1990.

(60) Sage, J. T.; Xia, Y. M.; Debrunner, P. G.; Keough, D. T.; De Jersey, J.; Zerner, B. Moessbauer analysis of the binuclear iron site in purple acid phosphatase from pig allantoin fluid. *J. Am. Chem. Soc.* **1989**, *111*, 7239.

(61) Kulik, L. V.; Epel, B.; Lubitz, W.; Messenger, J. Electronic structure of the  $\text{Mn}_4\text{O}_3\text{Ca}$  cluster in the  $S_0$  and  $S_2$  states of the oxygen-evolving complex of photosystem II based on pulse  $^{55}\text{Mn}$  ENDOR and EPR Spectroscopy. *J. Am. Chem. Soc.* **2007**, *129*, 13421.

(62) Sinnecker, S.; Neese, F.; Noodleman, L.; Lubitz, W. Calculating the Electron Paramagnetic Resonance Parameters of Exchange Coupled Transition Metal Complexes Using Broken Symmetry Density Functional Theory: Application to a Mn(III)/Mn(IV) Model Compound. *J. Am. Chem. Soc.* **2004**, *126*, 2613.

(63) Pantazis, D. A.; Orio, M.; Petrenko, T.; Zein, S.; Bill, E.; Lubitz, W.; Messenger, J.; Neese, F. A new quantum chemical approach to the magnetic properties of oligonuclear transition-metal complexes: Application to a model for the tetranuclear manganese cluster of Photosystem II. *Chem. Eur. J.* **2009**, *15*, 5108.

(64) Orio, M.; Pantazis, D. A.; Petrenko, T.; Neese, F. Magnetic and Spectroscopic Properties of Mixed Valence Manganese(III,IV) Dimers: A Systematic Study Using Broken Symmetry Density Functional Theory. *Inorg. Chem.* **2009**, *48*, 7251.

(65) Schinzel, S.; Kaupp, M. Validation of broken-symmetry density functional methods for the calculation of electron paramagnetic resonance parameters of dinuclear mixed-valence MnIVMnIII complexes. *Can. J. Chem.* **2009**, *87*, 1521.

(66) Han, W.-G.; Liu, T.; Lovell, T.; Noodleman, L. Active Site Structure of Class I Ribonucleotide Reductase Intermediate X: A Density Functional Theory Analysis of Structure, Energetics, and Spectroscopy. *J. Am. Chem. Soc.* **2005**, *127*, 15778.

(67) Han, W.-G.; Noodleman, L. DFT calculations of comparative energetics and ENDOR/Mössbauer properties for two protonation states of the iron dimer cluster of ribonucleotide reductase intermediate X. *Dalton T.* **2009**, 6045.

(68) Schäfer, K. O. Exchange Coupled Manganese Complexes: Model Systems for the Active Centres of Redoxproteins Investigated with EPR Techniques. Doctoral Thesis, Technische Universität, Berlin, 2002.

(69) Tan, X. L.; Gultneh, Y.; Sarneski, J. E.; Scholes, C. P. EPR-ENDOR of the electronic structure from two nitrogenously ligated bis( $\mu$ -oxo)-manganese(III)-manganese(IV) model complexes spectroscopically relevant to the multi-manganese center of photosystem II. *J. Am. Chem. Soc.* **1991**, *113*, 7853.

(70) Höfer, P.; Grupp, A.; Nebenführ, H.; Mehring, M. Hyperfine sublevel correlation (hyscore) spectroscopy: a 2D ESR investigation of the squaric acid radical. *Chem. Phys. Lett.* **1986**, *132*, 279.

(71) Thomann, H.; Bernardo, M.; Goldfarb, D.; Kroneck, P. M. H.; Ullrich, V. Evidence for Water Binding to the Fe Center in Cytochrome P450cam Obtained by  $^{17}\text{O}$  Electron Spin-Echo Envelope Modulation Spectroscopy. *J. Am. Chem. Soc.* **1995**, *117*, 8243.

(72) Andersson, C. S.; Högbom, M. A Mycobacterium tuberculosis ligand-binding Mn/Fe protein reveals a new cofactor in a remodeled R2-protein scaffold. *Proc. Natl. Acad. Sci. U. S. A.* **2009**, *106*, 5633.

(73) Griese, J.; Srinivas, V.; Högbom, M. Assembly of nonheme Mn/Fe active sites in heterodinuclear metalloproteins. *JBIC, J. Biol. Inorg. Chem.* **2014**, *19*, 759.

(74) Dassama, L. M. K.; Krebs, C.; Bollinger, J. M.; Rosenzweig, A. C.; Boal, A. K. Structural Basis for Assembly of the MnIV/FeIII Cofactor in the Class Ic Ribonucleotide Reductase from *Chlamydia trachomatis*. *Biochemistry* **2013**, *52*, 6424.

(75) Fiege, R.; Zweggart, W.; Bittl, R.; Adir, N.; Renger, G.; Lubitz, W. EPR and ENDOR studies of the water oxidizing complex of Photosystem II. *Photosynth. Res.* **1996**, *48*, 227.

(76) Pantazis, D. A.; Krewald, V.; Orio, M.; Neese, F. Theoretical magnetochemistry of dinuclear manganese complexes: broken symmetry density functional theory investigation on the influence of bridging motifs on structure and magnetism. *Dalton Trans.* **2010**, 39, 4959.

(77) Sinnecker, S.; Neese, F.; Lubitz, W. Dimanganese catalase - spectroscopic parameters from broken-symmetry density functional theory of the superoxidized Mn<sup>III</sup>/Mn<sup>IV</sup> state. *J. Biol. Inorg. Chem.* **2005**, *10*, 231.

(78) Mukhopadhyay, S.; Mandal, S. K.; Bhaduri, S.; Armstrong, W. H. Manganese clusters with relevance to photosystem II. *Chem. Rev.* **2004**, *104*, 3981.

(79) Neese, F. Theoretical Study of Ligand Superhyperfine Structure. Application to Cu(II) Complexes. *J. Phys. Chem. A* **2001**, *105*, 4290.

(80) Cotruvo, J. A.; Stubbe, J.; Class, I. Ribonucleotide Reductases: Metallocofactor Assembly and Repair In Vitro and In Vivo. *Annu. Rev. Biochem.* **2011**, *80*, 733.

(81) Cotruvo, J. A.; Stich, T. A.; Britt, R. D.; Stubbe, J. Mechanism of Assembly of the Dimanganese-Tyrosyl Radical Cofactor of Class Ib Ribonucleotide Reductase: Enzymatic Generation of Superoxide Is Required for Tyrosine Oxidation via a Mn(III)Mn(IV) Intermediate. *J. Am. Chem. Soc.* **2013**, *135*, 4027.

### 3.3. Recent developments in biological water oxidation

*Montserrat Pérez-Navarro, Frank Neese, Wolfgang Lubitz, Dimitrios A Pantazis, Nicholas Cox.*

*Published in Current Opinion in Chemical Biology 31 (2016): 113-119. Copyright 2016 National Academy of Sciences.*

The current hot topics in the field of biological water oxidation were discussed in this review, including our own results from Mülheim campus. In particular, the two popular proposals to describe the mechanism of water oxidation to obtain molecular oxygen: i) radical coupling of two oxygens; ii) nucleophilic attack involving an acid base type reaction. Current results found in the literature do not constrain the mechanism of O-O bond formation, but they do point to two proximal oxygens bound to Mn1 and Mn4 being the most probable candidates for the two substrate oxygens. Studies where the OEC are structurally distorted or perturbed due to site directed mutagenesis or addition of a substrate-like molecule brought relevant information for the mechanism, especially when the catalytic activity is affected. The results obtained after replacement of  $\text{Ca}^{2+}$  for  $\text{Sr}^{2+}$  and/or addition of  $\text{NH}_3/\text{H}_2^{17}\text{O}$  were included in this discussion. Taking into account all the up-to date published information and our latest results, we go on to describe a complete sequence of intermediates, which expanded the catalytic cycle (Figure 12).

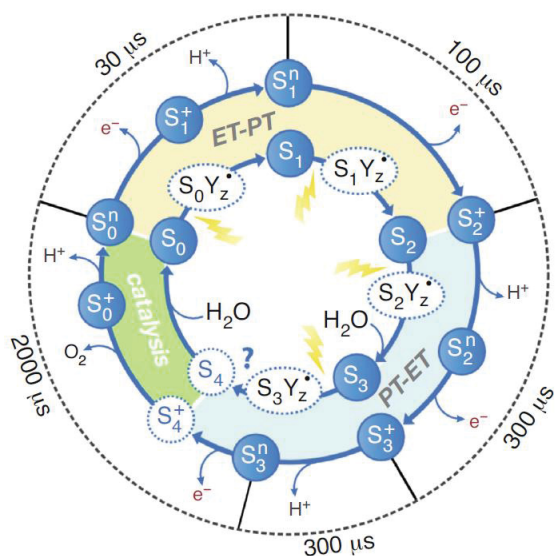


*Figure 12. Extended nine intermediate S-state cycle of the  $\text{Mn}_4\text{O}_5\text{Ca}$  cofactor.<sup>55</sup> The cycle starts in the neutral state,  $S_0^n$ . Electron withdrawal precedes proton transfer up until  $S_2^+$ . Generation of the  $S_3^+$  and  $S_4^+$  states requires first proton transfer, and then oxidation. After spontaneous release of molecular oxygen, the  $S_0^n$  is regenerated.*



ELSEVIER

## Recent developments in biological water oxidation

Montserrat Pérez-Navarro<sup>1</sup>, Frank Neese<sup>1</sup>, Wolfgang Lubitz<sup>1</sup>,  
Dimitrios A Pantazis<sup>1</sup> and Nicholas Cox<sup>1,2</sup>

Rapid progress has been made in the last five years towards resolution of the structure of nature's water splitting catalyst — a  $\text{Mn}_4\text{O}_5\text{Ca}$  cofactor embedded in Photosystem II — especially in the field of X-ray crystallography. In addition, recent magnetic resonance data have allowed the structure of the cofactor to be accessed in its last metastable intermediate state, prior to O–O bond formation. This activated form of the catalyst is geometrically similar to that seen by X-ray crystallography, which represents the resting state of the cofactor, but requires the coordination of an additional water molecule to the cofactor, rendering all Mn ions six coordinate. Importantly, it locates two water derived, Mn bound oxygen ligands in close proximity. It is these two oxygen ligands that likely form the product  $\text{O}_2$  molecule, as proposed earlier by quantum chemical modeling. Current views on the molecular level events that facilitate catalyst activation, that is, catalyst/substrate deprotonation, Mn oxidation and water molecule insertion are briefly described.

### Addresses

<sup>1</sup>Max Planck Institute for Chemical Energy Conversion, Stiftstr. 34-36, D-45470 Mülheim an der Ruhr, Germany

<sup>2</sup>Research School of Chemistry, Australian National University, Canberra, ACT 2601, Australia

Corresponding author: Cox, Nicholas ([nicholas.cox@cec.mpg.de](mailto:nicholas.cox@cec.mpg.de))

Current Opinion in Chemical Biology 2016, 31:113–119

This review comes from a themed issue on **Biocatalysis and biotransformation**

Edited by **Dan S Tawfik** and **Wilfred A van der Donk**

For a complete overview see the [Issue](#) and the [Editorial](#)

Available online 17th March 2016

<http://dx.doi.org/10.1016/j.cbpa.2016.02.007>

1367-5931/© 2016 Elsevier Ltd. All rights reserved.

### The structure of nature's water splitting cofactor in its resting state

Crystallographic advances, including the introduction of free electron laser sources, have fundamentally altered the trajectory of research on the mechanism of biological water splitting [1••]. These new methods have recently provided an atomic resolution crystal structure of the resting state of the catalyst. Specifically, the XFEL (X-ray free electron laser) structure: (i) reproduces earlier EXAFS constraints (e.g. Mn–Mn distances) [2,3,4•]; (ii) clarifies the location of all oxygen bridges of the catalyst including the O5 bridge, which in earlier X-ray models

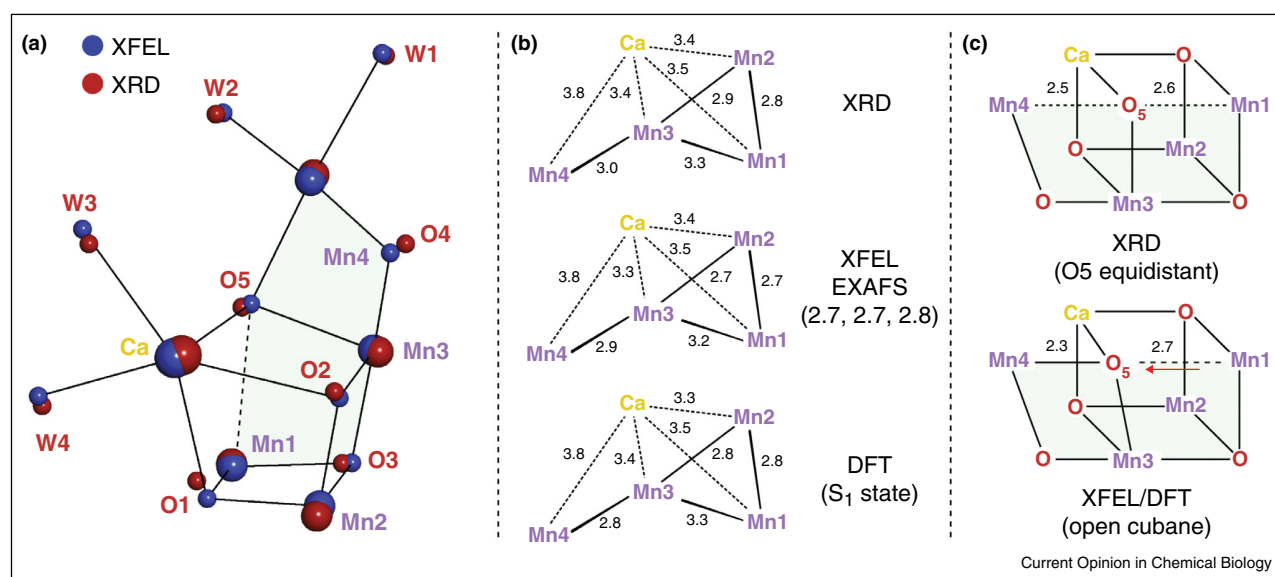
(XRD) was placed in a chemically unprecedented bonding position; and (iii) constrains the net oxidation state of the cofactor in the resting state (III, IV, IV, III) by resolving the Jahn–Teller axes of two  $\text{Mn}^{\text{III}}$  ions, Mn1 and Mn4 (see Figure 1). This novel structure allows the information content of complementary spectroscopies to be fully realized and together these data now provide a solid basis for the development of robust chemical models throughout its entire catalytic cycle [5•].

### Substrate binding and delivery to the catalyst

An understanding of the mechanism of biological water splitting is greatly aided by resolving what oxygen sites of the cofactor participate in the reaction [12•,13]. Recent magnetic resonance data has implicated O5 as one of the two substrates owing to its fast exchange with bulk solvent water [14•,15•,16]. This is a unique property not seen for the other four bridges, or for oxygen bridges in simpler synthetic model systems [17–19]. The identity of the second substrate remains more contentious as it is unclear if it is bound in all intermediate states of the catalyst, or if bound in all states, whether its position changes during the cycle [12•,20]. Water analogs such as ammonia and methanol provide a means to address this question by probing how the substrates first access the cofactor. Substrate access forms part of a larger debate on the dynamics of the solvent/substrate interface, namely how does the catalyst selectively *activate* two solvent water molecules (when it is surrounded by solvent water) and *regulate* solvent water access to the site of the catalyst, to avoid deleterious side products such as  $\text{H}_2\text{O}_2$ .

Although ammonia and methanol do not drastically alter the binding/exchange kinetics of the two substrates, their addition is associated with a decrease of the catalyst's efficiency under steady-state conditions suggesting that they hinder or interfere with substrate access to the site(s) of catalysis. The crystal structure identifies at least three water pathways leading towards/away from the cofactor: (i) a channel which includes the  $\text{Ca}^{2+}$  ion and the redox active tyrosine residue ( $\text{Y}_Z$ ); (ii) a channel which includes the outer Mn4 and the Asp61 residue [1,6]; and (iii) a similar channel which also includes the  $\text{Cl}^-$  ion (Figure 2a). The location of ammonia binding was recently deduced from chemical modeling [14•,15•,22] and mutagenesis [23•], displacing the water ligand (W1) of the outer manganese (Mn4). The binding location of methanol, however, is less well defined, with one option placing it close to the site of ammonia binding and another favoring its binding at the  $\text{Ca}^{2+}$  ion [24]. Competitive

Figure 1



(A) Comparison of the new XFEL structure with the earlier synchrotron (XRD) structure of the Mn<sub>4</sub>O<sub>5</sub>Ca cofactor [1,6]. The cofactor resembles a distorted chair with the back of the chair shown by the light blue plane. The XFEL structure better reproduces EXAFS constraints [2,3] (panel B) and places O5 in a more chemically realistic position (panel C), more in line with earlier chemical models [5,7–9]. The cofactor contains three coordinately saturated Mn ions (Mn2, Mn3 and Mn4) with a potential substrate binding site located at Mn1, the only five coordinate Mn ion. Mn4 and the Ca<sup>2+</sup> ion both carry two water derived ligands. All remaining ligands are derived from the protein backbone and oxygen bridge network. Substitution of the Ca<sup>2+</sup> ion with Sr<sup>2+</sup> has little effect on the structure of the catalyst [10], in line with spectroscopic results [11].

binding of small molecules at/near the position of W1 indicate that the water channel associated with this site (Asp61 channel) is important for water delivery [25<sup>\*\*</sup>]. As a whole, these results favor that one of the water derived ligands of the Mn4 is the second substrate. Water binding via the Asp61 channel involves a rotation of the waters on the Mn4, initiated by the facile shift of the O5 bridge [9,21]. This cascade of structural rearrangements results in a five coordinate, trigonal bipyramidal Mn ion, shown in Figure 2 [25<sup>\*\*</sup>]. Within this model water binding occurs on the back-face of the cofactor. As such the water molecule when first delivered is most likely not the substrate of the reaction – this is instead one of the existing water ligands (W2) – but form the substrate in the next catalytic cycle, see [12<sup>\*</sup>,20].

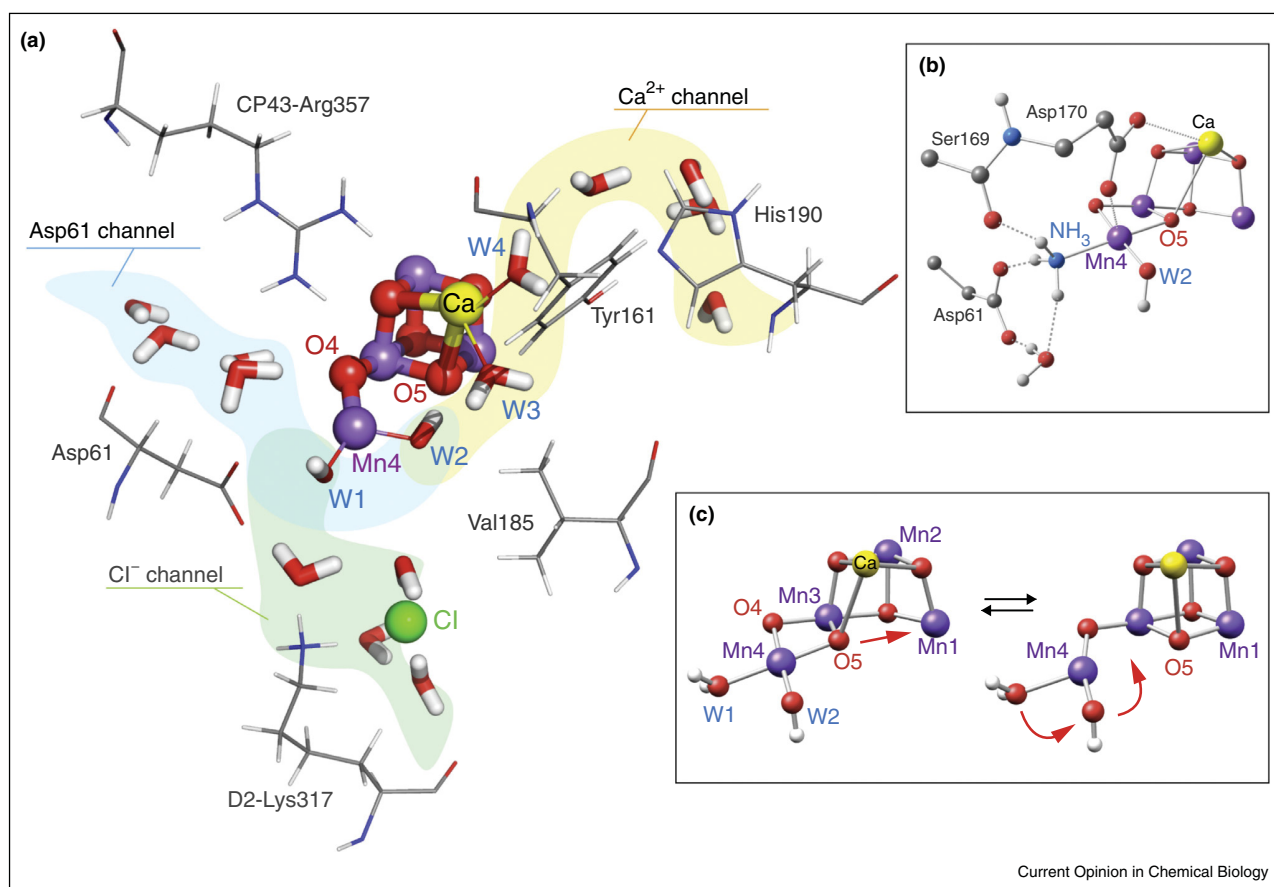
### The structure of the activated catalyst – structural evolution during the S-state

It is well known that the cofactor cycles through a series of five intermediate states: S<sub>0</sub>, S<sub>1</sub> (dark stable), S<sub>2</sub>, S<sub>3</sub>, and S<sub>4</sub> where the subscript refers to the number of oxidizing equivalents stored by the cofactor. The S<sub>4</sub> state spontaneously decays upon release of triplet O<sub>2</sub> returning to the S<sub>0</sub> state. Oxidation of the cofactor is driven by light excitation of the Photosystem II reaction center, via a redox active tyrosine residue (Y<sub>Z</sub>). Coupled with oxidation, protons are successively removed from the cofactor, to ensure its total charge/redox potential remains constant, termed redox

tuning or redox leveling. As such the cycle can more accurately be described in terms of nine states which differ in terms of their net electron and proton count [26,27<sup>\*</sup>] (Figure 3). An important observation is that at different points in the cycle the order in which electrons and protons are removed from the cofactor reverses; in the early S-state transitions (e.g. S<sub>0</sub> to S<sub>1</sub>) electron transfer precedes proton transfer whereas in the late transitions (e.g. S<sub>2</sub> to S<sub>3</sub>) proton transfer precedes electron transfer [26,27<sup>\*</sup>]. As a consequence, Y<sub>Z</sub> can be thought of having a dual role: first, it acts as an electron carrier; and second, it promotes deprotonation of the catalyst which is presumably facilitated via the intervening H-bonding network.

The XFEL structure described above represents the resting state of the catalyst (S<sub>1</sub>) [1<sup>\*\*</sup>], although it may contain some admixture of the S<sub>0</sub> state [5<sup>\*</sup>]. It is also thought to be a good model for the S<sub>2</sub> state as EXAFS results for the S<sub>0</sub>, S<sub>1</sub> and S<sub>2</sub> are all very similar [2,3] and progression from the S<sub>1</sub> to the S<sub>2</sub> state can occur at low temperatures (<200 K), where the protein's conformation should be fixed. The same however cannot be said of the S<sub>3</sub> state, the last metastable intermediate of the reaction cycle. Recent pulse EPR data has demonstrated that in this state all four Mn ions are structurally and electronically *similar*: they all exhibit a formal oxidation state 4+ and octahedral local geometry [28<sup>\*\*</sup>]. This requires the inclusion of an additional water-derived ligand at the

Figure 2



**(a)** Proposed access/egress channels to and from the  $\text{Mn}_4\text{O}_5\text{Ca}$  cofactor. **(b)** Binding location of  $\text{NH}_3$  which displaces the water ligand (W1) to the outer manganese (Mn4). Its binding was used to identify the exchangeable oxygen bridge (O5) as ammonia binds near (*trans* to) the O5 bridge. **(c)** Sequence of oxygen ligand movements that allow water binding to occur. Spectroscopic data support the cofactor being able to adopt open and closed cubane conformation, in support of this mechanism for substrate delivery [9,21].

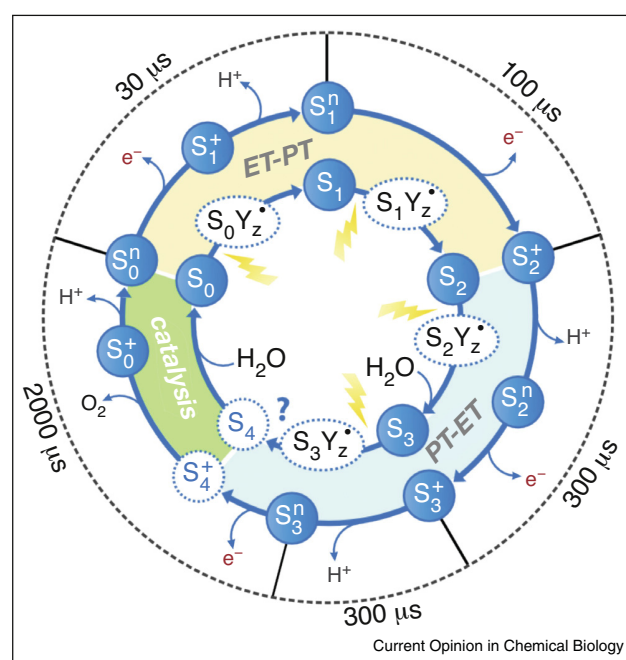
open coordination site of Mn1 rendering all four Mn ions six-coordinate [28<sup>••</sup>,29]. Importantly the proposed activated structure locates two oxygens 2.4 Å apart along the Mn1–Mn4 axis, the two likely substrates of the water splitting reaction, one of which is O5 in line with experimental results described above [7,30].

The question arises as to how this structure evolves from the resting state of the catalyst captured using X-ray crystallography. As indicated above the position of O5 is not fixed but toggles between two positions, as an oxygen bridge between Mn3 and Mn4, as seen in the X-ray structure (open cubane form), and as a vertex of the cubane unit (closed cubane form) [9,21] (Figure 2c). O5 does not display this property in all S-states, but instead evolves towards this dynamic state in the  $S_2$  state, as it is only in this state that O5 movement can be coupled with valence isomerism within the cluster [9,21]. It is this labile nature of O5 that provides a possible mechanism via

which the solvent inaccessible Mn1 is then connected to the Asp61 water channel described in the previous section (Figure 4). Briefly, the shift of O5 moves the open coordination site of the cofactor to the solvent accessible Mn4 [25<sup>••</sup>,31<sup>•</sup>]. This site is then filled by the rotation of the water ligands of Mn4 (W2/W1,  $S_3^A$ ), with binding of a new water molecule via the Asp61 channel [25<sup>••</sup>]. We note the  $\text{Ca}^{2+}$  channel could also provide the new water molecule. Subsequently, the protonation of the two water derived oxygens on the Mn1–Mn4 axis interchanges leading to the final activated catalyst structure ( $S_3^A$ ) [32<sup>•</sup>]. Importantly this pathway explains earlier spectroscopic results that suggested the net solvation increases in the  $S_2$  to  $S_3$  transition [12<sup>•</sup>,33].

It is likely that the sequential uptake of the substrate waters, with the delayed repositioning of the second substrate, is critical for efficient catalytic function yielding a single product. While the sequence described above provides a

Figure 3



Extended, nine intermediate S-state cycle of the  $Mn_4O_5Ca$  cofactor, based on [26]. The cycle starts in the  $S_0^n$  state ( $n$  = neutral) state. Up until the  $S_2^+$ , electron withdrawal precedes proton transfer (ET-PT). Subsequently, generation of the  $S_3^+$  and  $S_4^+$  states requires first proton transfer then oxidation (PT-ET).  $S_0^n$  is regenerated upon the spontaneous release of molecular oxygen and likely the binding and deprotonation of one of the substrates.

plausible access pathway for substrate binding/inclusion, the critical question is how this process is regulated. Experimental and theoretical results point to a gating mechanism involving proton shuffling from W1 to the Asp61 [31<sup>•</sup>,35–37], potentially by a rearrangement of the net electric dipole of the cofactor induced by  $Y_Z$  oxidation [38]. This redox tuning event then allows cofactor oxidation and subsequently substrate binding to the Mn4, which in the 4+ oxidation state is a better Lewis acid [25<sup>•</sup>,34]. In this way connections between the conversion of the catalyst from its resting to its active form with the two phases of the catalytic cycle (Figures 3 and 4) can begin to be made. In the resting-like states (Figure 4, low panel:  $S_0^A, S_1^A, S_2^A$ ) the two putative substrates are kept away from each other and the cofactor is uncoupled from the protein surrounding, i.e. the ET-PT phase. In contrast, in the active-like states (Figure 4, upper panel:  $S_2^B, S_3^A, S_3^B$ ) the two putative substrates are proximal to each other and the cofactor is coupled to the protein surrounding, i.e. the PT-ET phase. It is also noted that the two basic forms of the catalyst have a different electronic structure as evidenced by their ground spin state [34]. The resting state forms ( $S_0^A, S_1^A, S_2^A$ ) are all low spin whereas the active forms ( $S_2^B, S_3^A, S_3^B$ ) of the catalyst are high spin. The significance of this change in the electronic structure,

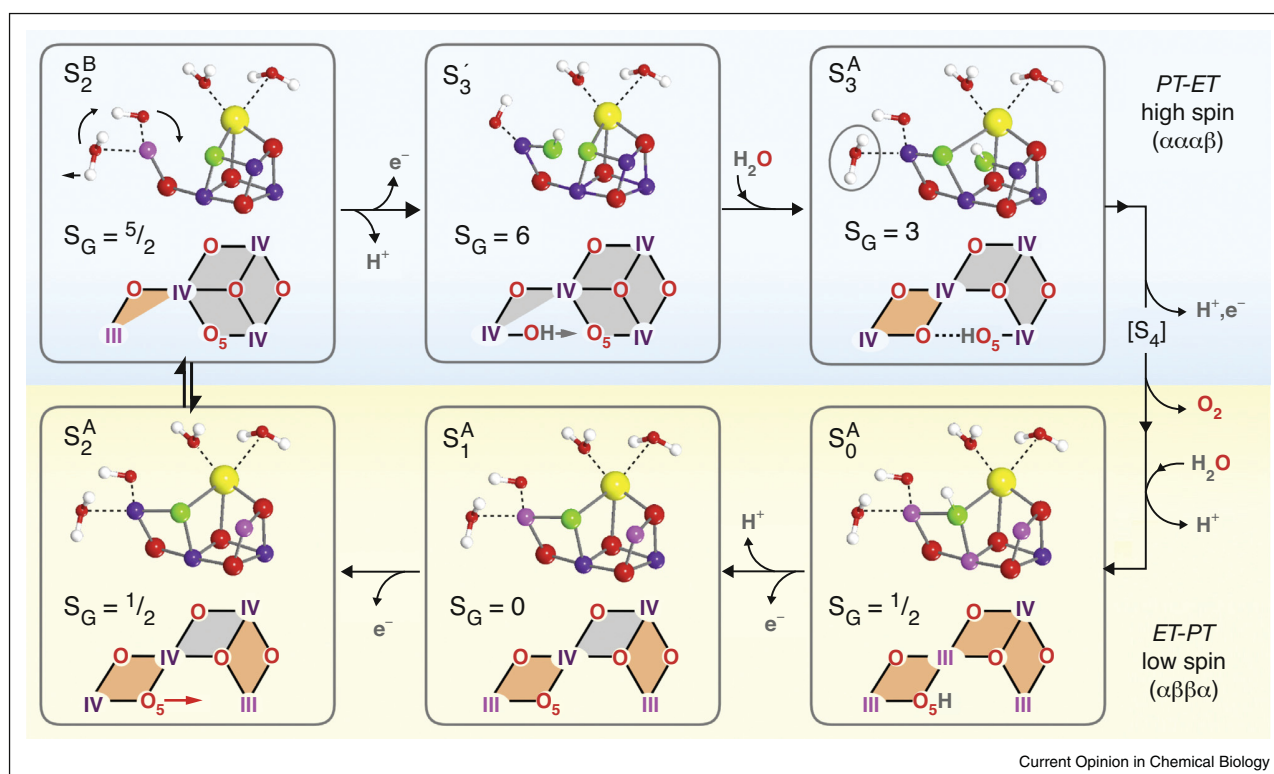
triggered by the  $S_2$  to  $S_3$  water binding step, is not yet understood but it has been suggested as critical for stabilization of the O–O bond forming transition state [28<sup>••</sup>,34].

### The O–O bond formation step

While recent results described above do not yet constrain the mechanism of water oxidation, they do provide a solid foundation to address this question. Importantly they point towards a mechanism involving the two proximal Mn-bound oxygens, seen in the activated catalyst structure, which are located along the Mn1 and Mn4 axis. There are two popular proposals in the literature explaining how the O–O bond formation could proceed, either by: (i) a radical coupling of the two oxygen as proposed by Siegbahn [30] or instead (ii) an acid base type reaction involving nucleophilic attack [39]. Current experimental data favor a coupling-type reaction, involving oxidation of one of the substrate oxygens, in part because no  $Mn^V$  intermediate has yet been observed [40]. The challenge though is to devise new experiments to better tease apart the catalytic phase of the cycle (Figure 3, green area) to conclusively answer this question; namely to address what is the nature of the deprotonation step to form the  $S_3^+(Y_Z^{\bullet})$  state and what is the subsequent fate of this state. This however remains difficult. Obvious routes to capture these intermediates, such as using high external  $O_2$  pressures do not affect photosynthetic oxygen production [41–43], requiring the equilibrium constant for the  $S_4 \rightarrow S_0$  transition to be large ( $>1.0 \times 10^7$ ) [44]. A more promising approach is to use structurally perturbed systems in which the catalyst activity is diminished [45]. These include site directed mutants (e.g. Asp61, Val185) or replacement of the redox-inactive ions (the exchange of the  $Ca^{2+}$  ion for  $Sr^{2+}$ , the  $Cl^-$  ion(s) for  $Br^-$  etc.) which have been shown to slow the kinetics of O–O bond formation by a factor of up to 100 fold [46,47<sup>••</sup>]. This latter approach has allowed water exchange to be studied during the catalytic phase (Figure 3). Interestingly substrate exchange is arrested in  $S_3^+(Y_Z^{\bullet})$ , favoring a O–O bond mechanism involving substrates that are tightly bound immediately prior to O–O bond formation [47<sup>••</sup>]. This would be consistent with the proposed substrate identities described above that is O5 and rotated W2 [12<sup>•</sup>,25<sup>••</sup>,34].

A molecular description of why these structural modifications slow the kinetics of  $O_2$  production is not immediately obvious. In these systems the intrinsic O–O bond formation step could be slower, or these changes could instead act to retard the advancement of the cofactor through its cycle (Figure 4), by decoupling cofactor tautomerism from proton release and second substrate inclusion. Clearly further spectroscopic characterizations of these perturbed systems are needed. Of these, new X-ray methods using free electron laser sources have the potential to provide key information, supplementing data already available on the structural and electronic evolution of the native cofactor during the catalysis phase of the cycle [48]. The goal for the

Figure 4



Self-consistent structures of the  $\text{Mn}_4\text{O}_5\text{Ca}$  cofactor during its catalytic cycle developed on the Mülheim campus [5\*,25\*\*,34]. Chemical models shown rationalize many experimental constraints and reproduce all structural and spectroscopic observables. Substrate oxygens are shown in green:  $\text{O}_5$  and the rotated  $\text{W}2$   $\text{Mn}4$  ligand [12\*,25\*\*,34]. 2D electronic coupling maps of the cofactor are shown below each structure, showing how the spin state of the cofactor evolves from low spin configuration in the resting states (dominantly antiferromagnetic coupling between adjacent Mn sites, orange pathways) to high spin configuration in the active states (dominantly ferromagnetic coupling between adjacent Mn sites, grey pathways).

future is to determine complete structures of short lived intermediates of the whole catalytic cycle, as free electron laser sources allow diffraction patterns to be collected within femtoseconds of X-ray exposure, providing snapshots of the O–O bond formation step even at ambient temperature [48,49].

## Acknowledgements

This work was supported by the Cluster of Excellence RESOLV (EXC 1069) and the DIP (Lu 315/17-1), both funded by the Deutsche Forschungsgemeinschaft and the project MANGAN (03EK3545) funded by the Bundesministerium für Bildung und Forschung (BMBF). N.C. thanks the Australian Research Council (FT140100834).

## References and recommended reading

Papers of particular interest, published within the period of review, have been highlighted as:

- of special interest
  - of outstanding interest
1. Suga M, Akita F, Hirata K, Ueno G, Murakami H, Nakajima Y, Shimizu T, Yamashita K, Yamamoto M, Ago H, Shen J-R: **Native**

### structure of photosystem II at 1.95 Å resolution viewed by femtosecond X-ray pulses. *Nature* 2015, 517:99-103.

This study reports the first 'radiation-damage-free' geometric arrangement of the  $\text{Mn}_4\text{CaO}_5$  cluster in the  $\text{S}_1$  state. Together with the earlier structure of Umena *et al.*, these data form the basis of our current understanding of the biological water splitting mechanism.

2. Yano J, Yachandra V: **Mn<sub>4</sub>Ca cluster in photosynthesis: where and how water is oxidized to dioxygen.** *Chem Rev* 2014, 114:4175-4205.
  3. Grundmeier A, Dau H: **Structural models of the manganese complex of photosystem II and mechanistic implications.** *Biochim Biophys Acta (BBA) – Bioenergetics* 2012, 1817:88-105.
  4. Beckwith MA, Ames W, Vila FD, Krewald V, Pantazis DA, Mantel C, Pécaut J, Gennari M, Duboc C, Collomb M-N, Yano J, Rehr JJ, Neese F, DeBeer S: **How accurately can extended x-ray absorption spectra be predicted from first principles? Implications for modeling the oxygen-evolving complex in photosystem II.** *J Am Chem Soc* 2015, 137:12815-12834.
- This study critically assesses the accuracy and reliability of predicting EXAFS spectra based on quantum chemical calculations.

5. Krewald V, Retegan M, Cox N, Messinger J, Lubitz W, DeBeer S, Neese F, Pantazis DA: **Metal oxidation states in biological water splitting.** *Chem Sci* 2015, 6:1676-1695.
- This computational study evaluated an extensive set of models of the biological water splitting cofactor for all stable S-states with respect to all the available experimental data. A single, self-consistent cycle was

deduced, based on the high-valent oxidation state model:  $S_0$  (III, III, III, IV)  $\rightarrow$   $S_3$  (IV, IV, IV, IV).

6. Umena Y, Kawakami K, Shen J-R, Kamiya N: **Crystal structure of oxygen-evolving photosystem II at a resolution of 1.9 Å.** *Nature* 2011, **473**:55-60.
7. Siegbahn PEM: **Water oxidation mechanism in photosystem II, including oxidations, proton release pathways, O–O bond formation and O<sub>2</sub> release.** *Biochim Biophys Acta (BBA) – Bioenergetics* 2013, **1827**:1003-1019.
8. Lubner S, Rivalta I, Umena Y, Kawakami K, Shen J-R, Kamiya N, Brudvig GW, Batista VS: **S<sub>1</sub>-state model of the O<sub>2</sub>-evolving complex of photosystem II.** *Biochemistry* 2011, **50**:6308-6311.
9. Pantazis DA, Ames W, Cox N, Lubitz W, Neese F: **Two interconvertible structures that explain the spectroscopic properties of the oxygen evolving complex of photosystem II in the S<sub>2</sub> state.** *Angew Chem Int Ed* 2012, **51**:9935-9940.
10. Koua FHM, Umena Y, Kawakami K, Shen J-R: **Structure of Sr-substituted photosystem II at 2.1 Å resolution and its implications in the mechanism of water oxidation.** *Proc Natl Acad Sci U S A* 2013, **110**:3889-3894.
11. Cox N, Rapatskiy L, Su J-H, Pantazis DA, Sugiura M, Kulik L, Dorlet P, Rutherford AW, Neese F, Boussac A, Lubitz W, Messinger J: **Effect of Ca<sup>2+</sup>/Sr<sup>2+</sup> substitution on the electronic structure of the oxygen-evolving complex of photosystem II: a combined multifrequency EPR, <sup>55</sup>Mn-ENDOR, and DFT study of the S<sub>2</sub> state.** *J Am Chem Soc* 2011, **133**:3635-3648.
12. Cox N, Messinger J: **Reflections on substrate water and dioxygen formation.** *Biochim Biophys Acta (BBA) – Bioenergetics* 2013, **1827**:1020-1030.  
This review compiles all experimental data related to the assignment of the two substrates of the biological water splitting reaction. The conclusion reached by the authors is that O5 likely represents the early binding substrate water (termed W<sub>slow</sub>) whereas W2 represents the late binding/relocated substrate (termed W<sub>fast</sub>). The labels 'fast' and 'slow' refer to the relative rates with which these two bound substrates exchange with bulk water.
13. Cox N, Pantazis DA, Neese F, Lubitz W: **Biological water oxidation.** *Acc Chem Res* 2013, **46**:1588-1596.
14. Lohmiller T, Krewald V, Pérez-Navarro M, Retegan M, Rapatskiy L, Nowaczyk MM, Boussac A, Neese F, Lubitz W, Pantazis DA, Cox N: **Structure, ligands and substrate coordination of the oxygen-evolving complex of photosystem II in the S<sub>2</sub> state: a combined EPR and DFT study.** *Phys Chem Chem Phys* 2014, **16**:11877-11892.  
In this study the identity of the exchangeable oxygen bridge of the water splitting cofactor was examined by site perturbation, namely the exchange of the Ca<sup>2+</sup> ion with Sr<sup>2+</sup>. This modification leads to a small change in the oxygen bridge signal suggesting the exchangeable bridge is a ligand of the Ca<sup>2+</sup>, most likely O5. This study also restricts the number of exchangeable bridges to be only one.
15. Pérez-Navarro M, Ames WM, Nilsson H, Lohmiller T, Pantazis DA, Rapatskiy L, Nowaczyk MM, Neese F, Boussac A, Messinger J, Lubitz W, Cox N: **Ammonia binding to the oxygen-evolving complex of photosystem II identifies the solvent-exchangeable oxygen bridge (μ-oxo) of the manganese tetramer.** *Proc Natl Acad Sci U S A* 2013, **110**:15561-15566.  
This EPR, DFT and time-resolved membrane inlet mass spectrometry study examined the binding of ammonia to the water splitting cofactor. It was observed that ammonia likely displaces the water (W1) ligand of Mn4. As ammonia binding simultaneously has a large effect on the exchangeable oxygen bridge, it was deduced that this bridge must be located *trans* to its binding position i.e. *trans* to W1, the O5 position.
16. Rapatskiy L, Cox N, Savitsky A, Ames WM, Sander J, Nowaczyk MM, Rögner M, Boussac A, Neese F, Messinger J: **Detection of the water-binding sites of the oxygen-evolving complex of photosystem II using W-band <sup>17</sup>O electron–electron double resonance-detected NMR spectroscopy.** *J Am Chem Soc* 2012, **134**:16619-16634.
17. McConnell IL, Grigoryants VM, Scholes CP, Myers WK, Chen P-Y, Whittaker JW, Brudvig GW: **EPR-ENDOR characterization of (<sup>17</sup>O, <sup>1</sup>H, <sup>2</sup>H) water in manganese catalase and its relevance to the oxygen-evolving complex of photosystem II.** *J Am Chem Soc* 2012, **134**:1504-1512.
18. Siegbahn PEM: **Substrate water exchange for the oxygen evolving complex in PSII in the S<sub>1</sub>, S<sub>2</sub>, and S<sub>3</sub> States.** *J Am Chem Soc* 2013, **135**:9442-9449.
19. Rapatskiy L, Ames WM, Perez-Navarro M, Savitsky A, Griese JJ, Weyhermüller T, Shafaat HS, Högbom M, Neese F, Pantazis DA, Cox N: **Characterization of oxygen bridged manganese model complexes using multifrequency <sup>17</sup>O-hyperfine EPR spectroscopies and density functional theory.** *J Phys Chem B* 2015, **119**:13904-13921.
20. Nilsson H, Krupnik T, Kargul J, Messinger J: **Substrate water exchange in photosystem II core complexes of the extremophilic red alga *Cyanidioschyzon merolae*.** *Biochim Biophys Acta (BBA) – Bioenergetics* 2014, **1837**:1257-1262.
21. Bovi D, Narzi D, Guidoni L: **The S<sub>2</sub> state of the oxygen evolving complex of photosystem II explored by QM/MM dynamics: spin surfaces and metastable states suggest a reaction path towards the S<sub>3</sub> state.** *Angew Chem Int Ed* 2013, **52**:11744-11749.
22. Schraut J, Kaupp M: **On ammonia binding to the oxygen-evolving complex of photosystem II: a quantum chemical study.** *Chem – Eur J* 2014, **20**:7300-7308.
23. Oyala PH, Stich TA, Debus RJ, Britt RD: **Ammonia binds to the dangler manganese of the Photosystem II oxygen-evolving complex.** *J Am Chem Soc* 2015, **137**:8829-8837.  
This study conclusively demonstrates that ammonia displaces the W1 ligand of Mn4. It is shown that mutation of the Asp61 residue, which provides a hydrogen bond to W1, perturbs the bound ammonia signal requiring ammonia to bind at the W1 site.
24. Oyala PH, Stich TA, Stull JA, Yu F, Pecoraro VL, Britt RD: **Pulse electron paramagnetic resonance studies of the interaction of methanol with the S<sub>2</sub> state of the Mn<sub>4</sub>O<sub>5</sub>Ca cluster of photosystem II.** *Biochemistry* 2014, **53**:7914-7928.
25. Retegan M, Krewald V, Mamedov F, Neese F, Lubitz W, Cox N, Pantazis DA: **A five-coordinate Mn(IV) intermediate in biological water oxidation: spectroscopic signature and a pivot mechanism for water binding.** *Chem Sci* 2016, **7**:72-84.  
This very recent work proposes a novel low barrier pathway for water insertion into the biological cofactor, facilitating cofactor activation. It identifies a new S<sub>3</sub> intermediate state which forms after cofactor oxidation but before water binding.
26. Klaus A, Haumann M, Dau H: **Alternating electron and proton transfer steps in photosynthetic water oxidation.** *Proc Natl Acad Sci U S A* 2012, **109**:16035-16040.
27. Klaus A, Haumann M, Dau H: **Seven steps of alternating electron and proton transfer in photosystem II water oxidation traced by time-resolved photothermal beam deflection at improved sensitivity.** *J Phys Chem B* 2015, **119**:2677-2689.  
Using a new spectroscopic technique, Time-Resolved Photothermal Beam Deflection, the authors were able to identify seven discrete transitions within the S-state cycle. These steps provide important information on the sequence of the alternate between electron transfer and charge-compensating proton transfer events that occur during the cycle.
28. Cox N, Retegan M, Neese F, Pantazis DA, Boussac A, Lubitz W: **Electronic structure of the oxygen-evolving complex in photosystem II prior to O–O bond formation.** *Science* 2014, **345**:804-808.  
As described in the main text, this study demonstrates that the stoichiometry of the biological water splitting cofactor changes in the final metastable intermediate state of the cycle (S<sub>3</sub>). These results require that the S<sub>2</sub> to S<sub>3</sub> transition involves a water binding event.
29. Li X, Siegbahn PE, Ryde U: **Simulation of the isotropic EXAFS spectra for the S<sub>2</sub> and S<sub>3</sub> structures of the oxygen evolving complex in photosystem II.** *Proc Natl Acad Sci U S A* 2015, **112**:3979-3984.
30. Li X, Siegbahn PEM: **Alternative mechanisms for O<sub>2</sub> release and O–O bond formation in the oxygen evolving complex of photosystem II.** *Phys Chem Chem Phys* 2015, **17**:12168-12174.
31. Narzi D, Bovi D, Guidoni L: **Pathway for Mn-cluster oxidation by tyrosine-Z in the S<sub>2</sub> state of photosystem II.** *Proc Natl Acad Sci U S A* 2014, **111**:8723-8728.  
This QM/MM study examines the initial phase of the S<sub>2</sub> to S<sub>3</sub> transition. The authors demonstrate that cofactor oxidation is triggered by proton shuffling between the Asp61 and W1, suggesting Asp61 participates in a

proton egress pathway, as had been proposed earlier from experiment. Importantly, oxidation of the cofactor is seen only for the closed ( $S_2^B$ ) state, not the open ( $S_2^A$ ) state.

32. Capone M, Bovi D, Narzi D, Guidoni L: **Reorganization of substrate waters between the closed and open cubane conformers during the  $S_2$  to  $S_3$  transition in the oxygen evolving complex.** *Biochemistry* 2015, **54**:6439-6442.
  - This very recent study examined the putative final rearrangement step in the  $S_2$  to  $S_3$  transition, which occurs after cofactor deprotonation, oxidation and water binding. The authors propose a novel mechanism allowing downhill conversion from a closed type intermediate structure ( $S_2^B$ ) to the experimentally observed open type structure ( $S_3^A$ ).
33. Noguchi T: **FTIR detection of water reactions in the oxygen-evolving centre of photosystem II.** *Philos Trans R Soc London B: Biol Sci* 2008, **363**:1189-1195.
34. Krewald V, Retegan M, Neese F, Lubitz W, Pantazis DA, Cox N: **Spin state as a marker for the structural evolution of nature's water-splitting catalyst.** *Inorg Chem* 2016, **55**:488-501.
35. Debus RJ: **Evidence from FTIR difference spectroscopy that D1-Asp61 influences the water reactions of the oxygen-evolving  $Mn_4CaO_5$  cluster of photosystem II.** *Biochemistry* 2014, **53**:2941-2955.
36. Siegbahn PEM: **Mechanisms for proton release during water oxidation in the  $S_2$  to  $S_3$  and  $S_3$  to  $S_4$  transitions in photosystem II.** *Phys Chem Chem Phys* 2012, **14**:4849-4856.
37. Rivalta I, Amin M, Lubner S, Vassiliev S, Pokhrel R, Umena Y, Kawakami K, Shen J-R, Kamiya N, Bruce D, Brudvig GW, Gunner MR, Batista VS: **Structural-functional role of chloride in photosystem II.** *Biochemistry* 2011, **50**:6312-6315.
38. Retegan M, Cox N, Lubitz W, Neese F, Pantazis DA: **The first tyrosyl radical intermediate formed in the  $S_2$ - $S_3$  transition of photosystem II.** *Phys Chem Chem Phys* 2014, **16**:11901-11910.
39. Sproviero EM, Gascón JA, McEvoy JP, Brudvig GW, Batista VS: **Quantum mechanics/molecular mechanics study of the catalytic cycle of water splitting in photosystem II.** *J Am Chem Soc* 2008, **130**:3428-3442.
40. Haumann M, Liebisch P, Müller C, Barra M, Grabolle M, Dau H: **Photosynthetic  $O_2$  formation tracked by time-resolved X-ray experiments.** *Science* 2005, **310**:1019-1021.
41. Haumann M, Grundmeier A, Zaharieva I, Dau H: **Photosynthetic water oxidation at elevated dioxygen partial pressure monitored by time-resolved X-ray absorption measurements.** *Proc Natl Acad Sci U S A* 2008, **105**:17384-17389.
42. Kolling DRJ, Brown TS, Ananyev G, Dismukes GC: **Photosynthetic oxygen evolution is not reversed at high oxygen pressures: mechanistic consequences for the water-oxidizing complex.** *Biochemistry* 2009, **48**:1381-1389.
43. Shevela D, Beckmann K, Clausen J, Junge W, Messinger J: **Membrane-inlet mass spectrometry reveals a high driving force for oxygen production by photosystem II.** *Proc Natl Acad Sci U S A* 2011, **108**:3602-3607.
44. Nilsson H, Cournac L, Rappaport F, Messinger J, Lavergne J: **Estimation of the driving force for dioxygen formation in photosynthesis.** *Biochim Biophys Acta (BBA) - Bioenergetics* 2016, **1857**:23-33.
45. Boussac A, Rutherford AW, Sugiura M: **Electron transfer pathways from the  $S_2$ -states to the  $S_3$ -states either after a  $Ca^{2+}/Sr^{2+}$  or a  $Cl^-/I^-$  exchange in Photosystem II from *Thermosynechococcus elongatus*.** *Biochim Biophys Acta (BBA) - Bioenergetics* 2015, **1847**:576-586.
46. Bao H, Burnap RL: **Structural rearrangements preceding dioxygen formation by the water oxidation complex of photosystem II.** *Proc Natl Acad Sci U S A* 2015, **112**:E6139-E6147.
47. Nilsson H, Rappaport F, Boussac A, Messinger J: **Substrate-water exchange in photosystem II is arrested before dioxygen formation.** *Nat Commun* 2014, **5** <http://dx.doi.org/10.1038/ncomms5305> Article number: 4305.
  - This study used time-resolved membrane inlet mass spectrometry to study the rate of exchange of the two substrate waters immediately prior to the O-O bond formation step. This experiment could only be achieved using chemically modified versions of the cofactor. The authors observe no exchange in this intermediate state ( $S_3^B(Y_Z^*)$ ) suggesting the two substrates are tightly bound. From this result the authors favor the two substrates being Mn ligated oxygen sites (O5 and W2).
48. Kern J, Tran R, Alonso-Mori R, Koroidov S, Echols N, Hattne J, Ibrahim M, Gul S, Laksmono H, Sierra RG *et al.*: **Taking snapshots of photosynthetic water oxidation using femtosecond X-ray diffraction and spectroscopy.** *Nat Commun* 2014, **5** <http://dx.doi.org/10.1038/ncomms5371> Article number: 4371.
49. Kupitz C, Basu S, Grotjohann I, Fromme R, Zatsepin NA, Rendek KN, Hunter MS, Shoeman RL, White TA, Wang D *et al.*: **Serial time-resolved crystallography of photosystem II using a femtosecond X-ray laser.** *Nature* 2014, **513**:261-265.

## 4. CONCLUSIONS

The work described in my thesis provides new important details on the catalytic mechanism of nature's water splitting complex. More generally the work demonstrates that the combination of multifrequency EPR spectroscopy with current state-of-the-art DFT calculations is a powerful tool to elucidate the structure and chemical properties of transition metal complexes. The two key findings of my thesis include:

1. **The identification of possible substrate water binding sites of the cofactor.** To resolve the mechanism of the water splitting, it is critical to ascertain how the cofactor binds the two substrate waters. Although good crystal structures of the cofactor now exist, these data do not unambiguously assign the two substrate sites, resolving at least five candidates i.e. the cofactor water derived ligands. To answer this question, our laboratory developed a new assay based on the detection of  $^{17}\text{O}$  labelled water by high field EPR techniques, specifically EDNMR. Using this method, we have shown earlier that one or more of the oxygen bridges ( $\mu$ -oxo) that connect the manganese ions, rapidly exchanges with  $^{17}\text{O}$  labelled water and are thus a good candidate for one of the substrates. In this study, we determined that only one oxygen bridge exchanges and identified it as O5 (shown in Figure 13). This was achieved by a competitive binding experiment – the addition of ammonia, a water analogue. We could show that ammonia displaces one specific bound water of the cofactor, a water ligand of the terminal/outer Mn ion (Mn4) mid-way through the catalytic cycle. In parallel, using mass spectrometry measurements we could show that the interaction of the two substrates with the cofactor remained unchanged upon binding ammonia, excluding this water ligand as a substrate. This result is important as it had been proposed that water of the terminal Mn ion goes on to form the O-O bond. Our results exclude this mechanistic pathway.

While the binding of ammonia does not inhibit function, it does change the spectroscopic signals of the potential substrate sites seen by  $^{17}\text{O}$ -EDNMR, including the oxygen bridge

signal. This allowed us to assign the exchangeable oxygen bridge to the bridge that connects the terminal Mn ion to the rest of the cluster (O5), as this bridge is nearest (trans) to the ammonia binding site. Thus, these results support mechanisms for O-O bond formation which involve O5. Here, O5 can be considered an ‘activated water’ already having lost both of its protons midway through the catalytic cycle.

- 2. What are the unique chemical properties for identification of oxygen bridges?** If an oxygen bridge is involved in the mechanism of O-O bond formation, it is its chemical bonding to the two Mn ions which will dictate whether its reaction with the second water proceeds by acid-base chemistry, i.e. nucleophilic attack of the oxygen bridge, which acts as an electrophile, or instead allows a radical coupling type mechanism, i.e. between the oxygen bridge of a terminal oxygen (oxyl) radical. Multifrequency and multiresonance EPR techniques are the only tools that allow the study of the electronic structure of oxygen bridges of paramagnetic complexes by labelling the oxygen with  $^{17}\text{O}$ . For a series of model systems we could show that the oxygen bridge motif has a very similar spectroscopic signature, which is significantly different from other types of oxygen ligands. In these experiments we measured the magnetic interaction of the  $^{17}\text{O}$  nucleus with the unpaired electron spin (hyperfine interaction). Preliminary DFT calculations reproduced experimental trends. This oxygen bridge fingerprint will serve as a benchmark for expanded catalytic studies on the catalytic cycle of the water splitting cofactor and metallocofactors in general.

These results, together with other findings have allowed us to propose an extended version of the S-state cycle, describing more accurately the chain of reactions that happens after light excitation of the PSII reaction center. In this extended version, correlations between the sequence of electron and proton coupled transfer events with structural evolution of the cofactor can, for the first time, be rationalized. This extended cycle also demonstrates the importance of the spin state in biological water splitting chemistry. This leads to a mechanism involving two proximal Mn-bound oxygens

located along the Mn1-Mn4 axis. The challenge now is to replicate this same chemistry in synthetic systems, with the goal of producing a cheap, efficient water oxidation catalyst. A series of self-consistent structures of the manganese cluster during the catalytic cycle is shown in Figure 13.

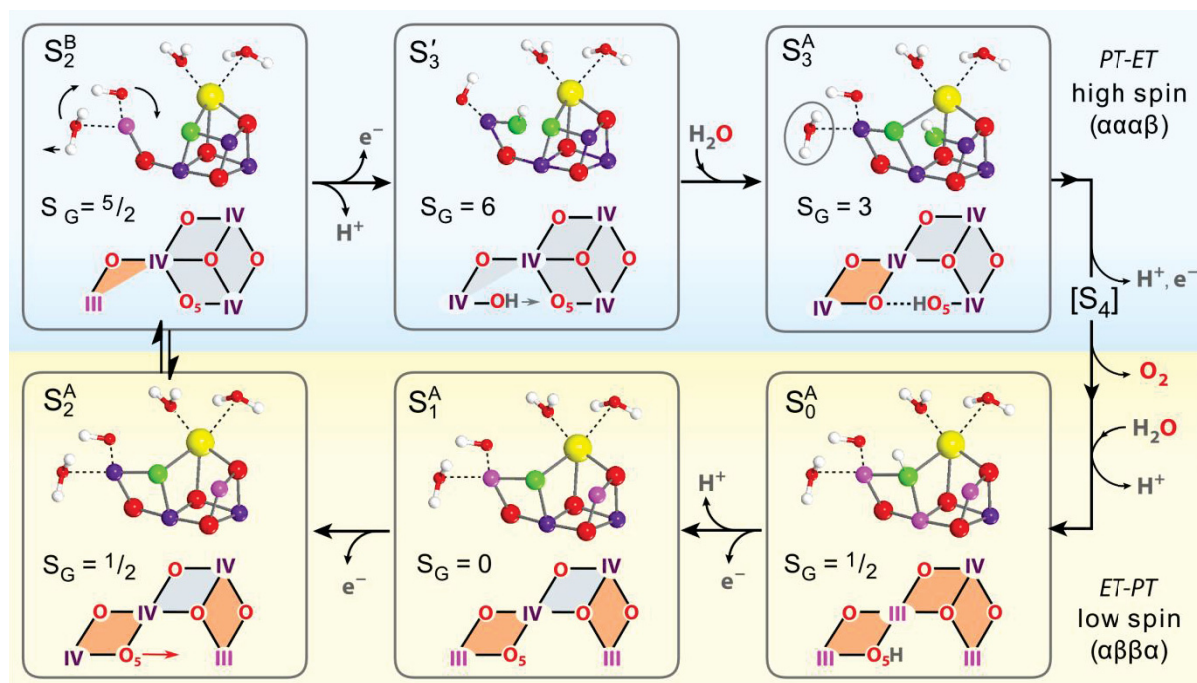


Figure 13. Water oxidation mechanism. Structures of the manganese cluster during the catalytic cycle are presented here. The blue panel corresponds to the high spin configuration, whereas the yellow panel describes the low spin, and a schematic description of the electronic coupling of the cluster evolving from the low spin to a high spin configuration.

## ***ACKNOWLEDGEMENTS***

I would first like to thank my thesis advisor Prof. Wolfgang Lubitz at Max-Planck Institute for Chemical Energy Conversion. The door to Prof. Lubitz office was always open whenever I ran into a trouble spot or had a question about my research or writing. He consistently allowed this paper to be my own work, but steered me in the right the direction whenever he thought I needed it.

I would also like to acknowledge Prof. Klaus Schierbaum of the Department of Materials Science at HHU as the second supervisor of this thesis, and I am gratefully indebted to his very valuable comments on this thesis and guidance during the submission process.

Foremost, I would like to express my sincere gratitude to my team leader Dr. Nicholas Cox for the continuous support of my Ph.D. study and research, for his patience, motivation, enthusiasm, and immense knowledge. His guidance helped me in all the time of research and writing of this thesis. I could not have imagined having a better advisor and mentor for my Ph.D. study.

I would also like to thank the experts who were involved in this research project: Alain Boussac, Dimitrios Pantazis, Vera Krewal, Will Ames, Johannes Messinger, Eiri Heyno, Mark Nowaczyk, and Hediaki Ogata. Without their passionate participation and input, the validation survey could not have been successfully conducted.

Thanks to the wonderful staff of the CEC: Ethel, Ed, Gudrun, Anton, Kristof, Ivy, Patty, Rita...and all the CEC-people for the amazing four years that we spent together.

I thank my fellow lab mates at CEC: Thomas Lohmiller, Nadia Siebel, and Jen Morton. Thanks Leonid Rapatskiy for your patience with me at the lab and teaching me Matlab, and to keep me calm in the moments with more stress, and your support. And I would like to give a “big thanks!” to Maria and Yury... thanks for the stimulating discussions, for the sleepless nights we were working together before deadlines, time shared at the conferences, tea-breaks, lunches and dinners at the EPR lab, and for all the fun we have had in the last two years. Maria and Yury have been a great support in my life...you are my family.

Also I thank my friends, my other “familia” here in Germany. Anna, when we met we were so lost...we are such a pretty mess! But we understand each other somehow and you were my first real friend in Germany... I owe you all! Rosarito, “mi mama”, thanks for you immense love and support and sorry for all the worries I caused you... you are an amazing person and I love you (y lo sabes)! Pelocobre, you are the most intense person I have ever met, but you have a big heart, you are such a

lovely person. Alaa, thank you for every hug...they helped me to heal and put all the pieces back together, so thanks. Thanks Tanze for our little chats, the chocolates you have shared with me and your smiles! Thanks James, Jason and Petr for all your support and advice. Thanks to Olaf, Harun, Dani, Raul, Alina and Jose for all the conversations and all the fun.

Muchas gracias también a todos esos amigos que he tenido en la distancia, pero no por ello han estado menos presentes en mi vida. Javi, Susanita, Ali, Ohzaru, Patricia, Edu, Celia y Clara, Luis, Mariafer, y, especialmente, quería dar las gracias a Mark...que has sido un apoyo muy importante en mi vida, y yo aún tengo la esperanza de que de alguna forma nuestros caminos se vuelvan a encontrar algún día porque te echo mucho de menos y quiero tenerte en mi vida de nuevo. Gracias a mis compis regulatorios de Pharmalex (Laura, Maria, Nacho, Pili, Belen, Lara, Jose, Diego y Suat), por su apoyo diario.

Finally, I must express my very profound gratitude to my parents and my brother for providing me with unfailing support and continuous encouragement throughout my years of study and through the process of researching and writing this thesis. This accomplishment would not have been possible without them. Thank you.

A handwritten signature in black ink, appearing to be 'M. Perez-Navarro', written in a cursive style.

Montserrat Perez-Navarro

## **REFERENCES**

1. Allegre, C. J., Manhès, G., and Göpel, C. (1995) The age of the Earth, *Geochimica et Cosmochimica Acta* 59, 1445-1456.
2. Kasting, J. F., and Walker, J. C. (1981) Limits on oxygen concentration in the prebiological atmosphere and the rate of abiotic fixation of nitrogen, *Journal of Geophysical Research: Oceans* 86, 1147-1158.
3. Schopf, J. W., Oehler, D. Z., Horodyski, R. J., and Kvenvolden, K. A. (1971) Biogenicity and significance of the oldest known stromatolites, *Journal of Paleontology* 45, 477-485.
4. Awramik, S., Schopf, J., and Walter, M. (1983) Filamentous fossil bacteria from the Archean of Western Australia, *Developments in Precambrian Geology* 7, 249-266.
5. Hofmann, H., Grey, K., Hickman, A., and Thorpe, R. (1999) Origin of 3.45 Ga coniform stromatolites in Warrawoona group, Western Australia, *Geological Society of America Bulletin* 111, 1256-1262.
6. Schopf, J. W. (2011) The paleobiological record of photosynthesis, *Photosynthesis research* 107, 87-101.
7. Dupraz, C., and Visscher, P. T. (2005) Microbial lithification in marine stromatolites and hypersaline mats, *Trends in microbiology* 13, 429-438.
8. Bosak, T., Liang, B., Sim, M. S., and Petroff, A. P. (2009) Morphological record of oxygenic photosynthesis in conical stromatolites, *Proceedings of the National Academy of Sciences* 106, 10939-10943.
9. Logan, B. W., Rezak, R., and Ginsburg, R. N. (1964) Classification and environmental significance of algal stromatolites, *The Journal of Geology*, 68-83.
10. Grotzinger, J. P., and Knoll, A. H. (1999) Stromatolites in Precambrian carbonates: evolutionary mileposts or environmental dipsticks?, *Annual review of earth and planetary sciences* 27, 313-358.
11. Reid, R. P., Visscher, P. T., Decho, A. W., Stolz, J. F., Bebout, B., Dupraz, C., Macintyre, I., Paerl, H., Pinckney, J., and Prufert-Bebout, L. (2000) The role of microbes in accretion, lamination and early lithification of modern marine stromatolites, *Nature* 406, 989-992.
12. McKendry, P. (2002) Energy production from biomass (part 1): overview of biomass, *Bioresource technology* 83, 37-46.
13. Whatley, F., Tagawa, K., and Arnon, D. I. (1963) Separation of the light and dark reactions in electron transfer during photosynthesis, *Proceedings of the National Academy of Sciences* 49, 266-270.

14. Blankenship, R. E. (2013) *Molecular mechanisms of photosynthesis*, John Wiley & Sons.
15. Green, B., and Parson, W. W. (2003) *Light-harvesting antennas in photosynthesis*, Vol. 13, Springer Science & Business Media.
16. Horton, P., and Ruban, A. (2005) Molecular design of the photosystem II light-harvesting antenna: photosynthesis and photoprotection, *Journal of Experimental Botany* 56, 365-373.
17. Deisenhofer, J., and Norris, J. R. (2013) *Photosynthetic Reaction Center*, Academic Press.
18. Cox, N., Pantazis, D. A., Neese, F., and Lubitz, W. (2015) Artificial photosynthesis: understanding water splitting in nature, *Interface Focus* 5, 20150009.
19. Umena, Y., Kawakami, K., Shen, J.-R., and Kamiya, N. (2011) Crystal structure of oxygen-evolving photosystem II at a resolution of 1.9 Å, *Nature* 473, 55-60.
20. Suga, M., Akita, F., Hirata, K., Ueno, G., Murakami, H., Nakajima, Y., Shimizu, T., Yamashita, K., Yamamoto, M., and Ago, H. (2014) Native structure of photosystem II at 1.95 Å resolution viewed by femtosecond X-ray pulses, *Nature*.
21. Rapatskiy, L. (2012) The Structure of the Water Oxidizing Complex of Photosystem II and the Sites of Substrate Binding as Investigated by Pulse EPR Spectroscopy, Universitäts-und Landesbibliothek der Heinrich-Heine-Universität Düsseldorf.
22. Satoh, K., and Wydrzynski, T. J. (2005) Introduction to photosystem II, In *Photosystem II*, pp 11-22, Springer.
23. Ho, F., Wydrzynski, T., and Hillier, W. (2012) Substrate and proton channels in Photosystem II, *Molecular Solar Fuels*, 208-248.
24. Rutherford, A. W., Boussac, A., and Faller, P. (2004) The stable tyrosyl radical in photosystem II: why D?, *Biochimica et Biophysica Acta (BBA)-Bioenergetics* 1655, 222-230.
25. Vass, I., and Styring, S. (1991) pH-dependent charge equilibria between tyrosine-D and the S states in photosystem II. Estimation of relative midpoint redox potentials, *Biochemistry* 30, 830-839.
26. Diner, B. A., and Britt, R. D. (2005) The redox-active tyrosines YZ and YD, In *Photosystem II*, pp 207-233, Springer.
27. Havelius, K. G., Sjöholm, J., Ho, F. M., Mamedov, F., and Styring, S. (2010) Metalloradical EPR signals from the YZ· S-state intermediates in photosystem II, *Applied Magnetic Resonance* 37, 151.
28. Hofbauer, W., Zouni, A., Bittl, R., Kern, J., Orth, P., Lendzian, F., Fromme, P., Witt, H., and Lubitz, W. (2001) Photosystem II single crystals studied by EPR spectroscopy at 94 GHz: The tyrosine radical Y, *Proceedings of the National Academy of Sciences* 98, 6623-6628.

29. Kok, B., Forbush, B., and McGLOIN, M. (1970) Cooperation of charges in photosynthetic O<sub>2</sub> evolution—I. A linear four step mechanism, *Photochemistry and Photobiology* 11, 457-475.
30. Pantazis, D. A., Ames, W., Cox, N., Lubitz, W., and Neese, F. (2012) Two Interconvertible Structures that Explain the Spectroscopic Properties of the Oxygen-Evolving Complex of Photosystem II in the S<sub>2</sub> State, *Angewandte Chemie International Edition* 51, 9935-9940.
31. Cox, N., Pantazis, D. A., Neese, F., and Lubitz, W. (2013) Biological water oxidation, *Accounts of chemical research* 46, 1588-1596.
32. Cox, N., Nalepa, A., Pandelia, M.-E., Lubitz, W., and Savitsky, A. (2015) Chapter Nine-Pulse Double-Resonance EPR Techniques for the Study of Metallobiomolecules, *Methods in enzymology* 563, 211-249.
33. Dismukes, G. C. (1996) Manganese enzymes with binuclear active sites, *Chemical reviews* 96, 2909-2926.
34. Cooper, S. R., Dismukes, G. C., Klein, M. P., and Calvin, M. (1978) Mixed valence interactions in di- $\mu$ -oxo bridged manganese complexes. Electron paramagnetic resonance and magnetic susceptibility studies, *Journal of the American Chemical Society* 100, 7248-7252.
35. Randall, D. W., Sturgeon, B. E., Ball, J. A., Lorigan, G. A., Chan, M. K., Klein, M. P., Armstrong, W. H., and Britt, R. D. (1995) <sup>55</sup>Mn ESE-ENDOR of a mixed valence Mn (III) Mn (IV) complex: Comparison with the Mn cluster of the photosynthetic oxygen-evolving complex, *Journal of the American Chemical Society* 117, 11780-11789.
36. Randall, D. W., Chan, M. K., Armstrong, W. H., and Britt, R. D. (1998) Pulsed <sup>1</sup>H and <sup>55</sup>Mn ENDOR studies of dinuclear Mn (III) Mn (IV) model complexes, *Molecular Physics* 95, 1283-1294.

37. Schafer, K.-O., Bittl, R., Zweggart, W., Lenzian, F., Haselhorst, G., Weyhermuller, T., Wieghardt, K., and Lubitz, W. (1998) Electronic structure of antiferromagnetically coupled dinuclear manganese ((MnMnIV)-Mn-III) complexes studied by magnetic resonance techniques, *Journal of the American Chemical Society* 120, 13104-13120.
38. Schäfer, K.-O., Bittl, R., Lenzian, F., Barynin, V., Weyhermüller, T., Wieghardt, K., and Lubitz, W. (2003) Multifrequency EPR investigation of dimanganese catalase and related Mn (III) Mn (IV) complexes, *The Journal of Physical Chemistry B* 107, 1242-1250.
39. Burdi, D., Willems, J.-P., Riggs-Gelasco, P., Antholine, W. E., Stubbe, J., and Hoffman, B. M. (1998) The core structure of X generated in the assembly of the diiron cluster of ribonucleotide reductase: 17O2 and H217O ENDOR, *Journal of the American Chemical Society* 120, 12910-12919.
40. Abragam, A., and Bleaney, B. (1970) *Electron Paramagnetic Resonance of Transition Metal Ions*, Clarendon, Oxford.
41. Schweiger, A., and Jeschke, G. (2001) *Principles of pulse electron paramagnetic resonance*, Oxford University Press on Demand.
42. Weil, J. A., and Bolton, J. R. (2007) *Electron paramagnetic resonance: elementary theory and practical applications*, John Wiley & Sons.
43. Möbius, K., and Savitsky, A. (2009) *High-field EPR spectroscopy on proteins and their model systems: characterization of transient paramagnetic states*, Royal Society of Chemistry.
44. Misra, S. K. (2011) *Multifrequency electron paramagnetic resonance: theory and applications*, John Wiley & Sons.
45. Bencini, A., and Gatteschi, D. (2012) *EPR of exchange coupled systems*, Courier Corporation.
46. Abragam, A., and Pryce, M. (1951) The theory of paramagnetic resonance in hydrated cobalt salts, In *Proceedings of the Royal Society of London A: Mathematical, Physical and Engineering Sciences*, pp 173-191, The Royal Society.
47. Ames, W., Pantazis, D. A., Krewald, V., Cox, N., Messinger, J., Lubitz, W., and Neese, F. (2011) Theoretical evaluation of structural models of the S2 state in the oxygen evolving complex of photosystem II: protonation states and magnetic interactions, *Journal of the American Chemical Society* 133, 19743-19757.
48. Hasegawa, K., Kusunoki, M., Inoue, Y., and Ono, T.-a. (1998) Simulation of S2-state multiline EPR signal in oriented photosystem II membranes: structural implications for the manganese cluster in an oxygen-evolving complex, *Biochemistry* 37, 9457-9465.

49. Rapatskiy, L., Cox, N., Savitsky, A., Ames, W. M., Sander, J., Nowaczyk, M. M., Rögner, M., Boussac, A., Neese, F., and Messinger, J. (2012) Detection of the water-binding sites of the oxygen-evolving complex of photosystem II using W-band  $^{17}\text{O}$  electron–electron double resonance-detected NMR spectroscopy, *Journal of the American Chemical Society* *134*, 16619-16634.
50. Hahn, E. L. (1950) Spin echoes, *Physical review* *80*, 580.
51. Rowan, L. G., Hahn, E., and Mims, W. (1965) Electron-spin-echo envelope modulation, *Physical Review* *137*, A61.
52. Mims, W. (1972) Envelope modulation in spin-echo experiments, *Physical Review B* *5*, 2409.
53. Mims, W. B. (1965) Pulsed Endor Experiments, *Proceedings of the Royal Society of London. Series A. Mathematical and Physical Sciences* *283*, 452-457.
54. Davies, E. R. (1974) A new pulse endor technique, *Physics Letters A* *47*, 1-2.
55. Klauss, A., Haumann, M., and Dau, H. (2012) Alternating electron and proton transfer steps in photosynthetic water oxidation, *Proceedings of the National Academy of Sciences* *109*, 16035-16040.